MODELING AND PERFORMANCE EVALUATION OF ELECTROMAGNETIC SUSPENSION SYSTEMS FOR THE HYPERLOOP

A Thesis

by

ERIC CHAIDEZ

Submitted to the Office of Graduate and Professional Studies of
Texas A&M University
in partial fulfillment of the requirements for the degree of

MASTER OF SCIENCE

Chair of Committee,	Shankar P. Bhattacharyya
Co-Chair of Committee,	Adonios Karpetis
Committee Members,	Aniruddha Datta
	I-Hong Hou
Head of Department,	Miroslav M. Begovic

May 2018

Major Subject: Electrical Engineering

ABSTRACT

In 2012, the founder of SpaceX, Elon Musk, proposed a new method of transportation known as the Hyperloop. The proposed system, which would serve as the fifth method of transportation, described the fundamental theory of traveling in a near-vacuum tube at high speeds in a pod-like vehicle. Since Musk made his proposal, various companies and universities have investigated the Hyperloop concept in order to make it a reality.

Researchers in the engineering and scientific community are currently investigating an effective electromagnetic suspension system design for the Hyperloop. It is hypothesized that a passive magnetic levitation (maglev) suspension system, as similarly designed for maglev trains, can be properly modeled and designed to provide optimized performance results for the proposed transportation method. The electromagnetic suspension design will utilize a specific arrangement of permanent magnets known as the Halbach array. In introducing linear velocity to the magnets, they will induce eddy currents along a conducting surface, and as a result, will create a force of levitation that will sustain the full weight of the capsule. Researchers have also proposed that in using a method of active magnetic levitation, where angular velocity instead of linear velocity is applied to the arrangement of magnets, the electromagnetic suspension will have improved control in stabilizing the induced levitation force and in keeping the displacement gap between the Hyperloop capsule and the conducting track constant.

In order to approach this engineering problem, a specific methodology composed of literature review, calculation analysis, simulation, and testing evaluation has been selected for the purpose of obtaining satisfactory results for the proposed electromagnetic suspension systems. Through literature review, the physical theoretical models behind the proposed technology will be fully investigated in order to properly apply them as the foundational architecture of the suspension system. A mathematical model of the proposed suspension system will be designed and tested through MATLAB, for comparing the theoretical models with experimental data of existing technologies. Furthermore, the simulation results will be observed and analyzed in order to properly evaluate the figures of merit of the electromagnetic suspension methods.

DEDICATION

This thesis in partial requirement in attaining a Master of Science degree is dedicated to my family and loved ones, for their support and encouragement in continuing a higher education degree.

ACKNOWLEDGEMENTS

I would like to thank my committee chair, Dr. Bhattacharyya, my committee co-chair, Dr. Karpetis, and my committee members, Dr. Datta and Dr. Hou, for their guidance and support throughout the course of this research.

Thanks also goes to my friends and colleagues and the department faculty and staff from the Department of Electrical and Computer Engineering and from the Department of Aerospace Engineering, for making my time at Texas A&M University a great experience. Finally, thanks to my mother, father, brother and sisters for providing their encouragement, patience and love in support of pursuing my undergraduate and graduate studies.

CONTRIBUTORS AND FUNDING SOURCES

Contributors

This work was supervised by a thesis committee consisting of Dr. Shankar P. Bhattacharyya of the Department of Electrical and Computer Engineering, who served as chair and advisor, Dr. Adonios Karpetis of the Department of Aerospace Engineering, who served as co-chair and advisor, and Dr. Aniruddha Datta, and Dr. I-Hong Hou, who served as committee members and advisors for this research project.

The contents for Chapter I, as well as any further applicational references throughout the scope of this paper of the presented technology for the Hyperloop System were primarily based on the original design documentation by Elon Musk and SpaceX.

The contents for Chapter II comprised of the mechanical and aerodynamic suspension systems were provided by Dr. Karpetis and his students from the *TAMU Aerospace Hyperloop Team*. Additional material in this chapter includes published work from the MIT Hyperloop team, and from *Maglev trains: Key Underlying Technologies* by Zhigang Liu, Zhiqiang Long, and Xiaolong Li.

All theoretical mathematical formulations for the electromagnetic systems as depicted in Chapters IV, V, and VI were primarily based on calculations previously investigated by the *Lawrence Livermore National Laboratory* through experimentation of a similar system in 1996. Identically, the experimental results for the electromagnetic active magnetic levitation system, as represented in Chapters VII, VIII, and IX were

based on patented documentation from *Propulsion and Control for a Magnetically Lifted Vehicle*, published in 2015 by *Arx-Pax, LLC*.

All other work conducted for the thesis was completed by the student independently.

Funding Sources

Graduate study was supported by a fellowship partnership from Texas A&M University and MIT Lincoln Laboratory through The National GEM Consortium.

NOMENCLATURE

A	Area under permanent magnet arrangement defining conducting circuit area.
B	Magnetic field.
B_r	Remnant magnetic field based on natural properties of permanent magnet material.
$\vec{B}_x$	Induced magnetic field vector in the x direction.
$\vec{B}_{x,mag}$	Magnetic field component of the permanent magnet arrangement in the –x-direction.
$\vec{B}_z$	Induced magnetic field vector in the z direction.
$\vec{B}_{z,mag}$	Magnetic field component of the permanent magnet arrangement in the –z-direction.
$\vec{B}_0$	Magnetic field peak of permanent magnet arrangement.
d	The thickness depth of the Halbach array permanent magnet arrangement.
d_{opt}	Optimum thickness for obtaining maximum lift-to-weight ratio of permanent magnet arrangement.
$\vec{F}_{drag}/\vec{F}_x$	Magnetic drag force resultant from the cross-product of the induced magnetic field (+z-direction) and eddy currents in the y-direction.
$\vec{F}_{lift}/\vec{F}_z$	Magnetic levitation/lift force resultant from the cross-product of the induced magnetic field (+x-direction) and eddy currents in the y-direction.
g	Acceleration due to gravity constant.
Δh_c	Conducting track circuit height under Halbach array.
$\vec{\imath}_e/\vec{I}_y$	Induced eddy currents as a result of the permanent magnet's magnetic field.

k	The wave number of the periodic Halbach array.
Δl_c	Conducting track circuit length under Halbach array.
L_c	Self-inductance of conducting track surface.
LDR	Lift-to-drag ratio of suspension system.
LWR	Lift-to-weight ratio of suspension system.
LPR	Lift-over-power ratio of suspension system.
M	Number of magnets per Halbach array period.
MAGLEV	Magnetic Levitation.
P_c	The perimeter area of the conducting track surface under one Halbach array period.
P_{loss}	Power loss due to drag of suspension system.
p	Permanent magnet density.
r	Radius of one full rotary Halbach array arrangement.
R_c	Resistance property of the conductive track.
s	Side length. Dimension symbol primarily used for a geometrical cube.
T	Time length of one Halbach array period.
$V_\emptyset$	Voltage potential that is induced as a result of the change in magnetic flux (Lenz's Law).
$\vec{v}$	Velocity vector of the permanent magnet's path of travel.
w	The width of the Halbach array.
Δw_c	Conducting track circuit width under Halbach array.
Δz	The distance between the levitated permanent magnet arrangement and the conducting track surface.

δ	Skin-depth effect of a conducting material due to induced eddy currents
λ	The length of the Halbach array.
μ_0	The permeability constant of free space.
ρ	The resistivity parameter of the conducting track.
$\vec{\emptyset}_x$	Induced magnetic flux of Halbach array.
ω	Excitation frequency of the magnetic flux as a result of the speed of the moving Halbach array magnetic field.
ω_m	Angular velocity of rotating Halbach array.

TABLE OF CONTENTS

Page

Page

LIST OF FIGURES

FIGURE Page

FIGURE Page

FIGURE Page

LIST OF TABLES

CHAPTER I

INTRODUCTION

In 2012, Elon Musk, the founder of SpaceX, Tesla Motors, and Solar City, proposed a new method of transportation referred to as the *Hyperloop*, which could be used to travel long distances in a short amount of time. His proposal, as pictured in Figure 1.1, described a transportation system involving a pod-like vehicle shaped like a capsule, achieving very high speeds by traveling in a near-vacuum tube. The key to achieving high velocities during travel would be the existence of low air-pressure inside the tube, allowing the vehicle inside to travel at a high velocity through a significantly lessened effect due to air resistance. [27]

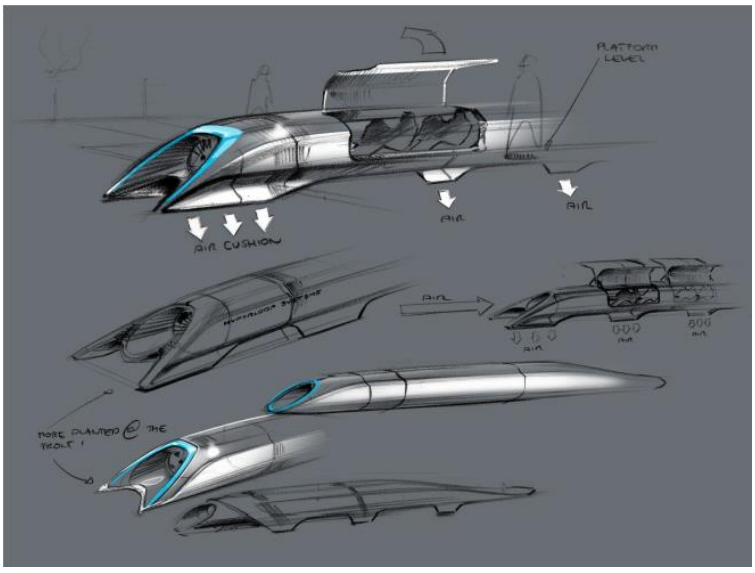

Figure 1.1. Original concept of the Hyperloop as designed by Elon Musk. Reprinted from *Hyperloop Alpha* with permission from Hyperloop (Musk, 2012). [27]

In theory, it was initially proposed that such high speeds would allow this vehicle to travel from San Francisco to Los Angeles in a matter of 35 minutes. However, in order make the short trip possible, the Hyperloop system would be required to travel at speeds up to Mach 1, or 760 mph. The designed trajectory for the Hyperloop system is shown in Figure 1.2. [27]

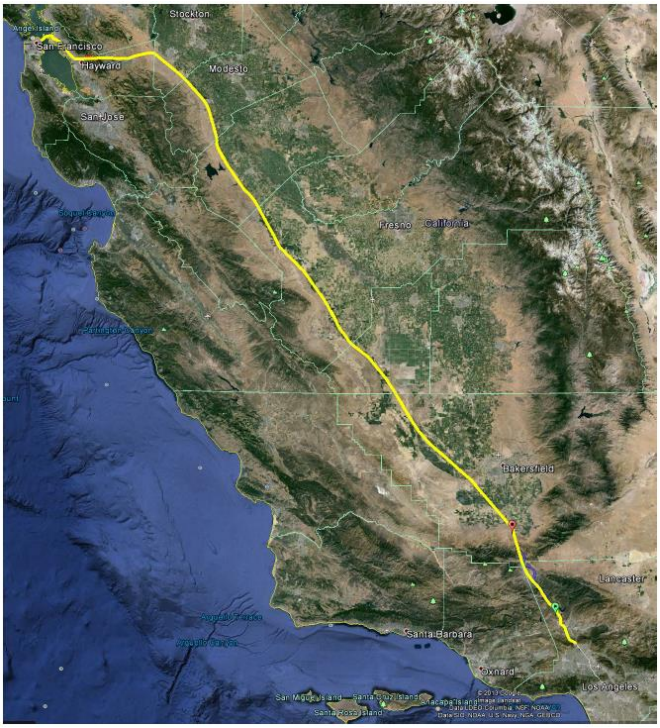

Figure 1.2. The designed trajectory for the Hyperloop for traveling from Los Angeles to San Francisco and vice versa. Reprinted from *Hyperloop Alpha* with permission from Hyperloop (Musk, 2012). [27]

In comparison, available transportation methods that can achieve this speed are primarily military jets and rocket-powered vehicles. Modern commercial airplanes are known to travel at cruising speeds ranging from 546 – 575 mph, but still fall short of the proposed Hyperloop speed. [41] Figure 1.3 shows further examples of the maximum recorded speed of available transportation methods and how each compares to the proposed Hyperloop top speed.

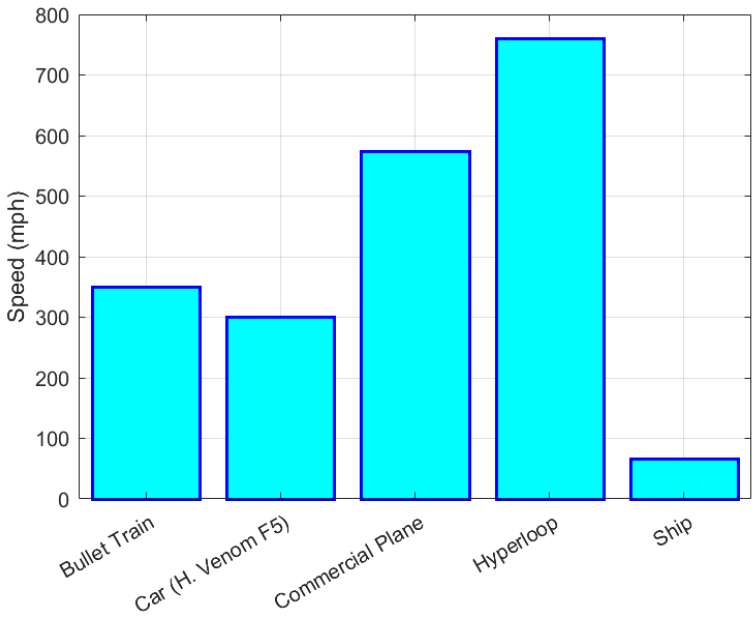

Figure 1.3. Maximum speed comparison of each available transportation system to the proposed Hyperloop. Data adapted from the Hennessey website (2018) [14], *Hyperloop Alpha* (Musk, 2012) [27], Gizmodo (Tarantola, 2017) [37], *Cruise (aeronautics)* (Wikimedia, 2017) [41], and World Economic Forum (2018). [49]

In 2013, Musk unveiled his proposal design for the Hyperloop, where various concepts required in order to make the transportation system a reality were summarized. Among these concepts included conceptual designs for each essential subsystem, such as the onboard power requirements, the propulsions subsystem, and the required suspension system. Although only brief, Musk clearly points out the challenges in his design for each subsystem, and the practicality of creating such a system with a budget of about $6 billion for a passenger-only capsule, and $7.5 billion for a passenger and cargo system. [27]

In order to keep the Hyperloop capsule stable, Musk does indeed point out the importance of designing and implementing an effective suspension subsystem. In his proposal, it is stated that at high velocities, friction becomes a significant issue, and a wheel and axle system would be considered impractical due to rolling friction and dynamic instability that could result in destruction of the vehicle. [27] In the case of the proposed suspension subsystem, Musk suggests two possible methods that would best handle the high speeds of the Hyperloop:

1. Magnetic levitation or Maglev
2. Air bearings

Among these two comparisons however, it is further stated air bearings would ultimately prove to be the most feasible solution due to lack of technology for designing a cost-effective maglev suspension system. [27] Furthermore, in order to create a possible suspension using maglev technology, further research will be required in order

to design an efficient suspension system, as studies have shown such technology requires large power usage.

In exploring further information on each proposed requirement for the subsystems of the Hyperloop, as well as a breakdown of the overall cost for building the transportation system, it is recommended to refer to Musk's original proposal. In the following chapter, each suspension proposed for the Hyperloop will be further explored in order to evaluate the feasibility of each system for meeting the requirements of the transportation method.

CHAPTER II

BACKGROUND OF PROPOSED SUSPENSION METHODS FOR THE HYPERLOOP SYSTEM

Mechanical Suspension Systems

In order to properly evaluate all potential suspension systems for the Hyperloop, a traditional mechanical system must be considered as it is currently the most commonly used suspension system for transportation vehicles. That is, a wheel and axle suspension system as is commonly used in everyday compact vehicles, large transportation vehicles such as semi-trucks, and even airplanes. Overall, such a system, as pictured in Figure 2.1, serves as a fundamental basis for evaluating and modeling a suspension system.

Figure 2.1. Wheel and axle suspension system design. Reprinted from HyperLoopDesign (2015). [16]

On January 2016, Elon Musk himself stated following the first SpaceX Hyperloop Pod Competition Design at Texas A&M University that it is worthwhile to study designs using traditional wheels for various reasons. First, because the Hyperloop will function in a near vacuum environment, it is evident the capsule would be capable of traveling at high speeds through a significant reduction in aerodynamic drag. In such an environment, a wheel-based suspension system should be sufficient in exceeding maximum speeds of comparable vehicles, including the fastest cars in the world which have been capable of reaching speeds up to 300 mph. Secondly, Musk also stressed the importance of using wheels for the Hyperloop capsule in order simplify complexities in terms of initial designs. In other words, as the transportation serves a new innovative concept that has never been practiced in the history of transportation travel, Musk stated "it is important to limit the number of miracles in series" where a wheel-suspension could serve to facilitate any complex issues in the design process. [16]

Several past studies have shown that wheels are capable of achieving very high speeds as proven through past test occurrences. This includes speeds of 622 mph using a pneumatic tire vehicle, and 767 mph using steel tires. It is essential to point out that each of these cases used rocket-powered propulsions. Additionally, studies have suggested that such tire designs are also capable of achieving impressive lift-to-drag ratios, where the tires can lifting heavy objects with reduced drag force due to friction, including 500:1 for the steel tire case, and 300:1 for pneumatic tires. [16] Table 2.1 provides a summary of the highest speeds recorded for such wheel-and-axle suspension systems.

Table 2.1. Summary of fastest recorded velocities and lift-to-drag ratios for given vehicle types. Data adapted from HyperLoopDesign (2015). [16]

Year	Vehicle	Wheel Type	Propulsion	Velocity (mph)	Lift/Drag
2013	Potent & Main Car	Pneumatic	Wheel driven/petroleum	439	300:1
1970	Blue Flame Car	Pneumatic	Rocket	622	300:1
1997	Andy Green Car	Steel	Rocket/Jet	767	500:1

As impressive as many of these past statistics for wheel and axle systems may appear, it is essential to point out that in order to achieve these speeds, massive amounts of fuel would be required in order to power the rocket propulsion vehicles. For all of these cases, the vehicles traveled through short duration trips. In all, the propulsion system is not the only concern as in each case, rolling resistance would also place a factor. Not only would rolling friction cause a reduction in speed, but it would also cause deterioration of the tires due to excessive heat created through increased speed.

A solution to reducing rolling friction would be to apply thinner tires for the Hyperloop capsule, in order to generate less heat through the tire rubber material, if using pneumatic tires for example. [16] However, further studies are required in order to test durability for the tire suspension system given long duration trips as proposed for the Hyperloop.

Aerodynamic Suspension Systems

Another type of suspension that must be considered is that of an aerodynamic system. In the Hyperloop proposal, it is stated that such a suspension can serve as the best potentially used system for supporting the Hyperloop's weight and reducing any form of drag friction. It is superior to a wheel and axle system due to its ability to not introduce rolling or surface contact friction, and to a maglev system due to its fairly inexpensive cost when comparing both suspensions. [27]

The design of the aerodynamic suspension is comprised of various air bearings, as depicted in Figure 2.2. The air bearings are designed to emit high pressurized air in the negative-z direction, with pressure values of 7.5 kPa or higher, in order to carry the weight of the capsule. [27] This is of course dependent on the pressure of the tube, which must be lower than the pressure of the air from the air bearings depicted in Figure 2.2. In effect, this creates a thin film of air lubricant, which is designed to drastically reduce drag force for any propulsion system that drives the capsule's velocity.

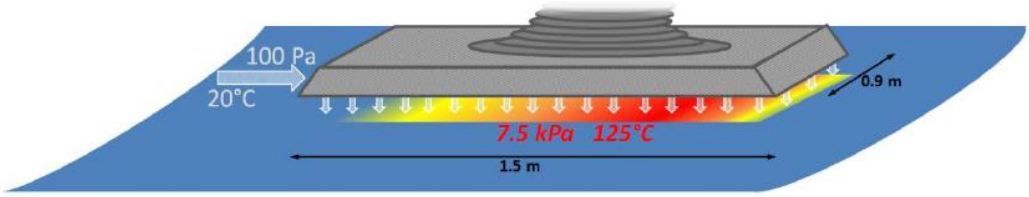

Figure 2.2. The design of an air bearing ski used that can potentially sustain the weight of the Hyperloop capsule. Reprinted from *Hyperloop Alpha* with permission from Hyperloop (Musk, 2012). [27]

The levitation gap between the air bearings and the surface of the track can vary anywhere from $70\ \mu m$ to $5\ mm$. In obtaining this maximum levitation gap, an air bearing prototype device, potentially designed for the Hyperloop was created by the Texas A&M University Hyperloop, or TAMU Hyperloop team. This prototype, which was built and tested for the SpaceX Hyperloop Competition I in January 2017, is capable of lifting heavy loads, where a small-scaled air bearing, as referenced in Figure 2.3, can sustain a $5\ mm$ levitation gap while lifting a load of $22\ lbs$. [18] In building larger-scaled air bearings, or multiple bearings, heavier loads can indeed be sustained for the goal of sustaining the proposed Hyperloop capsule weight of $33{,}000\ lbs$. [27]

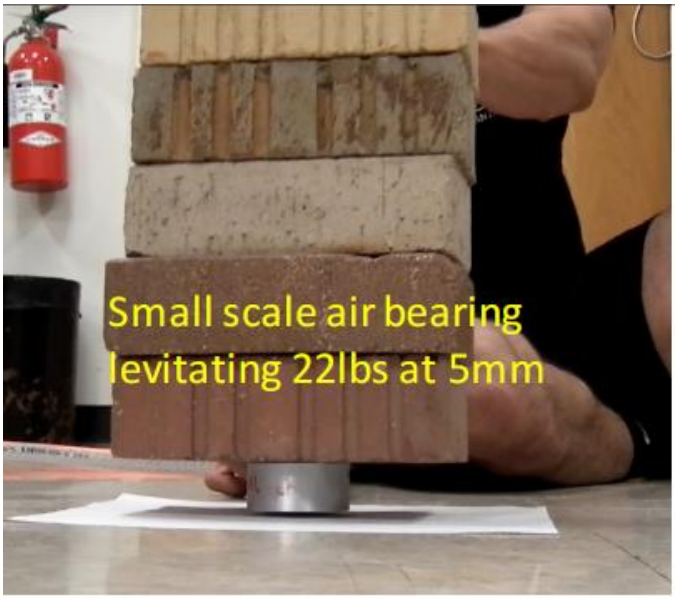

Figure 2.3. A small-scaled prototype of an air bearing as designed by the TAMU Hyperloop team. Reprinted from *Texas A&M Hyperloop* with permission from TAMU Hyperloop (Karpetis, 2017). [18]

From the many advantages of the aerodynamic suspension system, there are however some disadvantages. The first disadvantage is the introduction of additional air into the tube environment. As the tube is to expected to maintain a pressure of $100\ Pa$ (approximately $\frac{1}{1000}$ of normal atmospheric pressure), the air introduced by the air bearings will add complexity in keeping a constant low air pressure in the tube through industrial vacuum pumps. [27] Furthermore, as air pressure inside the tube will be kept at a minimum, it will be difficult for the air bearings to emit the desired air pressure to keep the Hyperloop capsule levitated.

An additional disadvantage to using an aerodynamic suspension system relates to the close proximity of the levitation gap between the air bearings and the surface of the track. Although this is not an issue at low velocities, the small displacement gap creates an issue at high velocities due to the Kantrowitz limit. [27] This limit describes a "chocked-flow" effect, where it takes place when the capsule travels at high velocities near Mach 1, with a consequential effect of increased air pressure formulating between close proximities of the traveling vehicle and the tube surfaces. This effect is essentially dependent on the ratio between the Hyperloop capsule and tube area, where a higher ratio, or in other words, using a pod that almost takes an entire available sectional area of the tube, will lead to a low velocity limit, resulting in velocities exceeding the Kantrowitz limit. The outcome to this can lead to a rupture of the tube due to the high air pressure between the capsule and tube. [29]

As the Kantrowitz limit was referenced in Musk's original Hyperloop proposal, various universities and companies have recognized this as a challenge for the Hyperloop

design. An example of such studies is expressed in Figure 2.4, where the MIT Hyperloop Team showcased studies describing various velocity limits in Mach numbers based on given pod/tube area ratios in investigating designs for their prototype for the Hyperloop competition. Although this limit is not only constrained to aerodynamic suspension designs, as this limit is recognized with any suspension design based on the area ratio between the pod and tube, air bearings will ultimately strengthen the negative effects of this limit due to their emission of high pressurized air with increased speeds. [29]

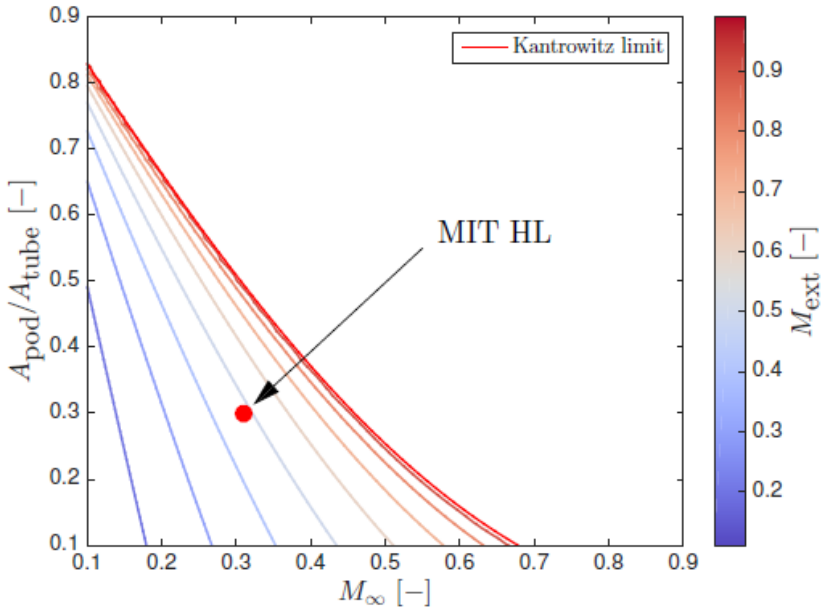

Figure 2.4. The theoretical capsule-to-tube area ratio versus Mach number plot for estimating the Kantrowitz limit (through magnitude variable M_{ext}) by the MIT Hyperloop Team. Reprinted with permission from the MIT Aeronautics department (Opgenoord & Caplan, 2017). [29]

Electromagnetic Suspension Systems

As two distinct types of suspension systems have been introduced and summarized as potential subsystems in the Hyperloop design, the last one to discuss follows the previous types as a suspension system capable of handling the heavy loads of the system's capsule vehicle. As previously mentioned, as each discussed suspension system has various flaws that will need to be addressed as the Hyperloop becomes a reality, it is important to identify all possible alternatives in designing an effective suspension system.

In all, the final alternative to be covered in this investigation is that of an electromagnetic suspension system. This technology, although not a completely new and innovative concept as its application has already been used by various maglev train systems, deserves much attention for its potential capabilities for its compatibility with the Hyperloop capsule and tube design. Much like an aerodynamic suspension design, the concept is based on supporting a vehicle above a track using a thin film of lubricant, where instead of high pressurized air acting as the film lubricant as in the case of an aerodynamic suspension, magnetism from permanent magnets would create this levitation gap. [45] As a result, this technology would function in allowing the Hyperloop capsule to accomplish its short duration trips through high speed travel by eliminating any friction occurring due to surface contact.

Although various iterations of electromagnetic suspension technology have already been designed and built, including for the German TR08 and the Japanese HSST100L maglev trains as pictured in Figure 2.5(a)-(b), the use of this concept has

been overall slow in being implemented to mainstream transportation systems due to its complex and costly design. [22] In order for these systems to work, the track has to be designed with various excitation coils that will interact with the onboard permanent magnets of the vehicle for creating levitation and propulsion (the basic physics behind this concept is later addressed in Chapter IV). Although practical through short distances, the overall cost in building and keeping in good maintenance of such a track will significantly increase if creating a long-distance Hyperloop.

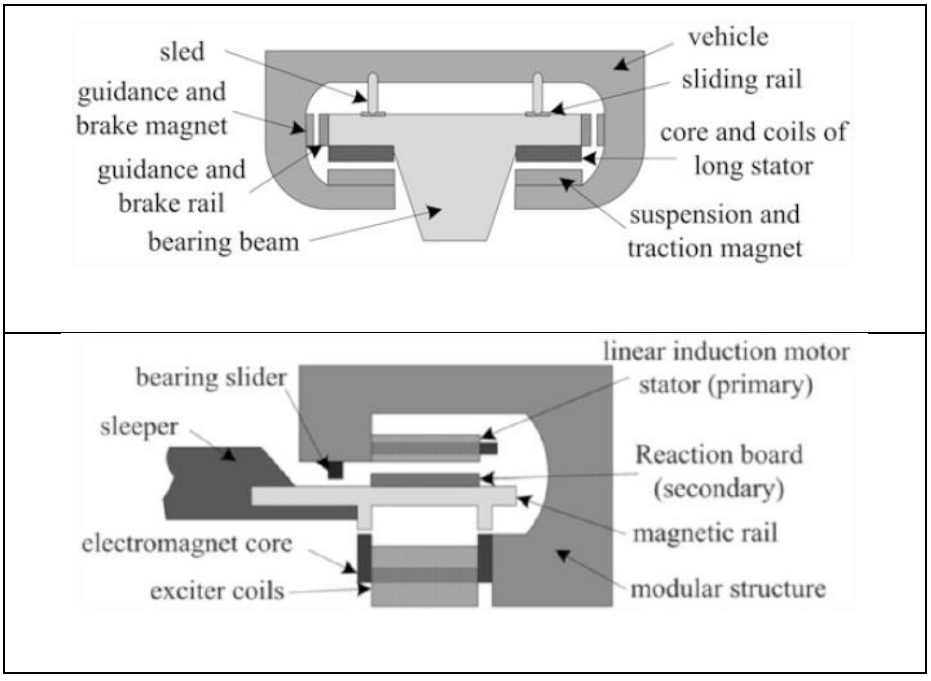

Figure 2.5(a)-(b). The German TR08 (Top) and the Japanese HSST100L (Bottom) are examples of maglev train technology that utilize electromagnetic suspension systems. Reprinted from *Maglev trains* (Liu, Long, & Li, 2015). [22]

Additionally, there is a supplementary setback that will result from this technology. As previously mentioned, although there isn't mechanical friction present due to rolling or surface contact, there is an alternate type of friction that will result in using an electromagnetic suspension system. This friction, known as an electromagnetic drag force, will ultimately reduce the speed of the traveling vehicle. [45] As a result, throughout much of the research done on maglev technology over the span of half a century, the maximum speed attainable by a maglev system has been only up to 370 mph. In comparison, a wheel-based suspension vehicle has managed to reach speeds of up 760 mph, or Mach 1, using rocket-powered propulsion in 1997 by British Royal Air Force pilot Andy Green. [16] Chapter IV further explains how this electromagnetic drag force is formed, and additionally provides methods and techniques for how its overall effect can be reduced.

Suspension Systems Summary Overview

As summarized in Figure 2.6, for all proposed suspension systems of the Hyperloop, there are evident pros and cons to each technology. For each suspension type, there exists a type of friction that will ultimately serve to:

1. Reduce the speed of the vehicle
2. Increase overall power consumption

For each suspension type, there is a direct relationship between the inevitable friction force the capsule will experience through faster velocity and the power that will be required in order to overcome that friction.

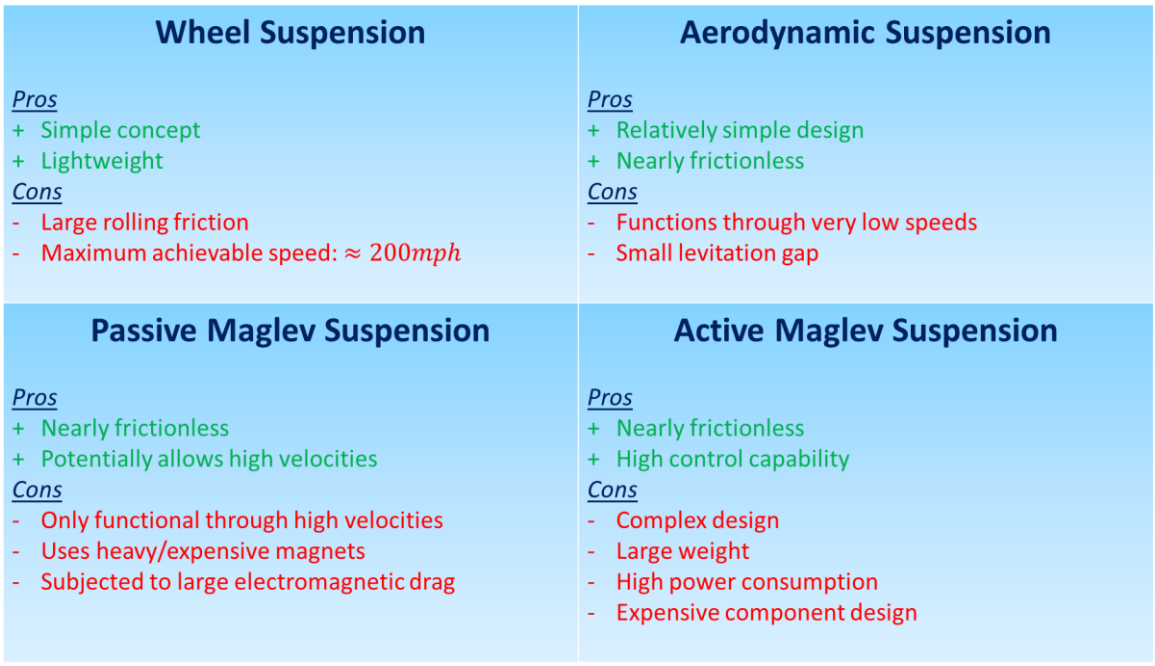

Figure 2.6. A summary comparison of the proposed suspension types for the Hyperloop System. Adapted from *Texas A&M Hyperloop* (Karpetis, 2017). [18]

In the following chapter, the research investigation problem will be defined. Over the course of the following chapters, the scope of focus will be shifted towards the proposed electromagnetic suspension technology, including both in terms of passive and active maglev technology. As it will be investigated, both suspension types function through similar physical concepts, where the theory for each suspension system will function under the utilization of Maxwell's equations.

CHAPTER III

THE HYPERLOOP SUSPENSION PROBLEM DEFINED

Since proposed, various companies and universities have investigated the Hyperloop concept in order to make it a reality. One difficult factor the capsule vehicle will more than likely need to overcome are the high g-forces the passengers inside the vehicle will experience during travel. In the original proposal, the vehicle was designed to travel under speed intervals where it would cruise at constant speed for the majority of the trip. However, in between these intervals, the vehicle will accelerate until reaching its maximum proposed speed of 760 mph, or Mach 1, as depicted in Figure 3.1. It is during these periods when the passengers of the Hyperloop could experience a tremendous amount of force due to the vehicle's acceleration and deceleration. [27]

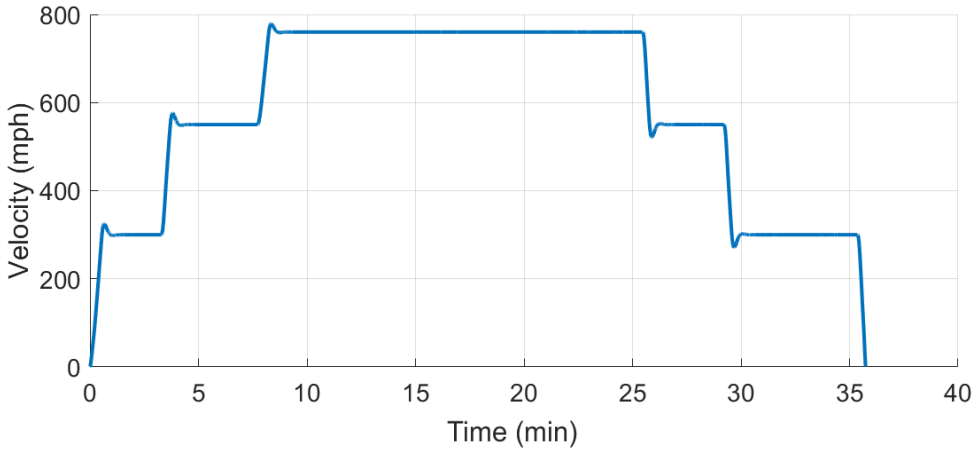

Figure 3.1. The planned velocity trajectory of the Hyperloop for ranging in three different velocity intervals. Data adapted from *Hyperloop Alpha* (Musk, 2012). [27]

An effective suspension system should help lessen this strong force effect on the passengers. However, in order for such a suspension system to be truly operational, it will need to effectively control the mass of the vehicle even when traveling at maximum velocity. Additionally, the suspension will need to be operational under the constraints of the Hyperloop design. For example, a mechanical suspension system will be ineffective due to the effect of rolling friction. In the case of an aerodynamic suspension system, such as air bearings as used in industry applications for lifting heavy objects, there would be an issue in the suspension's functionality due to the proposed low-pressure environment of the tube, along with the introduction of added air in the tube environment. Air bearings will additionally prove to be ineffective for traveling fast at high speeds due to the Kantrowitz limit, as it was pointed out in Chapter II. [29]

Overall, there is a need for an effective design of a suspension system for reducing the heavy forces the vehicle will experience during travel, as well as to avoid any mechanical and aerodynamic friction. As pointed out in Chapter II, a proposed method is the use of a magnetic suspension system, as similarly used by magnetic levitation, or Maglev trains. As these train systems, as shown in Figure 3.2, are known to travel to speeds up to 375 mph with the use of magnetic suspension system, a similar suspension design would allow the Hyperloop to travel up to its proposed speeds. [45]

Figure 3.2. Maglev train systems are known to travel at high speeds with the use of a magnetic suspension system. Reprinted from *Maglev* (Wikimedia, Public Domain, 2018). [45]

Nonetheless, it is impractical to suggest an electromagnetic suspension system will prove to be perfect in every physical aspect, at least in comparison to alternative suspension methods. As it will be explored in later chapters, an electromagnetic suspension system will need to overcome a form of drag force due to electromagnetic drag. This drag, acting as a form of friction force, will consequently reduce the speed of the Hyperloop capsule, and can only be overcome through either high torque motors, or through a higher displacement gap with a stronger levitation force.

Additionally, the overall power requirements in using an electromagnetic system will be expected to be much greater in comparison to traditional mechanical and aerodynamic systems. This is because of expected power dissipation due to

electromagnetic drag forces. It will be necessary to not only provide enough power for creating enough force to levitate a specific payload, but also to overcome power dissipated due to drag force in providing horizontal linear motion for the payload. In terms of power requirement performance, it is expected alternative suspension systems will surpass the electromagnetic suspension methods with current available technology.

Overall, it is still worthwhile to explore this suspension method for its potential capabilities in providing a formidable solution for sustaining the weight of the Hyperloop. As a way to evaluate the performance of both passive and active electromagnetic suspension systems, the following figures of merit will be used:

- Lift over drag force ratio, or LDR
- Lift over power ratio, or LPR
- Lift over weight ratio, or LWR

In terms of the LDR value, this ratio will be dependent on the total levitation and drag force values of the system, where a high efficiency system will be based on if a high lifting force is generated over a low drag force. In terms of the LPR value, this ratio will be dependent on the total lifting force and power dissipation due to drag, where a high efficiency system will be based on if a high lifting force is generated over a low power consumption value. And finally, in terms of the LWR value, this ratio will be dependent on the total lifting force capabilities and the weight of the system, or in the case of the passive and active maglev systems, the weight of the magnets, where a high efficiency system will be based on if a maximum lifting force is generated over the given weight of the magnets.

In laying out the guideline for this research investigation on the electromagnetic suspension system, the passive maglev case will be explored in Chapter IV and serve as the foundational basis as to how this technology works, along with optimization methods introduced in Chapter V. Chapter VI will explore the active maglev case as to how it serves as the translated version of the linear passive case that uses rotational velocity for better control of its levitation force, and Chapter VII discusses commercially available applicational uses. Furthermore, Chapters VIII and IX will compare the theoretical results behind the electromagnetic suspension system with experimental test results from a commercially available device that exploits active maglev technology for evaluating conclusions in Chapter X on the performance of the electromagnetic suspension technology.

CHAPTER IV

THE ELECTROMAGNETIC SUSPENSION: PART 1 – THE PASSIVE MAGLEV SYSTEM

Overview of the Passive Maglev System

The concept of the electromagnetic passive magnetic levitation system is comprised of various physical phenomenon that exploits many concepts derived from Maxwell's equations. It is the foundation to how modern maglev train systems and various motors that use this technique function. In the long run, the result of such a system is a generated force, which in the case of maglev trains and for the ultimate goal of the Hyperloop, will be used to generated levitation. However, in order for such a force to be generated, the key ingredients for this to occur are the introduction of a moving magnetic field environment and electric current exposure. [30, 44]

The simplest case that can be used to describe the concept of a passive magnetic system is that of a moving permanent magnet along a conducting surface as represented in Figure 4.1. In summary, a permanent magnet traveling with a constant velocity in the -x-direction will emit magnetic field lines along a conducting track surface, which will result in induced "eddy" currents to formulate along the track surface. The interaction of the magnetic field lines and the induced currents will as a result generate a force of levitation, which will keep the magnet levitated. [30, 44]

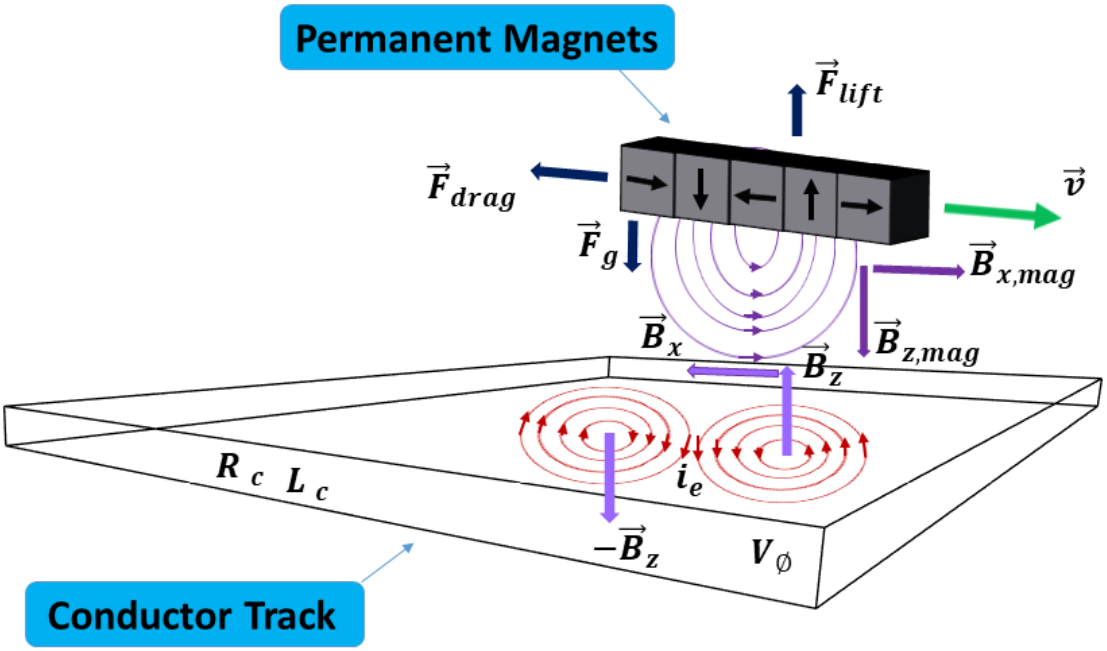

Figure 4.1. An overview of the passive maglev system for a traveling arrangement of permanent magnets along a conducting track. Adapted from Post & Ryutov © 2000 IEEE. [31]

Figure 4.1 provides a summary overview of the passive maglev system. In the representation, there are vector magnitudes representing the magnetic field components in the system, the velocity term, the electrical properties, and force vectors. Table 4.1 provides a summary of these vector variables.

Table 4.1. Vectors and parameters of the passive maglev suspension system. Adapted from Post & Ryutov © 2000 IEEE. [31]

$\vec{B}_x$	Mirrored induced magnetic field in the conducting surface in the +x-direction.
$\vec{B}_z$	Mirrored induced magnetic field in the conducting surface in the +z-direction.
$\vec{B}_{x,mag}$	Magnetic field component of the permanent magnet arrangement in the –x-direction.
$\vec{B}_{z,mag}$	Magnetic field component of the permanent magnet arrangement in the –z-direction.
$\vec{\imath}_e$	Induced eddy currents as a result of the permanent magnet's magnetic field.
R_c	Resistance property of the conductive track.
L_c	Self-inductance property of the conductive track.
$V_\emptyset$	Voltage potential that is induced as a result of the change in magnetic flux (Lenz's Law).
$\vec{F}_{lift}/\vec{F}_z$	Magnetic force resultant from the cross-product of the induced magnetic field (+x-direction) and eddy currents in the y-direction.
$\vec{F}_{drag}/\vec{F}_x$	Magnetic force resultant from the cross-product of the induced magnetic field (+z-direction) and eddy currents in the y-direction.
$\vec{v}$	Velocity vector of the permanent magnet's path of travel.

Overall, such a system is an ideal case of the passive maglev system, as an assumption is made that velocity will remain constant throughout the duration of the permanent magnet's trajectory duration. In truth, this is actually an inconsistency concept as this system will also result in a dragging electromagnetic force due to field

lines traveling in the z-direction. [30] Even if aerodynamic friction is not a factor, this electromagnetic drag will identically serve as a force of friction, and will ultimately decrease the velocity of the traveling magnet until it eventually comes to a stop. In order to keep the velocity from decreasing, such a system will require the use of motors with enough torque to overcome this drag force, a concept that is utilized for the active maglev system as it will later be explored in Chapter VI. However, it is important to study the passive maglev case in order to understand the basic physical concepts that define a functioning electromagnetic suspension system.

The Halbach Array and its Magnetic Field

During the 1980s, physicist Klaus Halbach of the Lawrence Berkeley National Laboratory invented the Halbach array, a method for manipulating the magnetic field of an array of permanent magnets to one side of the array, and ideally, cancelling the field on the opposing side. [19, 43] Such a phenomenon is represented in Figure 4.2.

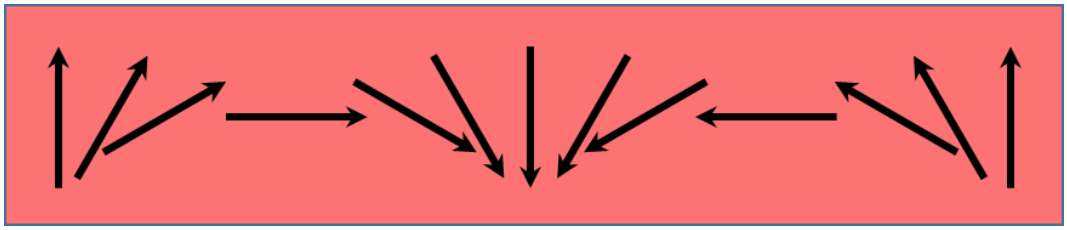

Figure 4.2. Ideal version of the Halbach Array permanent magnet arrangement. Adapted from Long, He, & Xue © 2011 IEEE. [21]

In creating a design for a magnetic suspension for the Hyperloop vehicle, an application of the Halbach array is proposed to be used, as is currently being used for maglev trains and other electromagnetic applications. As the arrangement in Figure 4.2 is impractical to fabricate, the formation of the permanent magnet arrangement is most commonly done through the use of cubital magnets, where each are placed in sequence of a conjoined magnet rotated to a specific angular rotation in reference to the previous magnet. (Han, Ham, & Philips, *Four- and eight-piece Halbach array*) © 2005 IEEE [11] Figure 4.3 shows an example of such an arrangement, where each magnet in sequence is rotated 90 degrees clockwise from the previous magnet.

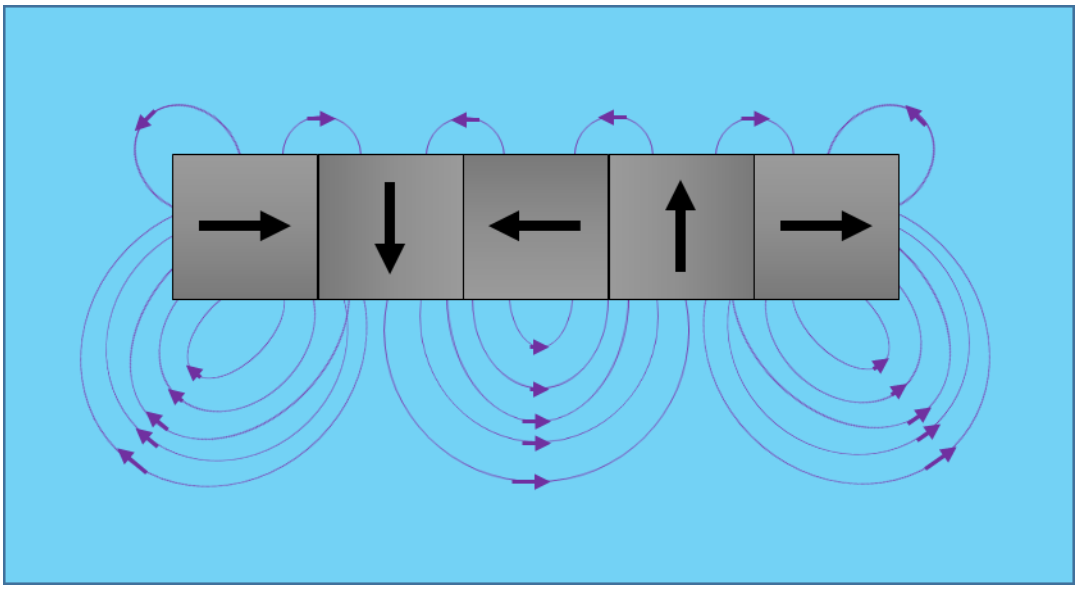

Figure 4.3. An overview of the Halbach Array arrangement of cubital permanent magnets and the resultant magnetic forces on each side of the array. Adapated from *Halbach array* (Wikimedia, 2018). [43]

As represented in Figure 4.3, the resulting magnetic field lines of the Halbach array are sinusoidal in nature, as referenced in many sources as found through literature review. Various mathematical techniques, ranging from Fourier series representation to computational analysis, have been used in order to properly model the magnetic field output of the Halbach array. [12] As the derivation of such mathematical techniques are quite complex to derive in terms of understanding the formulation of the permanent magnet arrangement magnetic field equations, such derivation is outside the scope of the this paper, and the sinusoidal behavior formulation as found in previous studies, will be accepted as the output magnetic field formulation of the Halbach array.

In Figure 4.1, it is shown that the magnetic field lines of the Halbach array arrangement of the permanent magnets are represented by two magnetic field vectors, each perpendicular to each other. If the field lines are facing down to an attracting conducing surface, then these field lines can be represented as $\vec{B}_{x,mag}$ and $\vec{B}_{z,mag}$, where each are magnetic fields in the respective -x and -z directions. When each of these vector components are exposed along a conducting track surface, a mirrored version of induced magnetic field lines will be formed on the opposing direction of the magnet's travel due to the conducting properties of the track. The magnetic field vectors, represented as $\vec{B}_x$ and $\vec{B}_z$, are represented by Eq. 4.1 and Eq. 4.2 respectfully, and the graphical representation of these equations are represented in Figure 4.4. (Han, Ham, & Philips, *Four- and eight-piece Halbach array*) © 2005 IEEE [11]

$$\overrightarrow{B_x}(t) = B_0 \sin(kx)\, e^{-k\Delta z} = B_0 \sin(kvt) e^{-k\Delta z} \tag{4.1}$$

$$\overrightarrow{B_z}(t) = B_0 \cos(kx) e^{-k\Delta z} = B_0 \cos(kvt) e^{-k\Delta z} \tag{4.2}$$

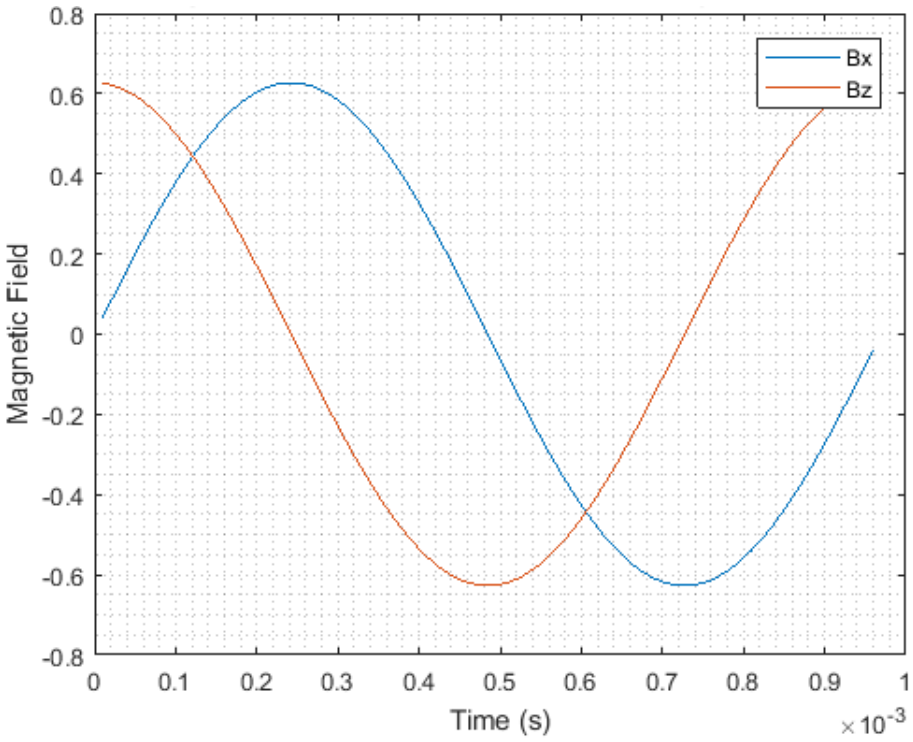

Figure 4.4. Graphical representation of the magnetic field vectors of the Halbach array for one period. Adapted from Post & Ryutov © 2000 IEEE. [31]

In these formulas, k represents the wave number of the periodic Halbach array, x represents the distance traveled of the traveling magnet in the x-direction, Δz represents the levitation gap between the array and the conducting surface, and B_0 represents the peak magnetic field of the permanent magnets. The relationship with k and the length of the array, λ, is described in Eq. 4.3. [30]

$$k = \frac{2\pi}{\lambda} \tag{4.3}$$

Additionally, the peak magnetic field of the permanent magnet arrangement is represented by Eq. 4.4, where B_0 represents an exponential sine cardinal function [40] in relation to d, the thickness of the permanent magnets, the wave number k, M, the number of permanent magnets in the Halbach array, and B_r, the natural remnant magnetic field of the permanent magnet material. [30] For this investigation, neodymium permanent magnets were mainly focused on for their strong magnetic characteristics, which has a natural remnant value of about $B_r \approx 1.41$. [46]

$$B_0 = B_r\left[1 - e^{-kd}\right]\frac{\sin\left(\frac{\pi}{M}\right)}{\left(\frac{\pi}{M}\right)} = B_r\left[1 - e^{-kd}\right]\operatorname{sinc}\left(\frac{\pi}{M}\right) \tag{4.4}$$

Formulation of Induced Currents in the Conducting Track

A key to allowing levitation force to occur is the application of electric currents in the track for which the arrangement of magnets travel. In the case of maglev trains, additional inductive coils are often used for allowing current paths along the track. (Gonzalez, Martines-Diaz, & Cabal, *Mathematical model*) © 2005 IEEE [9] However, for this investigation, such applications will be omitted as including this factor will further introduced complex mathematical derivation of our given passive system, and a simplified conductive track will be studied in order to fully understand the current formulation as a result of the Halbach array magnets.

As the arrangement of permanent magnets travel alongside the conducting track with a given velocity, $\vec{v}$, this effect will create a change in magnetic flux due to the

existing magnetic field vector in the x-direction of the permanent magnet arrangements, $\vec{B}_x$. Overall, because it is assumed the velocity of the magnets are moving in the -x direction, the magnetic flux is assumed to be zero in all other directions. That is, $\vec{\emptyset}_z = 0$, and the magnetic flux is equal to zero in all other directions except in the x direction, as it is assumed there is evident flux changes only in the direction of the moving magnet. Additionally, any small side-to-side perturbation movements in the y-direction and z-directions are ignored, as it is assumed $\Delta y = 0$ and Δz is constant relative to the track surface. [30]

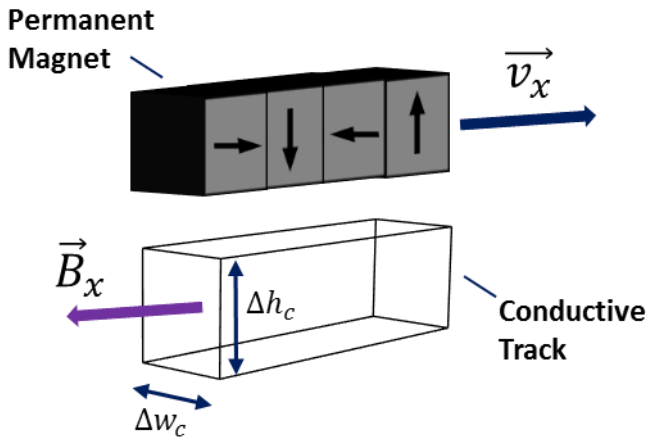

Figure 4.5. Geometrical representation of the magnet's magnetic field in the x-direction traveling through a cross-section of the conducting track. Adapted from Post & Ryutov © 2000 IEEE. [31]

As the resultant mirrored magnetic field vector in the +x-direction opposite from the given velocity in the -x-direction, the magnetic field vector $\vec{B}_x$ will travel through a

cross-section of the conductive track. In this case, it is assumed the cross-section has a rectangular geometrical shape, with dimensions Δw_c and Δh_c, as it is a section of the track most influenced by the magnetic field lines of the permanent magnet arrangement. [30] This is best represented in Figure 4.5. The magnetic flux can be derived through an integration of the magnetic field vector in the x-direction over the cross-sectional area dimensions shown in Figure 4.5. [30] This integration is shown in Eq. 4.5, where the relationship between the magnetic flux and the magnetic field over the cross-section area is shown.

$$\vec{\emptyset}_x = \iint_S \vec{B}_x(t) \cdot ds = \iint_{y,z} B_0 sin(kx) e^{-k\Delta z} \cdot dydz \tag{4.5}$$

In evaluating this relationship over the limits, where y corresponds to Δw_c and z corresponds to Δh_c, the final formulation representation is shown in Eq. 4.6. In this formulation, $w_c = \Delta w_c$ and $h_c = \Delta h_c$ when taking the lower limits for the area integrations as 0. Additionally, it is evidently seen that the magnitude of the magnetic flux is also dependent on the magnitudes of B_0, Δz, the inverse of k, and x, which represents the position of the magnet relative to the track surface. [30, 32] The full derivation for this equation is presented in Appendix A.

In this formula representation, the height of the conducting track, h_c, is part of an exponential term that can reduce skin-depth factor of the conducting track, based on how the magnetic flux penetrates the conducting track depth. [30] Skin-depth is further explored in Chapter V. In various literature sources, this term is often omitted, as it is

assumed this term is small compared to the overall magnetic flux present in the surface of the track.

$$\vec{\phi}_x = \frac{w_c B_0}{k} sin(kx) e^{-k\Delta z}(1 - e^{-kh_c}) \tag{4.6}$$

The magnetic flux present in this system is known to contribute to the electric current formulation within the surface of the track. Because it assumed a material with strong conducting properties is used, such as aluminum or copper, it will be assumed the derivation of the electric current formulation will mirror that of an RL electrical circuit, where Ohm's law can be used to derive the existing current in the passive maglev system. This is represented in Figure 4.6. (Gonzalez, Martines-Diaz, & Cabal, *Mathematical model*) © 2005 IEEE [9]

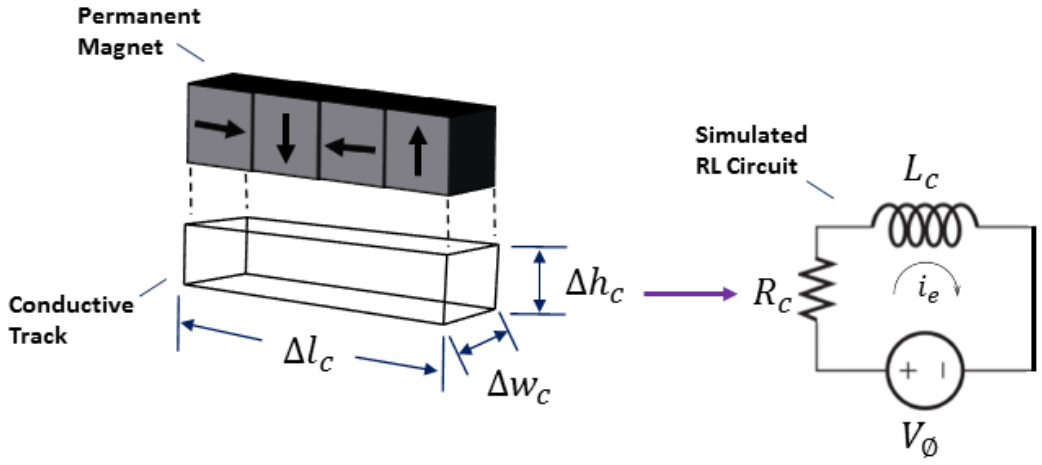

Figure 4.6. Representation of the formulation of electrical current in effect of the conducting track's "simulated RL circuit" due to the track's electrical properties. Adapted from Post & Ryutov © 2000 IEEE [31], and Gonzalez, Martines-Diaz, & Cabal © 2005 IEEE. [9]

Consequently, the magnetic flux formed by the traveling permanent magnet is directly proportional to the voltage potential that will form within the track surface. This is an effect of *Lenz's Law*, which is represented in Eq. 4.7, where a change in magnetic flux over time will indeed induce voltage potential, $V_{\emptyset}$. [44]

$$V_{\emptyset} = -\frac{\partial \emptyset_x}{\partial t} \tag{4.7}$$

Going forward, given that the electrical properties of the conducting track are similar to that of an RL circuit, and that the change in magnetic flux will more than likely be represented as a sinusoidal change over time, Eq. 4.7, can be represented as shown in Eq. 4.8, where L_c is the present self-inductance of the track, R_c is the resistance of the track, i_e is the electric "eddy" current formed along the track, and ω is the excitation frequency of the magnetic flux as a result of the speed of the moving magnetic field vectors. [32, 44]

$$V_{\emptyset}(t) = L_c \frac{di_e(t)}{dt} + R_c i_e(t) = \omega \phi_x cos(\omega t) \tag{4.8}$$

As Eq. 4.8 is a differential equation representation of the electrical current flowing through the conducting surface, this formula can be solved in terms of i_e through various differential equation techniques. [30] For this investigation, Laplace Transform formulation is used (derivation shown in Appendix A) in order to solve for the current, for the current formulation as represented in Eq. 4.9.

$$i_e(t) = \left(\frac{\phi_x}{L_c}\right)\left(\frac{1}{1+\left(\frac{R_c}{L_c\omega}\right)^2}\right)\left[sin(\omega t) + \left(\frac{R_c}{L_c\omega}\right)cos(\omega t)\right] \quad (4.9)$$

Finally, in combining Eq. 4.6, the magnetic flux equation with the above Eq. 4.9 for the electric current, the final formulation for the existing electric current formed in the conducting track is represented in Eq. 4.10. [30]

$$i_e = \left(\frac{B_0 w_c}{kL_c}\right)\left(\frac{1}{1+\left(\frac{R_c}{L_c\omega}\right)^2}\right)\left[sin(\omega t) + \left(\frac{R_c}{L_c\omega}\right)cos(\omega t)\right]sin(kx)e^{-k\Delta z}(1 - e^{-kh_c}) \quad (4.10)$$

It is important to point out various observations as based from this formulation of the electric current equation. It is evident that the magnitude of the current is dependent on the displacement gap, Δz, between the permanent magnet arrangement and the conducting track surface. That is, as $\Delta z \to 0$, $i_e = i_{e,max}$ for the given system. Of course, in order to obtain a large quantity for the electric current, i_e is additionally dependent on the track properties (h_c, w_c, R_c, and L_c), and magnet properties (B_0, k). However, as these are constraint properties that cannot be modified for a given system, the displacement gap, as well as the given velocity of the magnet, are the main control parameters for determining how much current will be generated in this system. [30]

As it will investigated in the next section, these factors also determine how much force will be generated by this system, where Δz will serve as a trade-off factor between the generated levitation and drag force.

Levitation and Drag Forces

In the two previous sections, the mathematical formulations for the magnetic field and electric current equations for the passive maglev system were explored. From these concepts, the resultant forces from this system can be investigated. It is important to understand that this physical relationship is best represented as a *Lorentz Force*, where the cross product of a given magnetic field and moving charge will result in a perpendicular force. This relationship is represented in Eq. 4.11, where the resultant force $\vec{F}$, is dependent on a moving charge q, the velocity of the charge $\vec{v}$, the existing magnetic field $\vec{B}$, and any external electric fields $\vec{E}$, introduced on the system. [7, 12, 30]

$$\vec{F} = q\vec{E} + q\vec{v} \times \vec{B} \tag{4.11}$$

In terms of the given passive maglev system, various points of modification can made to Eq. 4.11. With no external electric field, this formula can be reduced as it is assumed $\vec{E} = 0$. Additionally, as it is well known that $\vec{v} = x/t$, where x can be treated as the length of conducting surface, or $x = \ell$, and the time term can be written in terms of the charge q, a term for current can be expressed for $I = q/t$. As a result, the modified Lorentz force formula is express in Eq. 4.12. [7, 12, 30]

$$\vec{F} = q\vec{v} \times \vec{B} = \vec{I}l \times \vec{B} \tag{4.12}$$

In such a system, it is important to note the direction of each respective vector in in forming a Lorentz force. As it has already been established that the induced magnetic field in the system are traveling in the +x and +z directions for $\vec{B}_x$ and $\vec{B}_z$, it is essential to additionally understand the direction of the formulated eddy currents. As it was

investigated in the previous section, the existing magnetic flux within the conducting track is bounded by the dimensions w_c and h_c, the width and height of the track. Given that the induced electric current will travel along that path of these boundaries, it is safe to assume that the current traveling along the width of the track, which can be considered along the y-axis, will form a cross-product with the magnetic field vectors. Therefore, it can be assumed that $i_e = \vec{I}_y$. Figure 4.7 show the cross-product vectors forming a Lorentz force. [7, 12, 30]

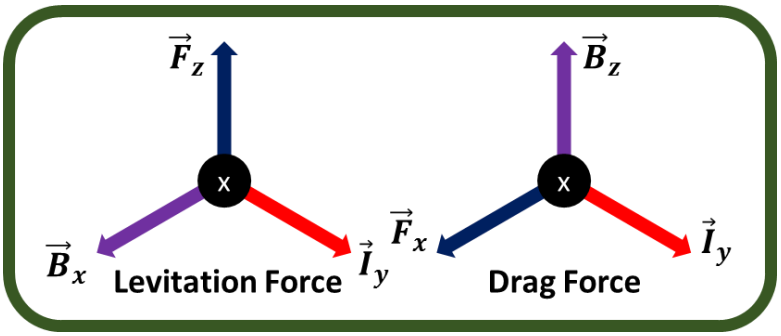

Figure 4.7. The vector formation representations of both the Lorentz levitation and drag forces through induced eddy current and magnetic field vectors. Adapted from Post & Ryutov © 2000 IEEE. [31]

Next, in taking each respective field equation, two different force equations can be derived. In taking the cross product of the current along the width of the track, where it is traveling in the +y direction, with the magnetic field vector found in the +x direction, a resultant force will be found in the +z direction. This will result in a force of levitation, or lift that is represented in Eq. 4.13. [12, 30]

$$\vec{F}_z(t) = w_c \vec{I}_y(t) \vec{B}_x(t) \tag{4.13}$$

Consequently, if the same steps are taken for finding the cross product of the formulated current and magnetic field vector traveling in the +z direction, a resultant force will be found in the +x direction, assuming the magnets/vehicle is traveling in the –x direction. This will result in a drag force that is represented in Eq. 4.14. [12, 30]

$$\vec{F}_x(t) = w_c \vec{I}_y(t) \vec{B}_z(t) \tag{4.14}$$

As the formulations for the levitation and drag forces are sinusoidal in nature, an average of these force equation is often taken as found in various literature sources. That is, an integration of $\vec{F}_z(t)$ and $\vec{F}_x(t)$ can be taken over one periodic term of the excitation wave of the Halbach array, where $T = \frac{2\pi}{\omega}$. The full derivation for these average calculations are found in Appendix A and the solutions for the averages $< F_z >$ and $< F_x >$ are respectively shown in Eq. 4.15 and in Eq. 4.16. [12, 30]

$$< F_z >= \frac{1}{T} \int_0^T \vec{F}_z(t)\, dt = \frac{B_0^2 {w_c}^2}{2kL_c} \frac{1}{1 + (\frac{R_c}{\omega L_c})^2} e^{-2k\Delta z} \tag{4.15}$$

$$< F_x >= \frac{1}{T} \int_0^T \vec{F}_x(t) dt = \frac{B_0^2 {w_c}^2}{2kL_c} \frac{(\frac{R_c}{\omega L_c})}{1 + (\frac{R_c}{\omega L_c})^2} e^{-2k\Delta z} \tag{4.16}$$

The lift and drag forces can be modeled as functions in terms of velocity as represented in Figure 4.8. It is important to note the linear correlation for each of the electromagnetic forces. Both the lift and drag forces exhibit exponential decay functions as $\omega \longrightarrow \infty$. In terms of the lifting force, the functions have a limit as expressed in Eq.

4.17. This limit represents a steady-state form of the lifting equation, following for when levitation reaches a maximum levitation. Additionally, as $\omega \longrightarrow \infty$, the overall drag force approaches zero. These limit decay behaviors are graphically expressed in Figure 4.8. Note that the forces are modeled versus linear velocity in miles per hour instead of the Halbach array frequency in Figure 4.8, for $\omega = kv$. [30]

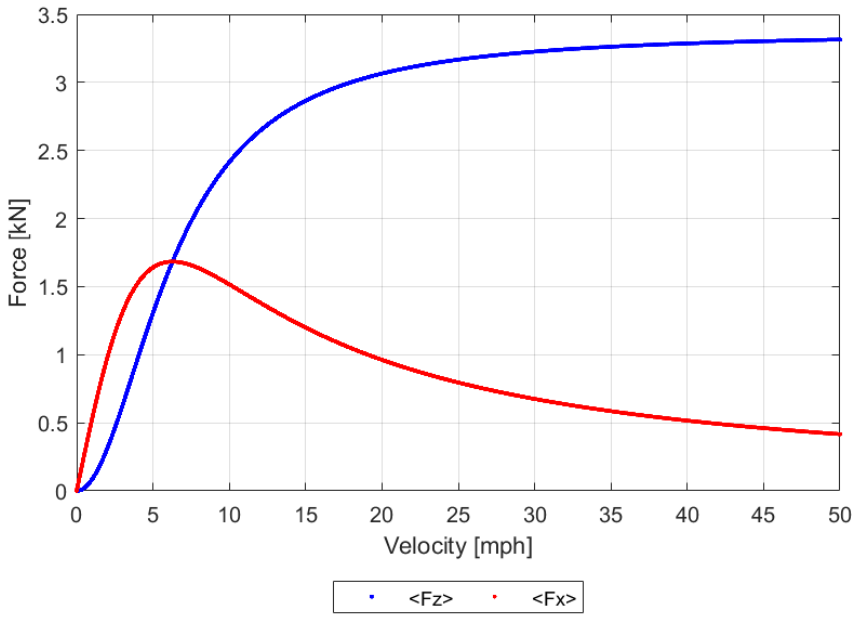

Figure 4.8. The plots for lift and drag forces versus velocity in miles per hour. Adapted from Post & Ryutov © 2000 IEEE. [31]

$$\lim_{\omega \to \infty} < F_z > = \frac{B_0^2 {w_c}^2}{2kL_c} e^{-2k\Delta z} \tag{4.17}$$

$$\lim_{\omega \to \infty} < F_x > = 0 \tag{4.18}$$

Further analysis on the drag force additionally shows that when the drag force is modeled versus the velocity, a peak maximum drag is found within the early regions of a given velocity range. In Figure 4.8, this is shown when the peak drag force occurs at approximately 6 mph. Mathematically, this is represented by taking a derivative of F_x in terms of ω, and solving for ω for when $\frac{dF_x(\omega)}{d\omega} = 0$, where a solution is expressed in Eq. 4.19. Full derivation for Eq. 4.19 is represented in Appendix A. [30]

$$\frac{dF_x(\omega)}{d\omega} = 0 \Longrightarrow \omega = \frac{R_c}{L_c} \tag{4.19}$$

This is a common side effect of most passive maglev suspension systems, as most significant drag will be experienced at early velocity intervals. It is one of the main reasons why most transportation systems that use maglev suspension require high velocities in order to prove to be effective. For this reason, several factors can be taken for evaluating the performance of the passive maglev resultant forces as described in the next section.

Performance and Efficiency Factors of the Passive Maglev System

In evaluating the performance of the overall levitation capabilities of the passive maglev system, a ratio evaluation can be considered for comparing the resultant lift and drag forces. Such a performance factor can be used in order to evaluate how effective the system is in terms of handling electromagnetic drag force. As previously mentioned, this drag force is a form of friction that will ultimately result in $\vec{v} = 0$ without a robust form

of propulsion for keeping a constant velocity, or through increasing velocity during transient acceleration time periods.

Therefore, in obtaining a lift/drag ratio from the derived levitation and drag average forces, the following relationship is found in Eq. 4.20. As evidently seen, when taking a ratio of $< F_z >$ and $< F_x >$, various terms in each respective formula will cancel out, and a ratio of the product of the Halbach array frequency and self-inductance of the track over the resistance of the track will result. [30]

$$LDR = \frac{< F_z >}{< F_x >} = \frac{\omega L_c}{R_c} = \frac{2\pi v}{\lambda}\left(\frac{L_c}{R_c}\right) \tag{4.20}$$

This shows us that the given LDR will ultimately depend on the velocity of the magnet, along with the electrical properties of the conducting track surface. In order to have an efficient lift-to-drag value, the conducting track needs to have a low resistance and a high self-inductance. For the given conductive track in Figure 4.6, the formulas for resistance and self-inductance are found in Eq. 4.21 and Eq. 4.22 respectively. [30, 42]

$$R_c = \rho \frac{l_c}{h_c w_c} \tag{4.21}$$

$$L_c = \frac{\mu_0 P_c}{2k\lambda} \tag{4.22}$$

In the case of both the resistance and inductance of the conducting track, it can be seen that each quantity depends on various dimensions from the conducting track. In the case of the resistance formula, the Halbach array length, λ, the height, h_c, and the width, w_c, along with the resistivity, ρ of the track under the influence of the permanent

magnet are considered. The self-inductance of the track is also dependent on λ, along with the wave number k, the permeability constant $\mu_0 = 4\pi\ x\ 10^{-7}$, and the perimeter, P_c, of the area under the permanent magnet. [30, 42]

Studying these formulas can provide much overview in ways for reducing electromagnetic drag force. As expressed in Eq. 4.21, the resistance of the track can be lowered in increasing the thickness, or height h_c, or width w_c of the track. Moreover, selecting the correct material for the track plays a factor for an efficient passive maglev system based on its electrical properties. For this reason, good conductors such as aluminum or copper are recommended to be used, as they are known to have low resistivity, high conductivity, and relatively low permeability constants. [42] Table 4.1 shows a summary of the electrical properties of various conducting surfaces.

Table 4.2. Electrical properties of various conducting materials. Data adapted from the Massachusetts Institute of Technology (2004) [23] and *Electrical resistivity and conductivity* (Wikimedia, 2017). [42]

Material	Resistivity (Ωm) at 20 °C	Conductivity (Sm^{-1}) at 20 °C	Permeability (NA^{-2})
Aluminum	$2.65x10^{-8}$	$3.50x10^{7}$	$1.2567x10^{-6}$
Copper	$1.68x10^{-8}$	$5.96x10^{7}$	$1.2566x10^{-6}$
Silver	$1.59x10^{-8}$	$6.30x10^{7}$	$1.2566x10^{-6}$
Gold	$2.44x10^{-8}$	$4.10x10^{7}$	$1.2566x10^{-6}$
Iron	$9.71x10^{-8}$	$1.00x10^{7}$	$6.3x10^{-3}$

Another method to evaluate the efficiency of this system is by determining how much power will be dissipated due to electromagnetic drag. This relationship is represented in Eq. 4.23. [30]

$$P_{loss} = vF_x \tag{4.23}$$

As seen in Eq. 4.23, there is a direct relationship between the power loss, P_{loss}, and the drag force that is generated by the system. Evidently, as this system increases in velocity, the power loss factor will additionally increase linearly. This means that if this technology is applied to the Hyperloop, as the capsule reaches top speeds of Mach 1, the power-to-drag force ratio will be expected to be 343:1. For this reason, as it will be investigated in later chapters through evaluation results of this system, it essential to reduce the drag force in order to reduce power loss due to electromagnetic drag through various methods, including by increasing the levitation displacement gap of the system. [30]

Furthermore, another method to evaluate the efficiency of this system is through a ratio comparison of the lift force and power loss. Eq. 4.24 shows this lift/power loss ratio, which is represented as LPR. [30]

$$LPR = \frac{F_z}{P_{loss}} \tag{4.24}$$

This ratio is essential to understand how much power will be ultimately required in order to lift a given weight force. A common value of $LPR = 1.0\ N/W$ is often found in passive maglev systems, as investigated by the *Lawrence Livermore National Laboratory* through their studies of *Inductrack* tests they performed. Additionally,

through their tests, it was found that adding coil circuits under the passive maglev system can ultimately improve the lift/power ratio with values of $LPR > 1.0\ N/W$. [30] Currently, such technology is already being practice by maglev train systems for handling heavy payloads, and consequently, could serve as a robust method in using for the Hyperloop system.

CHAPTER V

PERFORMANCE OPTIMIZATION AND LOSSES OF THE ELECTROMAGNETIC SUSPENSION SYSTEM

Optimization through a Conventional Track

As previously discussed, Chapter IV describes an ideal method of a passive maglev levitation system where it is assumed velocity will be kept constant as the permanent magnet travels alongside the track. However, it must be noted that a factor within the conducting track that will ultimately contribute to inefficiencies within the system is that of skin-depth. [30, 48] As eddy-currents form alongside the track, the induced currents will additionally travel inside the depth material of the conducting track, and will generate excess heat, which can contribute to loss of lift force and increased drag.

Past experimentation results of the passive maglev system by the Lawrence Livermore National Laboratory have let to studies of a conventional version of the conducting track that allows for optimization of the system. This track, known as a *flat-track*, uses a specific geometry of the track as seen in Figure 5.1, which ultimately lessens skin-depth effect and any other ohmic losses by reducing the track surface to a closely packed “rail-like” track, where the track is made of bars that act as an independent circuits from each consecutive bar. [30]

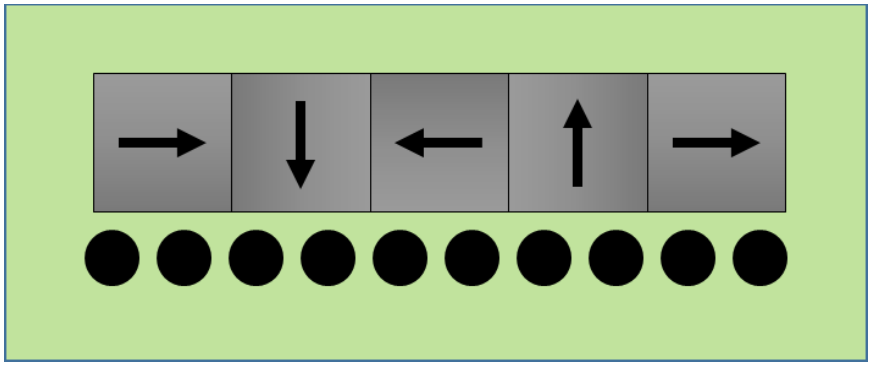

Figure 5.1. Flat-track design as designed by the Lawrence Livermore National Laboratory for reducing skin-depth effect and improving levitation force. Adapted from Post & Ryutov © 2000 IEEE. [31]

An advantage to using this type of track is the improvement of the overall inductance of the track. As seen in Eq. 4.19, the overall inductance of the track is dependent on the properties of the track, including the surrounding perimeter of the track surface where eddy currents will travel. Through this design, due to the reduction of each circuit's perimeter area, each bar in this track is very thin where $P_c = w_c$. As this is the case, when this is applied to the inductance equation, the overall lift equation over the area of one circuit bar is optimized as expressed in Eq. 5.1, where $A = w_c\lambda$. [30]

$$< \frac{F_z}{A} >= \frac{B_0^2}{\mu_0} \frac{1}{1 + (\frac{R_c}{\omega L_c})^2} e^{-2k\Delta z} \tag{5.1}$$

Eq. 5.1 can be optimized further as it is assumed that if $\vec{v} \to \infty$, or a very large velocity is reached, then a maximum lifting force formula can be found. Mathematically, this is done when a limit is be taken to Eq. 5.1, as $\omega \to \infty$. The maximum lift over area

formula is expressed in Eq. 5.2. Appendix A shows the full derivation of this limit calculation. [30]

$$< \frac{F_{z_{max}}}{A} >= \lim_{\omega \to \infty} < \frac{F_z}{A} > = \frac{B_0^2}{\mu_0} e^{-2k\Delta z} \tag{5.2}$$

Optimization of the Halbach Array

As an extension to optimizing the passive maglev system, the permanent magnets that are used to form the Halbach array are looked into. In all, the dimensions of the magnets can be optimized in order to carefully select values that can provide the maximum amount of lifting force the suspension system will emit, but at the same time, will contribute to the least amount of weight for the magnet arrangement.

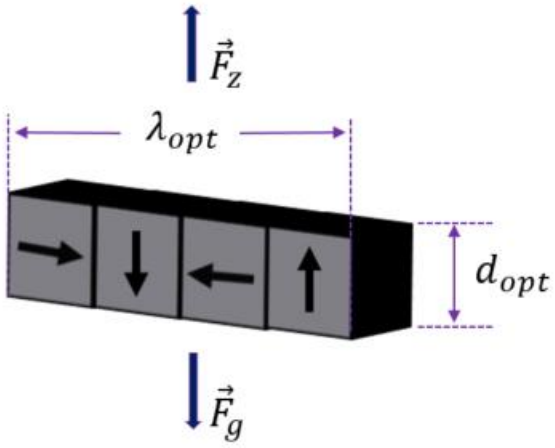

Figure 5.2. The design of a Halbach array through optimized dimensions for achieving a maximum lift-to-weight ratio. Adapted from Post & Ryutov © 2000 IEEE. [31]

In creating an optimized Halbach array, the length, λ, and depth, d are carefully selected to values that will provide the maximum lifting force that can best offset the weight of the magnets. Such expressions can ultimately be express as λ_{opt} and d_{opt} for an optimum Halbach array length and depth respectfully. [30] This is best represented in Figure 5.2.

In order to find these values, fundamental calculus techniques can be applied, where a first-derivative test can be applied to the overall lift-to-weight ratio of the magnets. This algorithm can be described in three single steps.

First, a ratio of the lift-to-weight ratio is found, where the lift equation is expressed as represented in Eq. 5.2 for a maximum lift, and the weight of the magnet arrangement for one Halbach period is expressed as $F_g = pw\lambda dg$, where p is the density of magnets, w, λ, and d are the respective width, Halbach length, and depth of the magnets (which combined also make up the volume of the magnets), and g is the gravity constant assumed at $9.81 m/s^2$. Additionally, it must be recalled that the peak magnetic field expression, B_0, also has a terms for λ and d as found in Eq. 4.3 and Eq. 4.4 from Chapter IV, so careful consideration must be taken in evaluating LWR. This ratio is expressed in Eq. 5.3. [30]

$$LWR = \frac{< F_{z_{max}} >}{F_g} = \frac{AB_0^2\mu_0^{-1}}{pw\lambda dg} e^{-2k\Delta z} \tag{5.3}$$

Secondly, through Eq. 5.3, the LWR can be expressed as a function where all variables are fixed, except for d, the depth of the magnets. In sweeping the lift-to-weight function over a range of values for d, it will be explored that through very small values

for d, LWR is fairly small but increases drastically very fast up to a maximum point for a certain value of d, and then begins to decay as d increases. This maximum value can be found through a first-derivative test as expressed in Eq. 5.4, where LWR is differentiated in terms of d, set equal to 0, and then solved for $d = d_{opt}$. [30]

$$\frac{d(LWR(d))}{d(d)} = 0 \Longrightarrow d = d_{opt} \tag{5.4}$$

Finally, similar steps are next taken for the length of the magnet arrangement, as an expression is written for LWR, with the found value for d_{opt}, and in terms of a range of values for λ. In performing a first-derivative test for this expression, where LWR is differentiated in terms of λ, and the derivative is set equal to 0, solving for λ will allow the solution to be found for $\lambda = \lambda_{opt}$. This final step is summarized in Eq. 5.5. [30]

$$\frac{d(LWR(d_{opt}, \lambda))}{d(\lambda)} = 0 \Longrightarrow \lambda = \lambda_{opt} \tag{5.5}$$

In following this methodology, a solution of $d_{opt} = \frac{1}{5}\lambda$ and $\lambda_{opt} = 4\pi\Delta z$ were respectfully found. It must be noted that comparable results were found by the Lawrence Livermore National Laboratory through a similar investigation. Appendix A has the full derivation to how these solutions can be acquired. [30]

In their studies, it was explored that in using a target displacement gap of $\Delta z = 3cm$, a maximum lift-to-weight ratio of 50:1 was found. [30] Such a ratio has the potential to handle heavy loads as would be expected for the Hyperloop capsule. In order to offset the overall payload weight of the vehicle, passengers, luggage, and onboard

instrumentation, the suspension magnets could be designed as such for finding the optimum dimensions that will support the maximum load.

Performance Losses due to Skin-Depth

In further investigation of evaluating the performance of the electromagnetic suspension, it must be noted that there will be existing performance losses when generating lift due to the skin-depth of the conducting track. This factor, as previously discussed, occurs when eddy currents are formed primarily along the track surface, which in effect increases heat and resistance along the conducting track. Unless a special track is used, as illustrated in Figure 5.1, a single slab (or a stack of single slabs) will ultimately suffer the effects of skin-depth and such performance losses will affect lift, drag, LDR, and lead to higher power losses. [30]

Figure 5.3. A single conductive slab will be susceptible to skin-depth factors.

Mathematically, skin-depth is expressed in Eq. 5.6, where it is described as the square-root of twice the resistivity of the track, ρ, over the product of the Halbach

angular frequency of the permanent magnet arrangement ω, times the permeability constant of free space, μ_o. [30]

$$\delta = \sqrt{\frac{2\rho}{\omega\mu_o}} \tag{5.6}$$

Experiments conducted by the Lawrence Livermore National Laboratory have previously formulated a theoretical formula for accounting skin-depth of the lift formula. This modification is expressed in Eq. 5.7. [30]

$$< F_{z,\delta} >= F_{z,max} \frac{\left(\sqrt{1+\frac{k^4\delta^4}{4}} - \frac{k^2\delta^2}{2}\right)^{3/2}}{k\delta + \left(\sqrt{1+\frac{k^4\delta^4}{4}} + \frac{k^2\delta^2}{2}\right)^{3/2}} \tag{5.7}$$

In Eq. 5.7, the term for maximum lift, $F_{z,max}$, as expressed in Eq. 5.2, is modified to include skin-depth and the Halbach array wave number constant, k. A similar derivation is expressed in Eq. 5.8 for the LDR_δ. [30]

$$LDR_\delta = \frac{1}{k\delta}\left(\sqrt{1+\frac{k^4\delta^4}{4}} - \frac{k^2\delta^2}{2}\right)^{1/2} \tag{5.8}$$

Consequently, Eq. 5.7 and 5.8 can be used to derive a formula for drag force under the effect of skin-depth factors. [30]

$$< F_{x,\delta} >= {< F_{z,\delta} >}/{LDR_\delta} \tag{5.9}$$

Equations 5.7-5.9 can be described as the most “realistic” equations for measuring the lift and drag forces of the electromagnetic suspension system levitating

under a conductive slab. In Chapter VIII, these formulas are tested and evaluated in comparison to the ideal force formulas of the passive maglev system as derived in Chapter IV. Additionally, the validity of Eq. 5.7-5.9 is further explored as these formulas are tested against experimental data provided from an existing active maglev device, as will be introduced in Chapter VII.

CHAPTER VI

THE ELECTROMAGNETIC SUSPENSION: PART 2 – THE ACTIVE MAGLEV SYSTEM

Overview of the Active Maglev System

As the passive maglev case was covered in Chapter IV, a transition of topic can be made in discussing the electromagnetic active maglev system. In all, the concept of an active maglev system has only been utilized in electromagnetic applications that involve energy generation, including transformers, or even in common technology applications, such as an exercising bicycle. [35, 45] However, the usage of this technology as a suspension type is still fairly new, where the idea of an active maglev suspension device is essentially a "hover-board device", as popularized in science fiction media. [36]

As this is the case, the active maglev system, through real-life technology applications, has proven to be worth discussing for its potential to serve as a "friction-less" suspension system for the Hyperloop, at least in terms of mechanical friction. Furthermore, as discussed in Chapter II, an active maglev system functions as a suspension type through magnetic lift, much like the passive maglev case. In the case of the active maglev suspension however, more robust control is applied in the amount of levitation required for increasing or decreasing the displacement gap of the suspension and the contact surface. As it will be further elaborated, this type of control can prove to be more effective than the passive case, as the active suspension would function independently from the vehicle's velocity thrust, a concept that would be desired in terms of vehicle

safety. [36] Additionally, as this technology eliminates the need for a long and specially designed track to increase the velocity of the vehicle, the active maglev case can potentially cost much less than passive maglev suspension technology.

Mathematical Formulation of the Active Maglev System

In all, the active maglev system can be considered a derivative of the passive maglev case, for much of the physical phenomenon considered in for creating an effective system is similar. In other words, all of the components required to create a force of levitation are the same, where a Halbach array of permanent magnets in motion is utilized above a conducting track surface in order to induce eddy currents, and a perpendicular cross-product results in a Lorentz force. [19, 43]

The difference between both electromagnetic suspension cases however is the velocity term. Where the passive maglev system depends on linear velocity, $\vec{v}$, for controlling its levitation gap, the active maglev case uses angular velocity for functionality. [36] This is the case as the active maglev system functions as a rotational translation of the linear Halbach array, as represented in Figure 6.1.

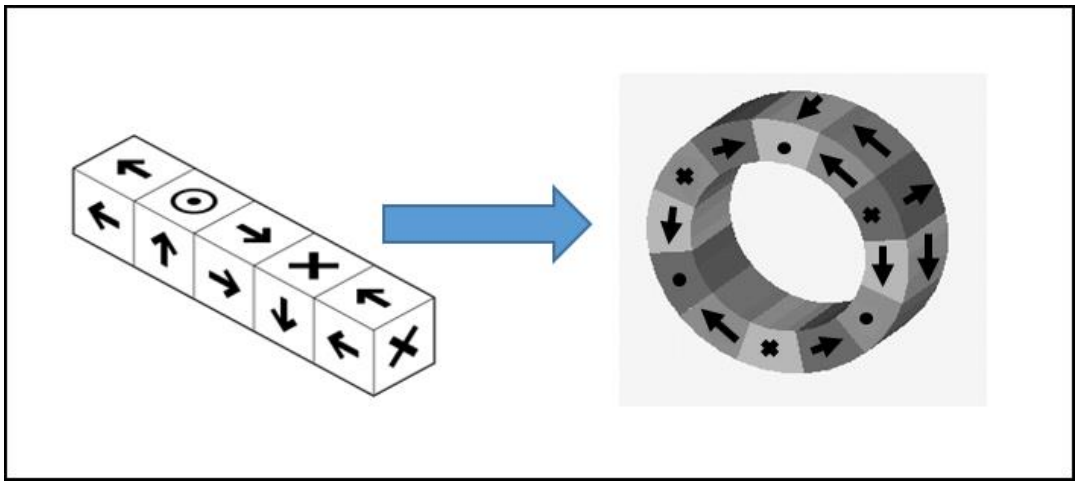

Figure 6.1. Translation of a linear to a circular arrangement of the Halbach Array. Reprinted from *Halbach array* (Wikimedia, 2017). [43]

In translating linear velocity into angular velocity, the radius of the translated circular Halbach array is considered. This is represented in Eq. 6.1, where the angular velocity ω_m, is presented as the ratio of the linear velocity v (note this velocity is a scalar quantity, and not a vector since it has no specific direction) of the system over the given radius the Halbach array circle as presented in Figure 6.2. Furthermore, the angular velocity is presented with the subscript m (which is in reference to a motor creating such an angular velocity), as to not confuse the symbol with the Halbach array frequency, ω. [17]

$$\omega_m = \frac{v}{r} \tag{6.1}$$

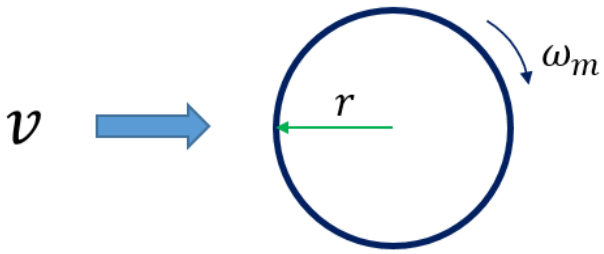

Figure 6.2. Representation of the translation of taking the magnitude of linear velocity into a component of angular velocity given a circle of trajectory with a specific radius. [17]

Figure 6.2 shows a visual representation on how the velocity of a linear Halbach array can be represented in terms of angular velocity. As it be expected, creating this type of angular velocity can be achieved through the use of a rotational motor with a given radius, r. [17]

As previously mentioned, the mathematical derivation for the induced current and Lorentz force formulas are assumed to be similar as with the passive maglev case. For this reason, it can be assumed the formulations presented in Chapter IV are sufficient in applying for the active maglev case. In following the same methodology in solving for the lifting force of the active maglev system, Eq. 6.2 is found. [17, 30]

$$< F_{lift} >= \frac{B_0^2 {w_c}^2}{2kL_c} \frac{1}{1 + (\frac{R_c}{k\omega_m L_c})^2} e^{-2k\Delta z} \tag{6.2}$$

As expected, Eq. 6.2 is identical to Eq. 4.15, where the lifting force for the linear Halbach array magnet arrangement is presented in Chapter IV. It must be noted that in this

presentation of the lifting force equation, the transient state portion of the formula is represented with ω_m instead of ω.

Consequently, the active maglev system will also experience a form of electromagnetic drag force. The formulation for the active maglev drag force can be found by applying Eq. 6.1 into Eq. 4.16, the drag force formula presented for the linear Halbach array magnet arrangement. The drag force representation of the active maglev system is presented in Eq. 6.3. [17, 30]

$$< F_{drag} >= \frac{B_0^2 {w_c}^2}{2kL_c} \frac{(\frac{R_c}{kr\omega_m L_c})}{1 + (\frac{R_c}{k\omega_m L_c})^2} e^{-2k\Delta z} \tag{6.3}$$

As it might have been noted, the levitation and drag forces for the active maglev case were represented with a subscript of $lift$ and $drag$, where the forces for the passive maglev case were represented with a subscript of z and x respectfully. This is but a small consideration of notation that was considered mainly due to two factors:

1. In order to differentiate the force formulas for the passive and active maglev systems.
2. For proper notation purposes, essentially for the drag force.

Following the second factor, proper notation is important for allowing consistency in properly labeling the forces for the active maglev system. Because the drag force in the passive maglev case was expected to be in the $+x$ direction, assuming the magnet travels in the $-x$ direction, the drag force was labeled as F_x. However, for the active maglev system, we can no longer assume this due to the system's rotation motion. The drag force

in this case will be in the form of a force opposing the rotational Halbach array's motion, where if the magnets travel in clockwise orientation, the drag will be experienced as a counterclockwise force. [17, 30]

Identically, the active maglev system formulation can also be modified to include skin-depth factor, through equation Equations 5.7-5.9. In all, Eq. 5.6 is modified where in including the active maglev's angular velocity, ω_m. The result is expressed in Eq. 6.4. This skin-depth factor is included in the Chapter IX results for obtaining a closer proximity to the experimental results of the active maglev system. [17, 30]

$$\delta = \sqrt{\frac{2\rho}{k\omega_m\mu_o}} \tag{6.4}$$

In general, utilizing a suspension using the active maglev case is dependent to using a type of electrical motor for creating the system. As is the case, this makes the active maglev system very attractable in implementing for the abundant availability of commercial electrical motors in the market. As it will be explored in the next chapter, several prototypes using this type of suspension system have recently been created in the hopes of using for future technologies.

CHAPTER VII

APPLICATIONS OF THE ACTIVE MAGLEV SUSPENSION SYSTEM

Application Overview of an Active Maglev Device

In Chapter VI, the mathematical derivation for the theoretical levitation of an active maglev device was presented. As much of what was covered behind the active maglev suspension system can be considered conceptual theory, as such technology is still fairly new in being used in applications, it is important to cover an existing prototype that currently uses this suspension system.

In 2014, the engineering company *Arx-Pax* created the *Hendo* board, a real-life active maglev device. [2, 13] At the time, the device was described by *Time* magazine as one of the most innovative devices of the year for being essentially the first hoverboard device. [38] The device, resembling much like an ordinary skateboard, but comprised of rotating magnet arrangements instead of wheels, is seen in Figure 7.1.

Figure 7.1. The *Hendo* board from Arx-Pax uses active maglev technology for levitation applications. Reprinted from Hendo Hover (Kickstarter, 2014). [13]

Design of the Active Maglev Device

Through literature review, it was investigated that Arx-Pax created nine patent modifications for the *Hendo* hoverboard device as of 2017. Over the course of time, the company made various modifications for their device, primarily based on an improved design and efficiency of the board. [2, 13]

In analyzing patented information for the prototype, various design schematics show to reveal the *Hendo* is primarily comprised of 2-4 rotary Halbach array designs (early iterations of the device used 2 rotary arrangements, while later implementation used up to 4 rotary arrangements). Each rotary Halbach array arrangement is comprised of 16-20 permanent magnets, each arranged to form a circle with a diameter of

approximately 7.5 inches (with an outer motor diameter of 8.5 inches). An example of a 16-magnet rotary arrangement is found in figure 7.2. [3]

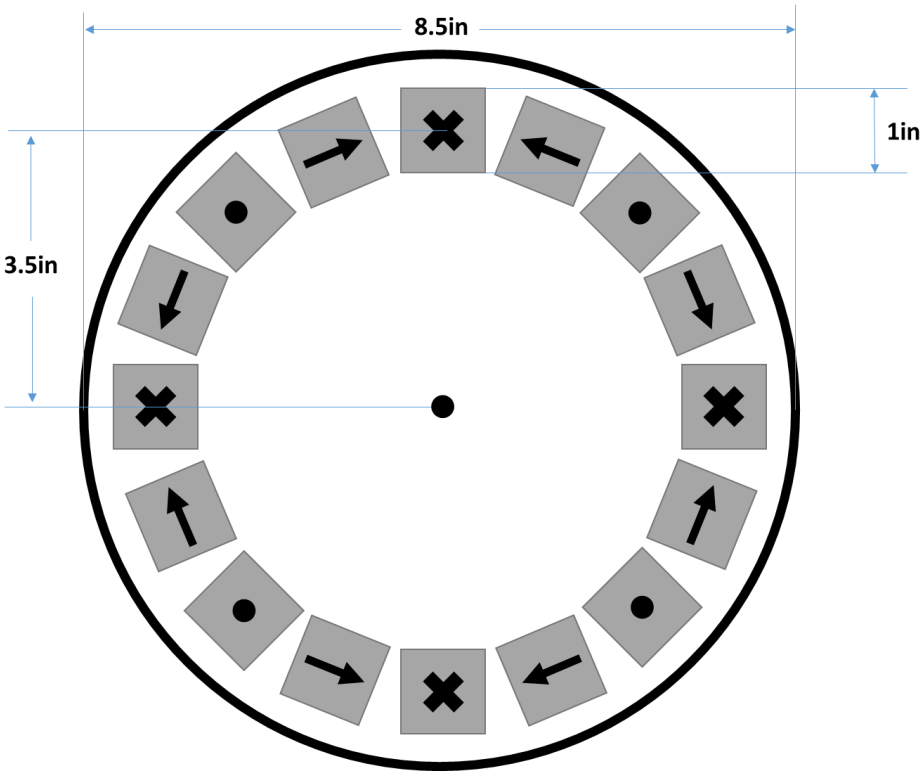

Figure 7.2. Example of a permanent magnet rotary arrangement that is utilized for the *Hendo* active maglev device. Adapted from *Arx-Pax* (2015). [3]

Furthermore, this design is comprised of four magnets per periodic Halbach array waveform, that is, $M = 4$. The permanent magnets are all cubed-shaped magnets with given side parameters of $s = 1\ in$, or about $s = 2.54\ cm$ in metric units, and are all neodymium type magnets, which typically have a remnant magnetic field value of $B_r =$

1.4 T. In using Eq. 4.4, these parameters will provide a peak magnetic field value of $B_0 = 1.0\ T$. This peak magnetic field value can be considered quite impressive, as a typical refrigerator magnet usually is known to have a magnetic field value of approximately $B = 5.0\ mT$, a magnetic field ratio comparison of 200:1 to that of the cube magnets. [3]

Through the design of Figure 7.2, one rotation of the rotary permanent magnet arrangement will be comprised of four Halbach array periodic waveforms. Although each magnet is not conjointly packed as in the case of the passive maglev case, through high speed rotation of the permanent magnets, the active maglev device should simulate the magnetic field periodic waveforms based on the formulas for Eq. 4.1 and Eq. 4.2. [3, 36]

Additional patented data information shows the lifting capability and expected drag force for the *Hendo* hoverboard. As represented in Figure 7.3, the expected lifting and drag force closely match the theoretical force plots represented by Figure 4.8, as represented in Chapter IV. Although Figure 7.3 describes the force plots for an active maglev application, it must be noted that there is indeed much fascination in not only the close correlation found from expected data coming from the applicational device to the theoretical calculations of a designed active maglev device, but also in terms of the close correlation that is expected when comparing both a passive maglev and an active maglev system. [3, 30]

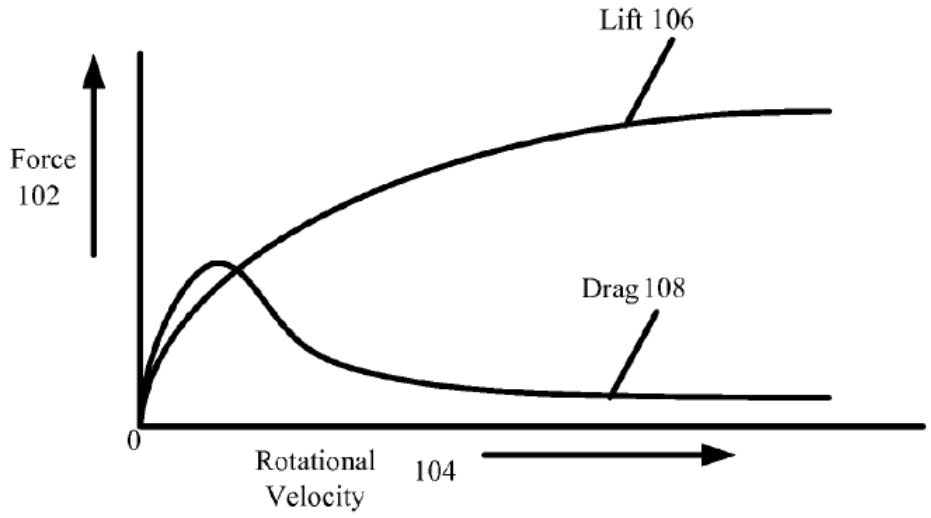

Figure 7.3. Expected lifting and drag force for the *Hendo* active maglev hoverboard device. Reprinted from *Arx-Pax* (2015). [3]

Figure 7.3 further supports the evidence that heavy drag force will be experienced by any active Halbach array device during the early stages of increasing rotational velocity runs. As rotational velocity is increased, the overall drag force will begin to decrease and as result, will lead to an increase in the levitation gap between the device and the conducting track surface. In order to overcome this drag force, relatively high torque motors are recommended for the design of an active maglev system. As an example, the prototype application of the *Hendo* device used motors with maximum torque values of approximately $9.73Nm$. [3] Without enough torque, the experienced electromagnetic drag force will in effect decrease the rotational speed of the motors up to a maximum speed limit, and result in an inefficient system.

In the end, it is not sufficient to merely point out samples of the data coming from the applicational device in order to verify the theory presented in the earlier chapters for both the passive and active maglev system. As it will be showcased, the scope of the following chapters will be comprised of much of this verification, where simulation data, primarily coming from theoretical calculations for each of the systems, will be compared with available test data from the patented active maglev device. This test methodology will consequently be used to draw conclusions in evaluating the necessary figures of merit for both electromagnetic suspension systems.

CHAPTER VIII

SIMULATION RESULTS OF THE PASSIVE MAGLEV SYSTEM

Simulation Methodology Overview

In obtaining results for this investigation, the primary simulation tool used was MATLAB software. Through MATLAB's powerful capabilities of modeling large amounts of data with precision in a relatively short amount of time, the selection of this software for this investigation was more than acceptable in order to validate the theoretical results and compare with the provided experimental results.

In all, two major scripts were written for testing the electromagnetic suspension system: one for the passive maglev system and one for the active maglev system. Although both scripts were designed in a similar way, where the results for both scripts provided output plots of each system, the major difference between both scripts was the experimental comparison factor.

In the case of the passive maglev simulation, the suspension system was modeled under two scenarios: a passive maglev model without consideration of skin-depth and one where it is considered. This script was modeled in such a way in order to show the effect of skin-depth and how it affects the overall performance of the system. As the effect of skin-depth is not considered in various pieces of literature review documenting maglev levitation, it is essential to show a graphical representation of how this factor does indeed affect the performance of an electromagnetic suspension system, essentially when comparing to a real-life application. From this simulation comparison, results are

provided for modeling lift and drag forces, lift-to-drag, lift-to-weight, power loss, and lift-over-power.

Following the passive maglev model results, Chapter IX follows the methodology and results for the script design of the active maglev system model.

Results of the Passive Maglev System Model

In modeling all figures of merit for the passive maglev system, various parameters were considered. These parameters included the size of the magnets, the types of magnets, the number of magnets used per Halbach array arrangement, the conducting track material used, and the selected displacement gap between the magnets and track. A table of these parameters is included in Appendix C.

In the case of the passive maglev system, two case scenarios were modeled: one where skin-depth was not considered and one where it was factored in the system. Figure 8.1 models the lift and drag forces versus linear velocity of both passive maglev scenarios.

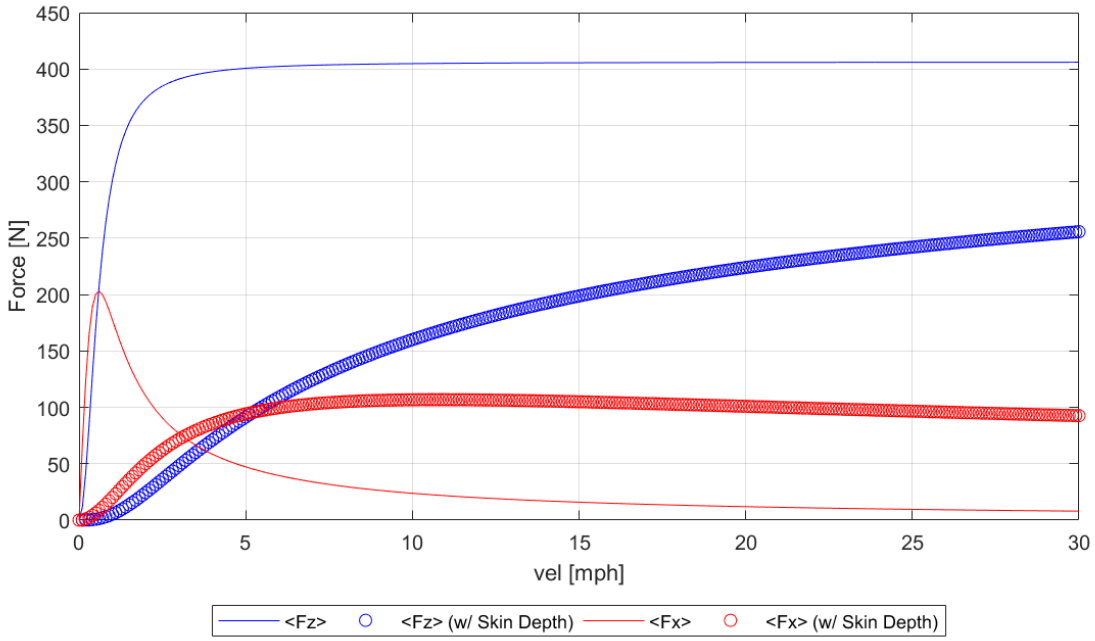

Figure 8.1. Passive maglev performance model of lift and drag force (N) versus velocity (mph). Data adapted from Post & Ryutov (1996). [30]

In analyzing Figure 8.1, it can be seen that forces for lift and drag follow the expected theoretical models as seen in Figure 4.8, where a peak drag force is experienced in the early stages of the velocity span. However, it must be noted that if skin-depth is factored in the system, the electromagnetic drag force increases and decreases from the maximum peak drag in a much slower fashion as compared to the case where skin-depth is not factored. Additionally, the lift force of the system when considering skin-depth of the track increases to its maximum limit much slower than given a track with no skin-depth factor considered. Essentially, both lift and drag models are expected to reach their limits even if skin-depth is factored into the system, as

represented in Eq. 4.17-4.18. However, if skin-depth is considered in the system, much larger velocities will be required in order to reach the lift force limit and for the drag force to become zero.

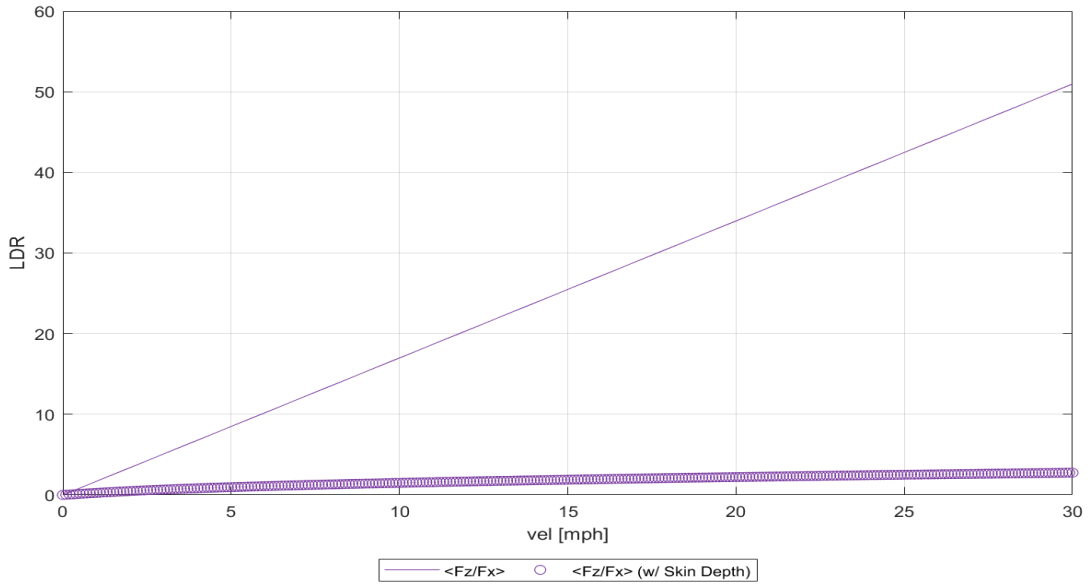

Figure 8.2. Passive maglev performance model of lift/drag versus velocity (mph). Data adapted from Post & Ryutov (1996). [30]

The lift/drag, or LDR of the passive maglev system is modeled in Figure 8.2 against linear velocity. When skin-depth is not considered, the LDR slope is seen to be much greater than that of the system where skin-depth is factored. As represented in Figure 8.2, the slope comparison can be seen to be about 50:3 in comparing the ideal

LDR to the non-ideal LDR with skin-depth factor. Figure 8.3 shows the LDR versus velocity plot in log-scale.

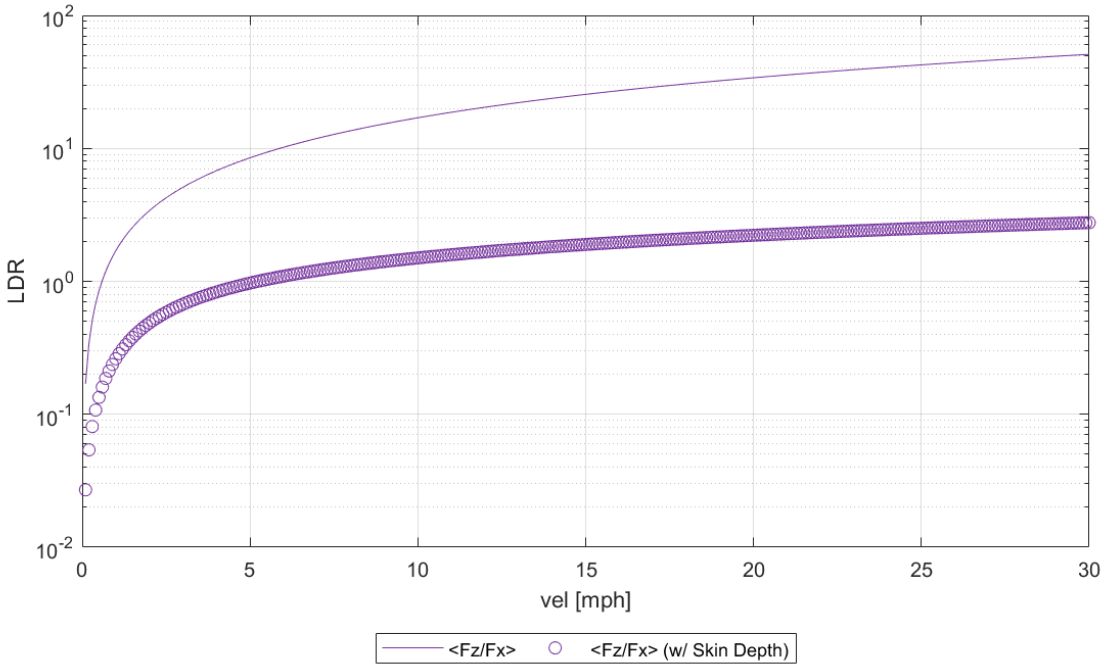

Figure 8.3. Passive maglev performance model of lift/drag versus velocity (mph) in log-scale. Data adapted from Post & Ryutov (1996). [30]

In Figure 8.4, the lift/weight is modeled against the linear velocity of the permanent magnets over the conducting track. The overall shape of the plots for both the passive maglev systems resemble the plots of Figure 8.1 for the lift force. This is because the relationship of both F_z and the LWR versus velocity is expected to be similar, but different in magnitude as LWR accounts for the weight of the magnets

throughout the velocity trajectory. Similar to the plot for F_z, the LWR for the track when skin-depth is considered will required a much larger velocity in order to reach a magnitude similar to that of an ideal system with no skin-depth considered.

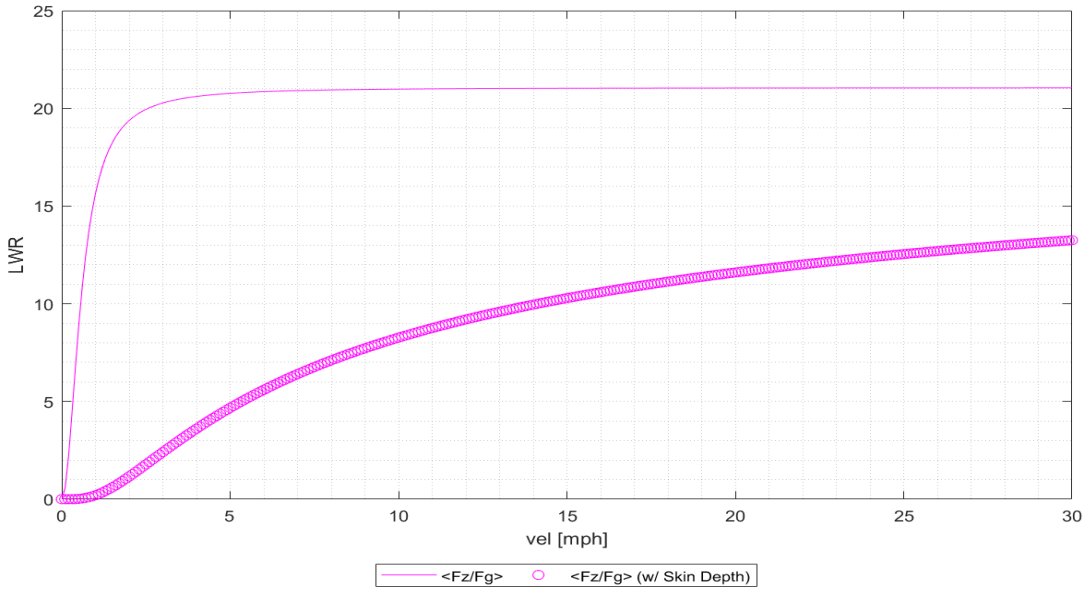

Figure 8.4. Passive maglev performance model of lift/weight versus velocity (mph). Data adapted from Post & Ryutov (1996). [30]

Figure 8.5 shows the relationship between the power loss and the linear velocity for both passive maglev cases. In the ideal case, the power loss will be expected to be at a minimum and nearly constant value of approximately $100\ W$ as velocity increases. For the non-ideal case however, there exists significant power losses as velocity increases. This is relationship is modeled after Eq. 4.23, where an increase in drag force and

velocity will lead to greater power losses. Consequently, because the drag force does not immediately go to values near zero as velocity increases, there will be a greater power loss of the system as the permanent magnets travels along the conducing slab track.

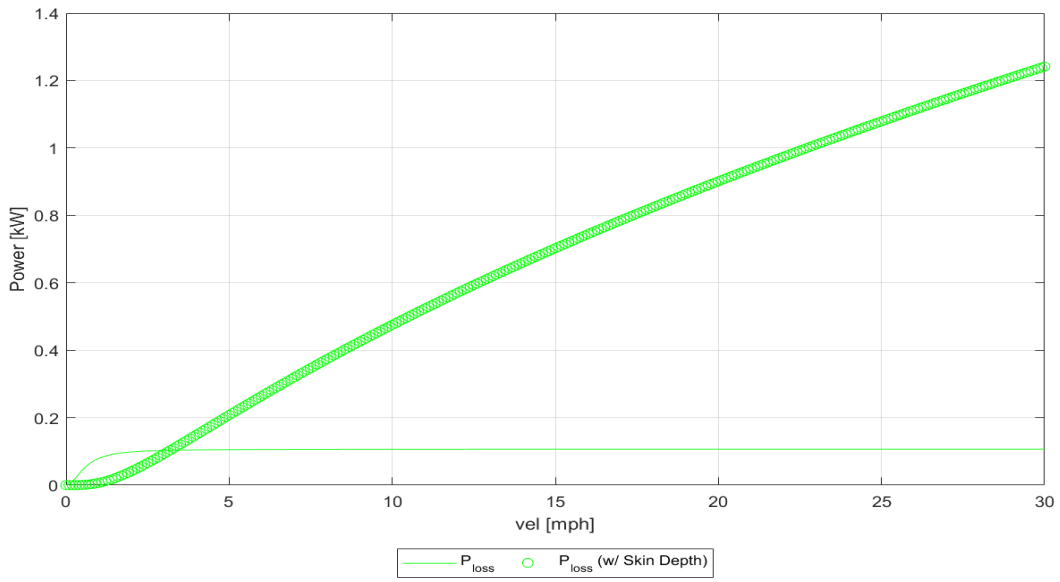

Figure 8.5. Passive maglev performance model of Power loss (W) versus velocity (mph). Data adapted from Post & Ryutov (1996). [30]

Furthermore, Figure 8.6 provides a model of the LPR versus the linear velocity of both system cases. In comparing both cases, the LPR plot further exploits the difference in efficiency between both case scenarios of the passive maglev system. Without considering skin-depth factor, a constant approximate LPR value of 3.8 N/W is expected for the system. However, in the case of the track slab, a much lower LPR in the

range between $0.2 - 0.6\ N/W$ will be expected, and will decrease as the velocity increases.

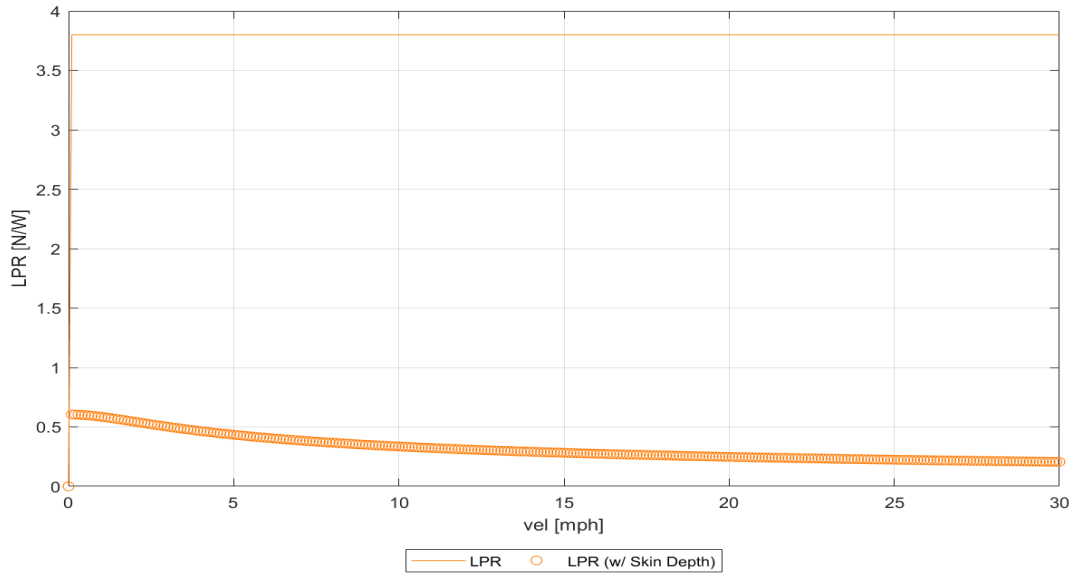

Figure 8.6. Passive maglev performance model of Lift/Power (N/W) versus velocity (mph). Data adapted from Post & Ryutov (1996). [30]

As a result, these plot results serve to show the importance of considering skin-depth as a factor for modeling a realistic performance model of the electromagnetic suspension system. In the next section, the results of the performance of the active maglev system are presented and evaluated, where the non-idealistic characteristics of the electromagnetic suspension system due to skin-depth factors are once again showcased through comparison with prototype experimental results.

CHAPTER IX

SIMULATION AND EXPERIMENTAL RESULTS OF THE ACTIVE MAGLEV SYSTEM

Simulation Methodology Overview

In modeling the active maglev system, an approach was taken where the expected theoretical results from the formulas introduced in Chapter VI are modeled against experimental results as provided by the patented active maglev hover device by *Arx-Pax* from Chapter VII. [3] From this simulation comparison, results are provided for modeling lift and drag forces, displacement gap, lift-to-drag, power loss, lift-over-power, and lift duration time versus angular velocity and displacement gap.

Furthermore, as a method to evaluate these performance tests and validate results, percentage error plots are additionally provided in Appendix D in order to show the close proximity between the theoretical and experimental results for the active maglev system.

Results of the Active Maglev System Model

In modeling all figures of merit for the active maglev system, various parameters were considered. These parameters included the size of the magnets, the types of magnets, the number of magnets used per Halbach array arrangement, the conducting track material used, the diameter of the motors and the rotary Halbach array, and the selected displacement gap between the magnets and track. These parameters additionally include the type of batteries used to power the *Hendo* board from *Arx-Pax*. A full

summary of these parameters is included in Appendix C. For the active maglev performance plots, two case scenarios were modeled: the theoretical plot results (with skin-depth factor considered) and the experimental results as provided by the *Hendo* board patent by *Arx-Pax*.

Figure 9.1 models the lift force versus angular velocity of the theoretical and experimental result comparisons.

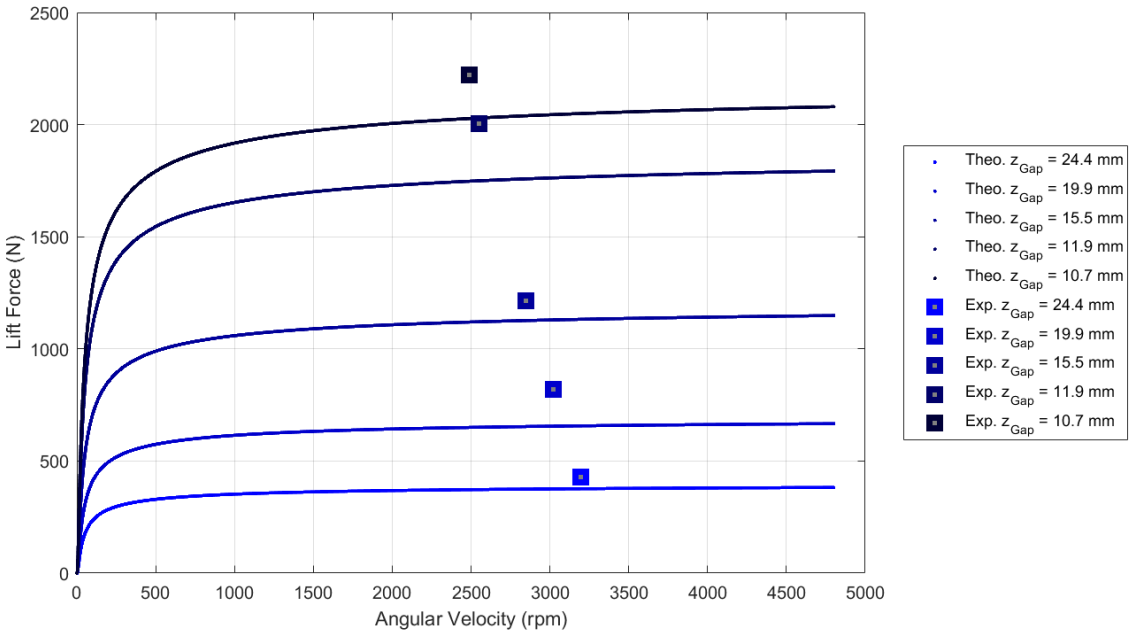

Figure 9.1. Active maglev performance model of lift (N) versus angular velocity (rpm). Data adapted from *Arx-Pax* (2015) [3] and Post & Ryutov (1996). [30]

Given that only discrete sets of experimental data were provided, much consideration was taken for understanding how the theoretical data best fits the

experimental data. In Figure 9.1, it can be seen the lift force magnitude is dependent on two variables: angular speed and the displacement gap between the magnets and the track. In general, as angular speed increases, the generated lift also increases, but not by a constant slope. In the early stages for each iteration, the generated lift increases dramatically from zero to a significantly larger force. After about $500\ RPM$, the increase in lift becomes smaller, and the lift goes to a steady-state limit as angular velocity increases. The lift is also dependent however on the displacement gap. As the displacement gap is decreased, a larger lift limit is expected to be reached, and a lower limit is reached as the gap is made larger.

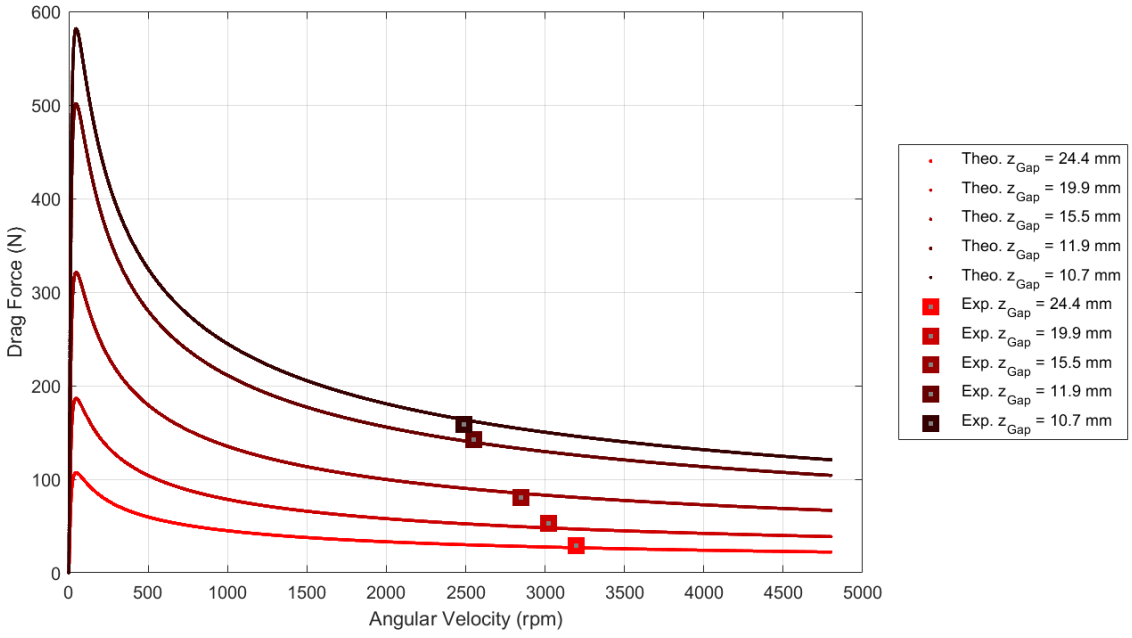

Figure 9.2. Active maglev performance model of drag (N) versus angular velocity (rpm). Data adapted from *Arx-Pax* (2015) [3] and Post & Ryutov (1996). [30]

In Figure 9.2, the electromagnetic drag force versus angular velocity is explored. Although the *Arx-Pax* patent did not provide direct data for recorded drag force, these experimental values were acquired upon taking the product of recorded power consumption values and the recorded angular speed for each iteration. [3] It can be seen that as angular speed was increased, the overall drag was found to decrease. Identically, the further the magnets were from the surface of the track surface, the smaller the drag force that was introduced into the system. Although no experimental data was recorded for early speed intervals, it is expected larger amounts of drag is experienced by the active maglev device as the theoretical data suggests.

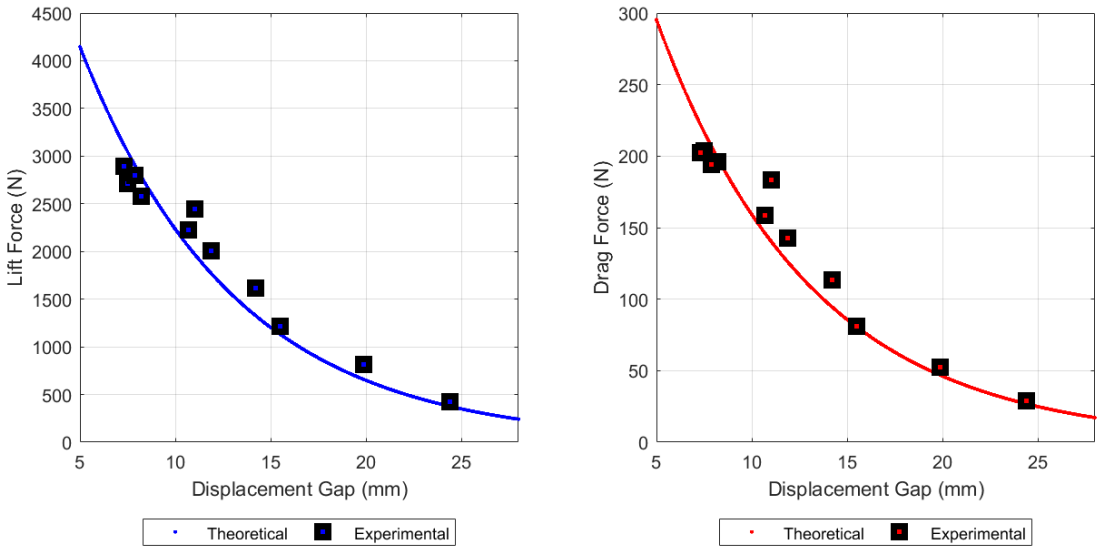

Figure 9.3. Active maglev performance model of lift and drag (N) versus displacement gap (mm). Data adapted from *Arx-Pax* (2015) [3] and Post & Ryutov (1996). [30]

The expected lift and drag forces can be further analyzed when plotted against the displacement levitation gap of the system as seen in Figure 9.3. As expected, there is a decreasing effect in the lift and drag force magnitude as the gap used in the system is increased. This shows there is indeed a tradeoff in lifting heavy loads and the displacement gap required to provide lift. However, the tradeoff is based on the expected drag that will be experienced by the system. For this reason, the generated lift and drag force ratios are modeled against angular velocity and displacement gaps in Figures 9.4 and 9.5 in order to further explore this trade-off.

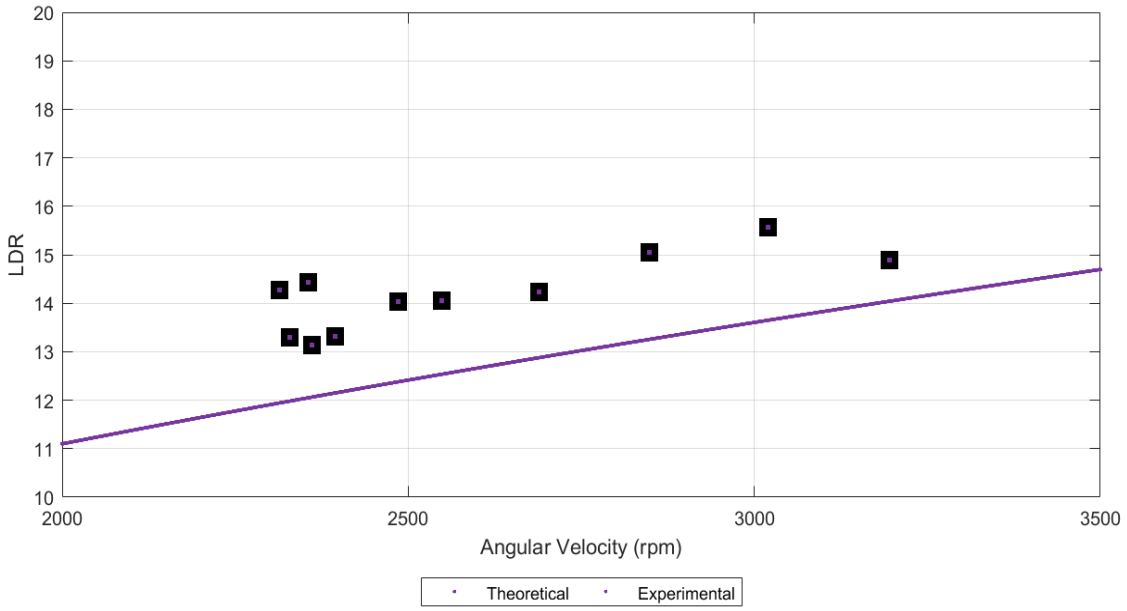

Figure 9.4. Active maglev performance model of lift/drag versus angular velocity (rpm). Data adapted from *Arx-Pax* (2015) [3] and Post & Ryutov (1996). [30]

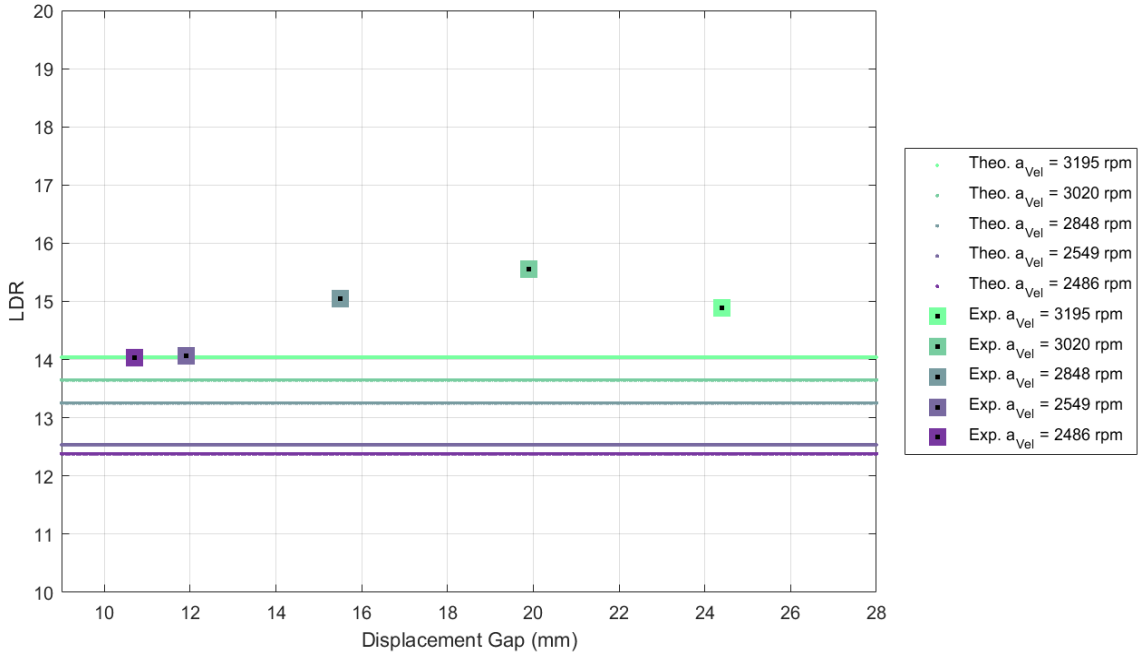

Figure 9.5. Active maglev performance model of lift/drag versus displacement gap (mm). Data adapted from *Arx-Pax* (2015) [3] and Post & Ryutov (1996). [30]

In analyzing the LDR versus the angular velocity, it is observed the active maglev system will be expected to handle more lift with less drag. Identically, an increase in the displacement gap will not affect the LDR, as the relationship remains constant when the gap is increased. Mathematically, this is because the displacement gap, Δz is part of the exponential term of both F_z and F_x formulas, which when taking the ratio of both, each end up canceling out. Figure 9.5 additionally shows that only the overall magnitude is increased as the angular speed of the rotary Halbach array is increased (as is expected based on observations from Figure 9.4).

The relationship between the displacement gap in millimeters and the angular velocity of the system is further explored in Figure 9.6. The plot further explores the relationship seen in the previous figures in showing how an increase in angular velocity increases the expected levitation gap of the system.

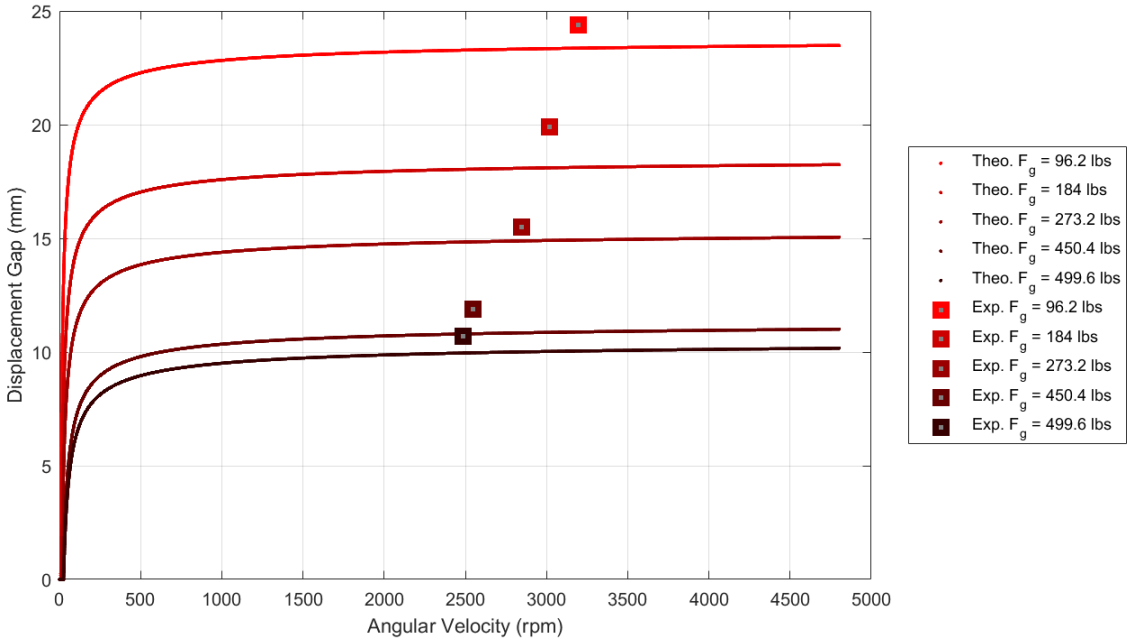

Figure 9.6. Active maglev performance model of the displacement gap (mm) versus angular velocity (rpm). Data adapted from *Arx-Pax* (2015) [3] and Post & Ryutov (1996). [30]

Identically, Figure 9.6 also shows that the weight of the payload also influences how much levitation displacement will be created by the system. In this scenario, because it is assumed the experimented active maglev device is in a balanced steady-

state levitation mode for the duration of acquired data, it is assumed $F_g = F_z$. [3, 30] That is, for this device there is clearly a limit in the lifting capability of the system as any heavier loads above $F_g \geq 500lbs$ will lead to smaller displacement gaps and ultimately result in a system exposed to larger drag force as illustrated in Figure 9.3.

Figure 9.7 shows the expected power required to operate the tested active maglev device versus angular velocity and given displacement gaps.

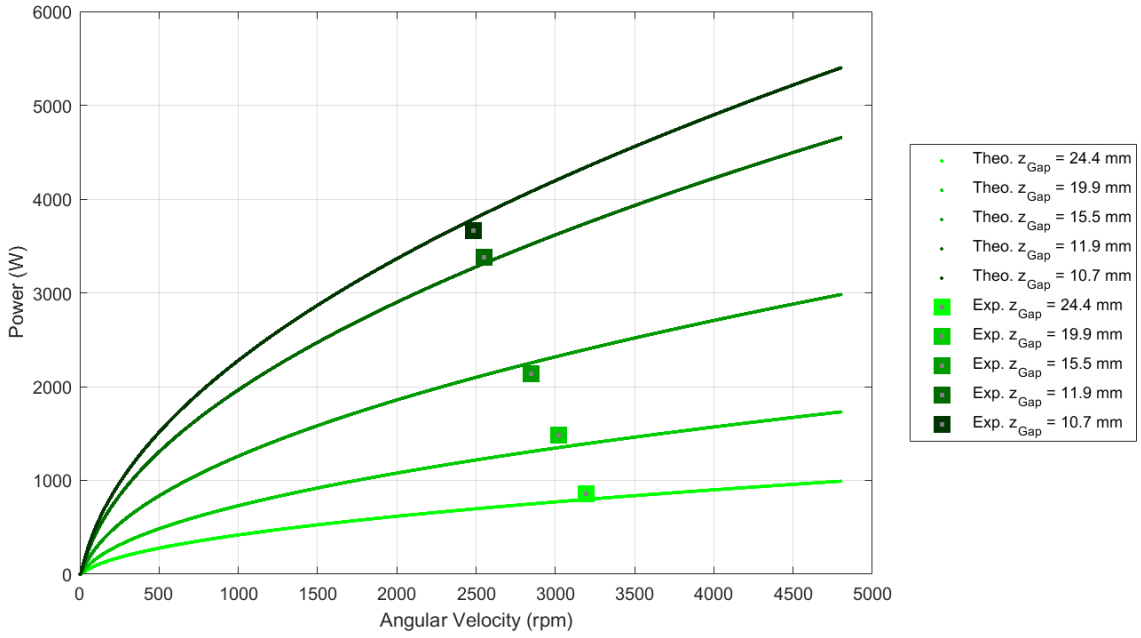

Figure 9.7. Active maglev performance model of the expected power loss (W) versus angular velocity (rpm). Data adapted from *Arx-Pax* (2015) [3] and Post & Ryutov (1996). [30]

As expected, an increasing trend in power is expected as angular velocity is increased and as the displacement gap of the system is decreased. As the displacement gap is kept too low, the theoretical power requirements show that over 5 kW of power will be required in order to power the active maglev device with a levitation gap of 10.7 mm and an angular speed of $\omega_m = 4000\ rpm$. Additionally, as the motors for the active maglev device are required to increase speed, more current will be needed in order to operate the higher speeds required for levitating the payload weight.

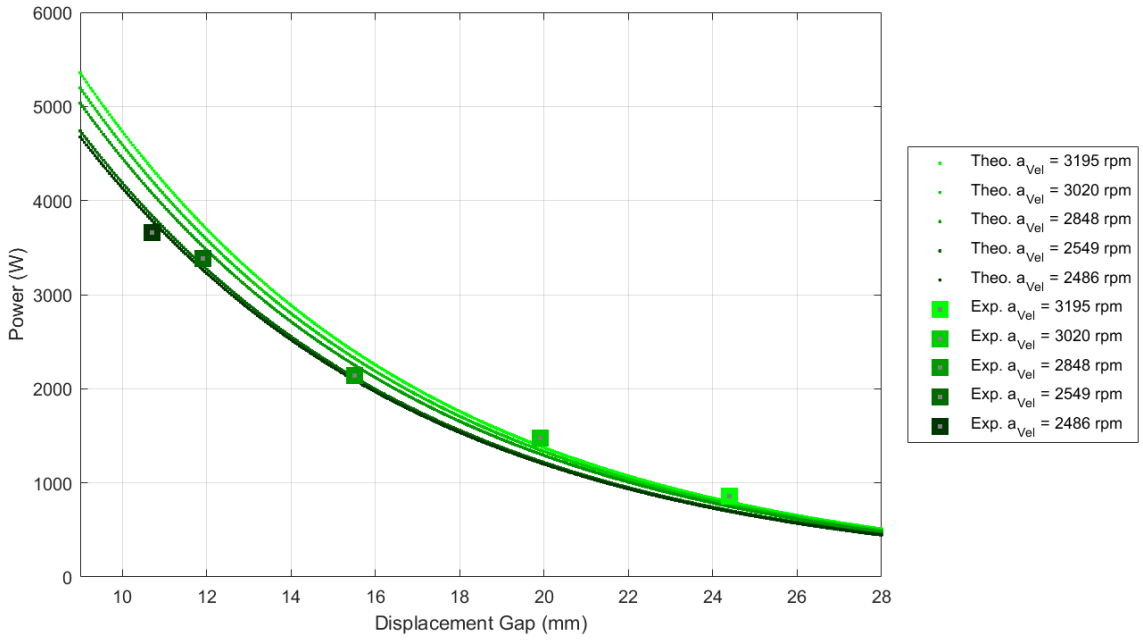

Figure 9.8. Active maglev performance model of the expected power loss (W) versus displacement gap (mm). Data adapted from *Arx-Pax* (2015) [3] and Post & Ryutov (1996). [30]

In continuing the power analysis of the active maglev electromagnetic suspension system, the power loss versus displacement gap plot proves to show that a lower displacement gap will lower the amount of power required to operate the active maglev device. Additionally, Figure 9.8 shows that lowering the angular displacement can help to lower the overall power loss of the system. However, this change is considered minimal for each iteration, essentially with larger displacement gaps.

The amount of power required for levitating a specific payload can be further analyzed by exploring how many Newtons can be lifted per Watt of power. This plot is represented in Figure 9.9.

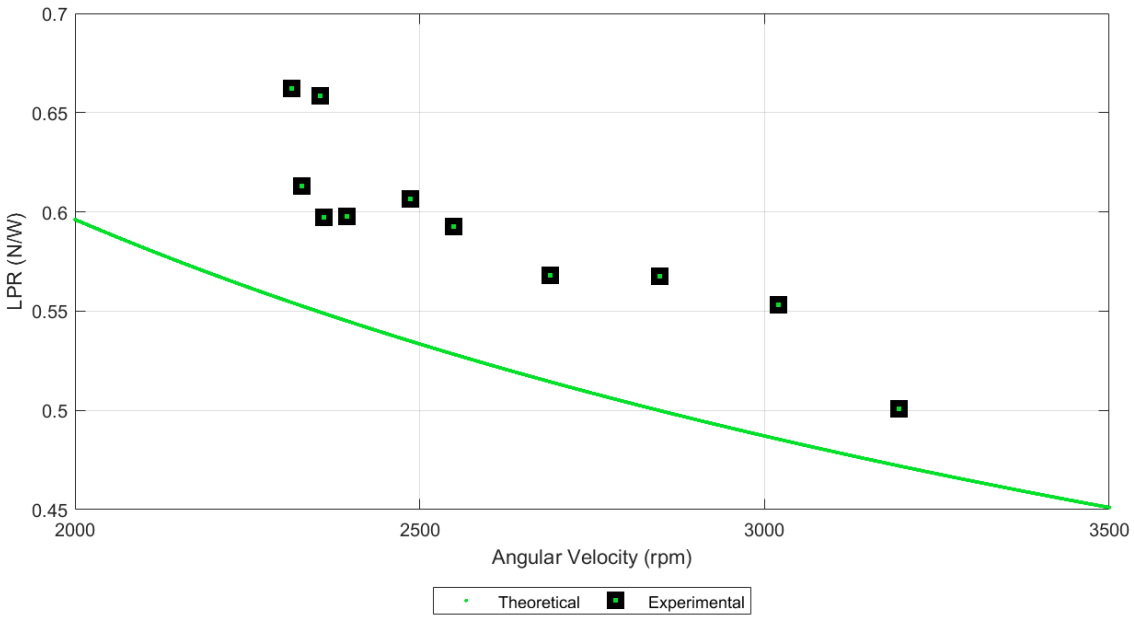

Figure 9.9. Active maglev performance model of the lift/power (N/W) versus angular velocity (rpm). Data adapted from *Arx-Pax* (2015) [3] and Post & Ryutov (1996). [30]

In Figure 9.9, a decreasing trend is seen for the LPR value as angular velocity increases. This is the case as the amount of power required to spin the motors faster is expected to increase. Additionally, because the maximum lift of the active maglev device is reached early in the velocity range, the LPR of the active maglev also decreases with greater velocity as the lifting capabilities of the device increases much more slowly though higher velocities. Figure 9.10 further studies the LPR value over the range of sweeping displacement gaps. Similarly to Figure 9.5, the LPR remains constant as did the LDR when the displacement gap increases. However, in contrast to Figure 9.5, the LPR magnitude increases primarily when the angular velocity decreases, unlike the LDR magnitude, which increases with an increase in angular velocity.

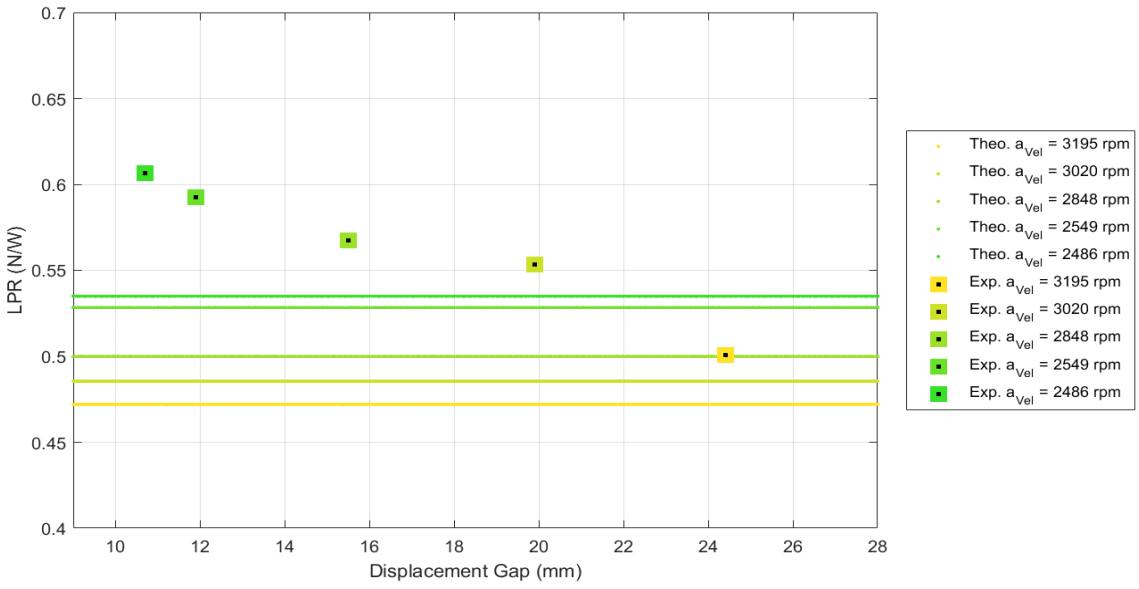

Figure 9.10. Active maglev performance model of the lift/power (N/W) versus displacement gap (mm). Data adapted from *Arx-Pax* (2015) [3] and Post & Ryutov (1996). [30]

Time Duration Performance Tests

As part of the performance tests for the active maglev suspension system, the simulation and experimental test comparisons were also used to analyze the overall time of operation for the electromagnetic suspension. As the active maglev device operates through internal battery power, it is expected to only operate for a certain amount of time until battery power runs out. According to the patent by *Arx-Pax*, the *Hendo* board operates through four $14.8V$ batteries used to power each motor. Each battery has a capacity of about $5000mAH$, where in taking a ratio of this value and the expected current for running the motors, a theoretical value for duration time can be acquired. [3]

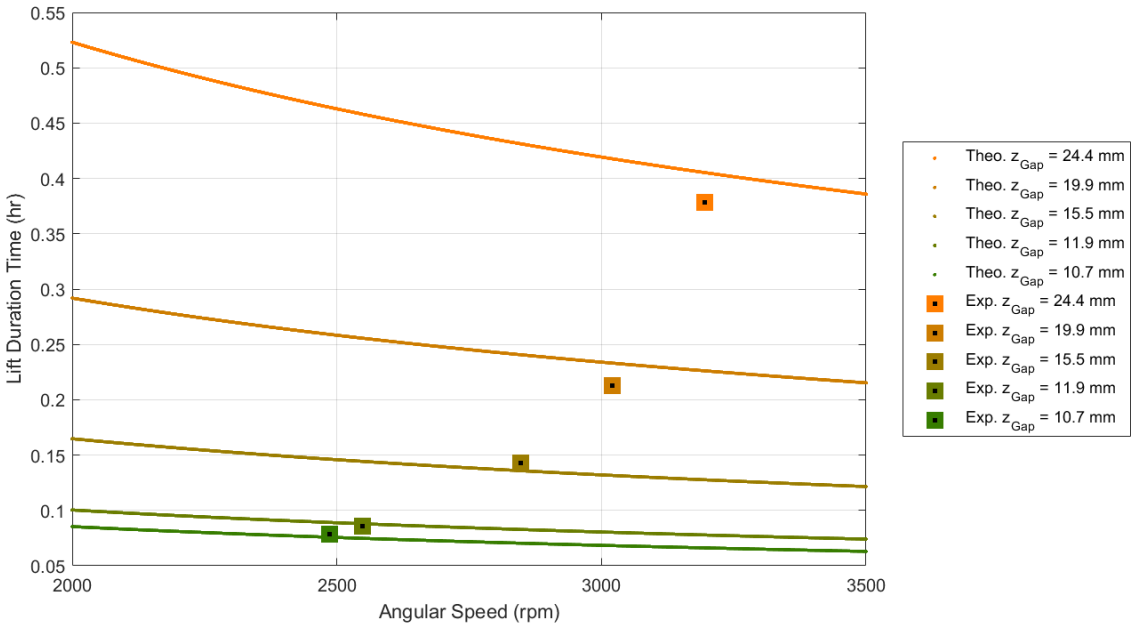

Figure 9.11. Active maglev performance model of the lift duration time (hr) versus angular speed (rpm). Data adapted from *Arx-Pax* (2015) [3] and Post & Ryutov (1996). [30]

In Figure 9.11, it is seen that the duration time for operating the active maglev device is fairly short. The theoretical data showed that in increasing the speed for each iteration, the operating time for the device will decrease. This is expected as higher speeds of the motors will require more electric current and thus, will require an increase in power consumption from the internal batteries. Additionally, the proximity of the magnets to the track will affect the operation time of the device. As the displacement gap is kept small, the closer proximity of the device to the track will generate more drag, and as a result, require more power to rotate the motors.

This is relationship is further explored in Figure 9.12. Both Figures 9.11 and 9.12 show that under a gap of $\Delta z = 24.4\ mm$, the active maglev hover device will operate for about 0.38 hours, or about 22 minutes. However, a gap $\Delta z = 10.7\ mm$ will lead to only about 4 minutes of operation with fully charged batteries!

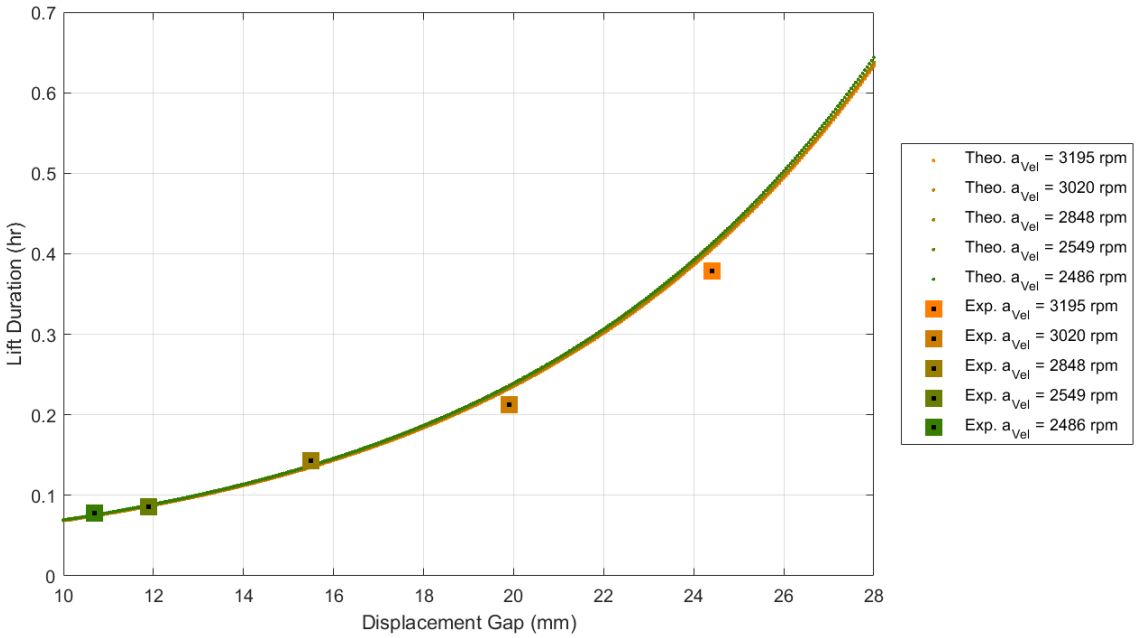

Figure 9.12. Active maglev performance model of the lift duration time (hr) versus displacement gap (mm). Data adapted from *Arx-Pax* (2015) [3] and Post & Ryutov (1996). [30]

In further exploring the operation time plots of the active maglev device, a mathematical relationship can also be found between the operation duration time and the lifting force capability as seen in Figure 9.13.

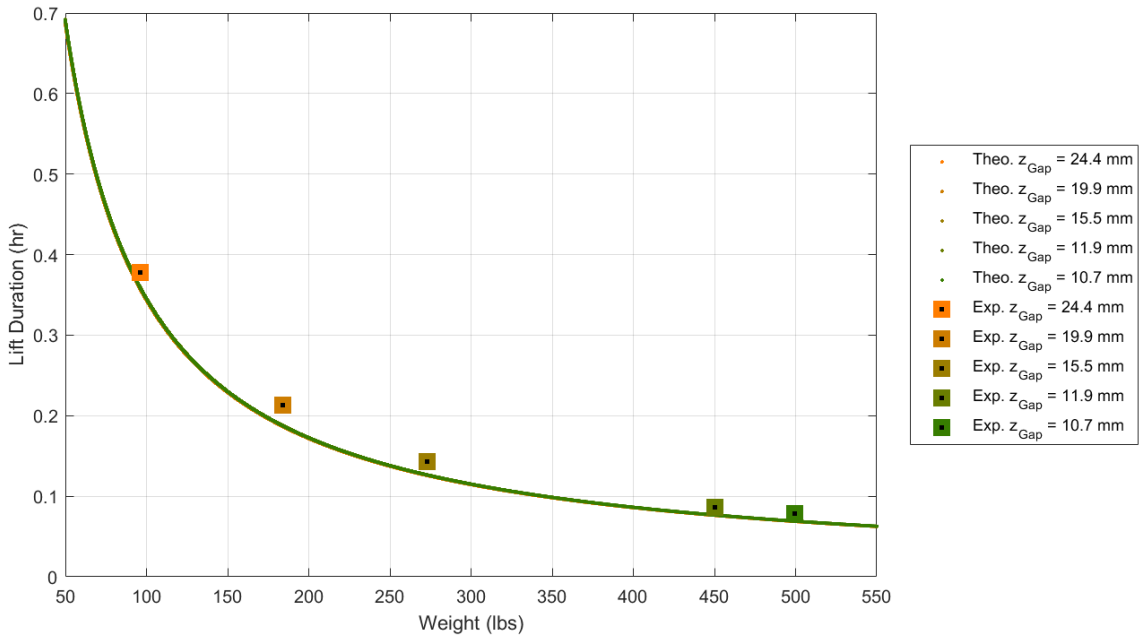

Figure 9.13. Active maglev performance model of the lift duration time (hr) versus the lifting weight capability (lbs). Data adapted from *Arx-Pax* (2015) [3] and Post & Ryutov (1996). [30]

In all, Figure 9.13 follows the observations from Figure 9.11 and 9.12. In lifting a bigger payloads, the operation time of the active maglev device will vary to a much smaller value. There is a clear relationship between the lifted payload and the displacement gap of the system. Under a larger weight, the device will be set to a closer proximity to the track surface. Through less weight, the hover device will have the capability of levitating with a larger levitation gap and experience less drag, for a result of consuming less power and consequently result in longer operating times.

CHAPTER X

TEST EVALUATIONS, CONCLUSIONS, AND EXTENSIONS

Evaluation of the Electromagnetic Suspension System

Following an overview representation of performance results of both the passive and active maglev system, it is essential to evaluate this technology for potential use of for the Hyperloop.

In all, the comparison results of the simulated results with the provided experimental data from the existing active maglev device proved as an adequate representation of the expected figures of merit performances for this technology. In terms of percent error, as an example, the smallest percentage error found was at 0.79% for the drag versus displacement gap plot, and the largest discrepancy found was at about 30% difference for the same plot. It must be noted however that all displacement gap points were acquired by hand, and thus were subjected to human error, as stated in the active maglev patented documentation from *Arx-Pax.* Power losses due to heat dissipation from the track and a voltage drop from the device's electronic components could have also caused discrepancies in recorded data. [3] A full summary plot representation of these percent errors are documented in Appendix D.

Based on the provided results, it can be concluded the electromagnetic suspension system has an inverse relationship between its lifting force capability and its duration time of operation. If requiring to lift fairly heavy loads, the operation time of the active maglev device is found to be fairly short. As in the case of the *Hendo* board,

handling a lift of about $F_g > 300lbs$, assuming $F_g = F_Z$, the duration time of operation of the electromagnetic suspension will be no more than a maximum time of 10 minutes. [3] Of course, the performance of the active maglev device is also dependent on the strength and size of the magnets used. For lifting an estimated Hyperloop capsule weight of $F_g \approx 33{,}069\ lbs$, or about $15{,}000\ kg$, heavier and larger magnets, or a large quantity of smaller-sized magnets are expected to be used if using active maglev technology. [27]

There is however a trade-off factor in cost if heavier or more magnets are used for a heavier load. As a comparison, the 1-inch cube magnets used to levitate the *Hendo* board can cost up to $30 depending on the commercial-of-the-shelf price of the market seller. [20] Table 10.1 shows an example of what a prototype using similar components to the *Hendo* board can be expected to cost.

Table 10.1. Total cost list of required components for an active maglev suspension prototype. Data adapted from Amazon (2017) [1], Hacker Motor shop (2017) [10], and K&J Magnetics (2018). [20]

Component	Price ($)	Qty	Total ($)
1in Cube Magnet	26	64	1,664
Brushless Motor	2,200	4	8,800
Batteries	130	16	2,080
		Total:	**$12,544**

Table 10.1 can be used to represent how expensive an electromagnetic suspension device can be, essentially through the requirement of permanent magnets. Because the costs increase dramatically in requiring larger sized-magnets, given the total price of over $12,000 for the *Hendo* board prototype in using 1 inch magnets (not including electronic controllers, chassis and harnesses, and any other required components), it is projected that a scale-factored suspension for the Hyperloop can be expected to reach relatively high costs and increase the overall cost of the Hyperloop design. [1, 10, 20, 27]

Furthermore, the plot results can identically be used to form conclusions in terms of the power requirements of the active maglev device. In terms of the *Hendo* board, a minimum power loss value of about $855\ W$ was recorded through a displacement gap of $24.4\ mm$, and a maximum power loss value of about $4.4kW$ was recorded through a displacement gap of $7.3\ mm$. [3] The overall power consumption of both the passive and active maglev device are dependent on the close proximity of the suspension device to the surface of the track, as a small displacement gap will lead to higher power losses due to skin-depth factor and generated heat. [30, 48] If using an electromagnetic suspension for the Hyperloop, a key to keeping a low power consumption rate will require keeping a fairly large displacement gap, which will be dependent on the vehicle's velocity and the strength of the permanent magnets.

Conclusion and Future Extensions

As a final conclusion, there is a gap in current available technology for using an electromagnetic suspension for the Hyperloop system, as based on the system's

performance and efficiency figures of merit from this investigation. In comparing this technology to that of alternate suspension methods, that is a wheel-based or aerodynamic suspension, it is expected these technologies will prove to be more efficient when comparing lifting capabilities, power consumptions factors, and overall cost construction and maintenance factors.

Consequently, the Hyperloop's potential technological design can serve to facilitate the use of an electromagnetic suspension. As an example, including the use of pressure vacuum stations for keeping a low air-pressure in the Hyperloop tube environment will allow for possible higher angular speeds for the levitation motors if using active maglev technology. As a result, this will allow for less power losses due to drag force with a higher displacement gap between the vehicle and the track surface. However, further studies are required to be conducted in order to observe the full advantages to this technological trade-off.

As a goal for future extensions, a complete analysis of the four technology suspensions is to be included as a scope for this research investigation. Upon completion of this investigation, this comparison analysis will provide the necessary quantitative and qualitative data to the scientific and engineering community for the feasibility of using each suspension type for the Hyperloop and for any other possible technological applications.

REFERENCES

[1] Amazon. (2017). *Venom 50C 4S 5000mAh 14.8V Hard Case LiPo Battery ROAR Approved with Universal Plug*. Retrieved from https://www.amazon.com/Venom-5000mAh-Battery-Approved-Universal/dp/B004805S78.

[2] Arx-Pax. (2015). *From hoverboards to flying cars, this startup has a maglev master plan*. Retrieved from http://hover.arxpax.com/media-item/hoverboards-flying-cars-startup-maglev-master-plan/.

[3] Arx-Pax LLC. (2015). *Propulsion and control for a magnetically lifted vehicle*. US 2015 0303768 A1. Retrieved from https://www.google.ch/patents/US9254759.

[4] Barber, T. J., Hiett, D., & Fastenberg, S. (2006). *CFD modeling of the hypersonic inlet starting problem*. Retrieved from https://arc.aiaa.org/doi/abs/10.2514/6.2006-123.

[5] Bhattacharrya, S., Datta, A., & Keel, L. H. (2009). *Linear control theory: Structure, robustness, and optimization*. Boca Raton, FL: CRC Press.

[6] Braun, J., Sousa, J., & Pekardan, C. (2017). *Aerodynamic design and analysis of the Hyperloop*. Retrieved from https://arc.aiaa.org/doi/abs/10.2514/1.J055634.

[7] Britannica. (2017) *Lorentz force*. Retrieved from https://www.britannica.com/science/Lorentz-force.

[8] Constine, J. (2015). *Arx-Pax demos its new steerable mag-lev hoverboard.* Retrieved from https://techcrunch.com/2015/10/21/real-hoverboard/.

[9] Gonzalez, A, Martines-Diaz, R., Cabal, E. (2005). *Mathematical model of a levitation system based on eddy currents*. Retrieved from http://ieeexplore.ieee.org/document/1644339/.

[10] Hacker Brushless Motors. (2017). *Q150-4M*. Retrieved from https://www.hacker-motor-shop.com/Brushless-Motors/Hacker-Q150/Q150-4M.htm?shop=hacker_e&SessionId=&a=article&ProdNr=10107589&p=8741.

[11] Han, Q., Ham, C., and Philips, R. (2005). *Four- and eight-piece Halbach array analysis and geometry optimization for Maglev*. Retrieved from http://ieeexplore.ieee.org/document/1436176/.

[12] Han, Q. (2004). *Analysis And Modeling Of The Eds Maglev System Based On The Halbach Permanent Magnet Array*. Retrieved from http://stars.library.ucf.edu/etd/133/.

[13] Hendo Hover. (2014). *Hendo Hoverboards - World's first REAL hoverboard*. Retrieved from https://www.kickstarter.com/projects/142464853/hendo-hoverboards-worlds-first-real-hoverboard.

[14] Hennessey Performance. (2018). *Hennessey Venom F5*. Retrieved from http://hennesseyperformance.com/vehicles/hennessey/venom-f5/.

[15] Hoburg, J., F. (2004). *Modeling maglev passenger compartment static magnetic fields from linear Halbach permanent-magnet arrays*. Retrieved from http://ieeexplore.ieee.org/document/1264123/.

[16] HyperLoopDesign. (2015). *Elon Musk says "Use wheels . . limit the number of miracles in series"*. Retrieved from https://www.hyperloopdesign.net/wheels.

[17] Hyperphysics. (2016). *Angular Velocity*. Retrieved from http://hyperphysics.phy-astr.gsu.edu/hbase/rotq.html.

[18] Karpetis, A., Swearingen, B. and Malambri, F. (2017). *Texas A&M Hyperloop*. College Station: Texas A&M University, pp.1-2,4-6.

[19] K&J Magnetics, Inc. (2003). *Halbach Arrays*. Retrieved from https://www.kjmagnetics.com/blog.asp?p=halbach-arrays/.

[20] K&J Magnetics, Inc. (2018). *Neodymium Block Magnets*. Retrieved from https://www.kjmagnetics.com/proddetail.asp?prod=BX0X0X0.

[21] Long, Z., He, G., and Xue, S. (2011). *Study of EDS & EMS hybrid suspension system with permanent-magnet Halbach array*. Retrieved from http://ieeexplore.ieee.org/abstract/document/5872046/.

[22] Liu, Z., Long, Z., & Li, X. (2015). Maglev Train Overview. *Maglev trains: Key Underlying Technologies* (pp. 3-4). New York, NY: Springer.

[23] Massachusetts Institute of Technology. (2004). *Material: Gold (PVD or electroplated).* Retrieved from http://www.mit.edu/~6.777/matprops/gold.htm.

[24] Microwaves101. (2018). *Magnetic materials*. Retrieved from https://www.microwaves101.com/encyclopedias/magnetic-materials.

[25] MIT Hyperloop. (2017). *Lift suspension*. Retrieved from http://hyperloop.mit.edu/lift-suspension.html.

[26] Murakami, A. (2015). *Halbach array 1.4 pound motor delivers 7 horsepower*. Retrieved from http://emediapress.com/category/permanent-magnets/.

[27] Musk, E. (2012). *Hyperloop Alpha*. Retrieved from http://www.spacex.com/sites/spacex/files/hyperloop_alpha-20130812.pdf.

[28] National Geographic. (2015). *Elon Musk's Hyperloop to break ground: 5 things to know*. Retrieved from https://news.nationalgeographic.com/energy/2015/06/150602-Musk-sonic-hyperloop-gets-California-stretch/.

[29] Opgenoord, M., J., Caplan, P., C. (2017). *On the aerodynamic design of the Hyperloop concept*. Retrieved from http://web.mit.edu/mopg/www/papers/OpgenoordCaplan_2017_Aerodynamics_Hyperloop_online.pdf.

[30] Post, R.F. and Ryutov, D.D. (1996). *The inductrack concept: a New Approach to Magnetic Levitation*. Retrieved from https://www.osti.gov/scitech/servlets/purl/237425.

[31] Post, R.F. and Ryutov, D.D. (2000). *The inductrack approach to magnetic levitation*. Retrieved from http://ieeexplore.ieee.org/document/828377/.

[32] Princeton. (2016). *Eddy Currents*. Retrieved from https://www.princeton.edu/ssp/joseph-henry-project/eddy-currents/eddy_wiki.pdf.

[33] Raja, V. N., Ananthababu, P., Latha, D. P., Sudha, K. R. (2015). *Design and analysis of position controlled eddy current based nonlinear magnetic levitation system using LMI*. Retrieved from http://ieeexplore.ieee.org.lib-ezproxy.tamu.edu:2048/stamp/stamp.jsp?tp=&arnumber=7432882.

[34] Rouleau, G. (2013). *Hyperloop: Not so fast!* Retrieved from http://blogs.mathworks.com/simulink/2013/11/22/hyperloop-not-so-fast/.

[35] Skytran. (2017). *Maglev*. Retrieved from http://www.skytran.com/maglev/.

[36] Storey, Jed. (2014). *Maglev Mark1 CAD upload*. Retrieved from http://mitrocketscience.blogspot.com/search/label/maglev.

[37] Tarantola, A. (2017). *The World's Fastest Ship Is Basically an Aquatic Concorde Jet.* Retrieved from https://gizmodo.com/the-worlds-fastest-boat-is-basically-an-aquatic-concor-572876759.

[38] Time Staff. (2014). *The 25 Best Inventions of 2014*. Retrieved form http://time.com/3594971/the-25-best-inventions-of-2014/

[39] Veritasium. (2017). *Electromagnetic levitation quadcopter*. Retrieved from https://www.youtube.com/watch?v=pCON4zfMzjU.

[40] Weisstein, E. W. (2018). *Sinc function*. Retrieved from http://mathworld.wolfram.com/SincFunction.html.

[41] Wikimedia Foundation, Inc. (2017). *Cruise (aeronautics)*. Retrieved from https://en.wikipedia.org/wiki/Cruise_(aeronautics).

[42] Wikimedia Foundation, Inc. (2017). *Electrical resistivity and conductivity*. Retrieved from https://en.wikipedia.org/wiki/Electrical_resistivity_and_conductivity.

[43] Wikimedia Foundation, Inc. (2017). *Halbach array*. Retrieved from https://en.wikipedia.org/wiki/Halbach_array.

[44] Wikimedia Foundation, Inc. (2018). *Lenz's law*. Retrieved from https://en.wikipedia.org/wiki/Lenz%27s_law.

[45] Wikimedia Foundation, Inc. (2018). *Maglev*. Retrieved from https://en.wikipedia.org/wiki/Maglev.

[46] Wikimedia Foundation, Inc. (2017). *Permeability (electromagnetism)*. Retrieved from https://en.wikipedia.org/wiki/Permeability_(electromagnetism).

[47] Wikimedia Foundation, Inc. (2018). *Orders of magnitude (magnetic field)*. Retrieved from https://en.wikipedia.org/wiki/Orders_of_magnitude_(magnetic_field).

[48] Wikimedia Foundation, Inc. (2018). *Skin effect*. Retrieved from https://en.wikipedia.org/wiki/Skin_effect.

[49] World Economic Forum. (2018). *These are the world's fastest trains*. Retrieved from https://www.weforum.org/agenda/2017/09/these-are-the-world-s-fastest-trains/.

APPENDIX A

DETAILED DERIVATION OF FORMULAS

Appendix A-1 Derivation of Induced Magnetic Flux of the Halbach Array

$$\Rightarrow \vec{\emptyset}_x(t) = \iint_S \vec{B}_x(t) \cdot ds\,, \qquad (\omega t = kx)$$

$$= \iint_{y,z} B_0 \sin(kx)\, e^{-k\Delta z} \cdot dydz$$

$$= \int_{z=-h_c}^{0} \int_{0}^{y=w_c} B_0 sin(kx) e^{-k\Delta z} \cdot dydz$$

$$= \int_{z=-h_c}^{0} wB_0\, sin(kx)\, e^{-k\Delta z} \cdot dz, \qquad |w = w_c$$

$$= \int_{z=-h_c}^{0} w_c B_0\, sin(kx)\, e^{-k\Delta z} \cdot dz\,, \qquad (\Delta z = \Delta z - z)$$

$$= w_c B_0\, sin(kx)\, e^{-k\Delta z} \int_{z=-h_c}^{0} e^{kz} \cdot dz$$

$$= w_c B_0\, sin(kx)\, e^{-k\Delta z} [\frac{1}{k}(1 - e^{-kh_c})]$$

$$= \frac{w_c B_0}{k} sin(kx) e^{-k\Delta z}(1 - e^{-kh_c})$$

- Final Solution adapted from Post & Ryutov © 2000 IEEE. [31]

Appendix A-2 Derivation of Induced Eddy Currents due to Halbach Array

$$\Rightarrow V_{\emptyset}(t) = -\frac{\partial \emptyset_x}{\partial t}$$

$$= \omega \phi_x cos(\omega t)$$

$$= L_c \frac{di_e(t)}{dt} + R_c i_e(t)$$

$\Longrightarrow Apply\ Laplace\ Transform$:

$$sL_c I_e(s) + R_c I_e(s) = \omega \phi_x \frac{s}{s^2 + \omega^2}$$

$$I_e(s)(sL_c + R_c) = \omega \phi_x \frac{s}{s^2 + \omega^2}$$

$$\Rightarrow I_e(s) = \frac{\omega \phi_x}{L_c}\left(\frac{1}{s + R_c/L_c}\right)\left(\frac{s}{s^2 + \omega^2}\right)$$

$\Longrightarrow Apply\ Partial\ Fraction\ Decomposition$:

$$\frac{\omega \phi_x}{L_c}\left(\frac{1}{s + R_c/L_c}\right)\left(\frac{s}{s^2 + \omega^2}\right) = \frac{\omega \phi_x}{L_c}\left[\frac{\alpha}{s + R_c/L_c} + \frac{\beta s + \gamma}{s^2 + \omega^2}\right]$$

$$s = \alpha(s^2 + \omega^2) + (\beta s + \gamma)(s + R_c/L_c)$$

$$s = (\alpha + \beta)s^2 + \left(\beta \frac{R_c}{L_c} + \gamma\right)s + (\alpha \omega^2 + \gamma \frac{R_c}{L_c})$$

$$\begin{cases} 0 = \alpha + \beta \\ 1 = \beta \frac{R_c}{L_c} + \gamma \\ 0 = \alpha \omega^2 + \gamma \frac{R_c}{L_c} \end{cases} \Longrightarrow \begin{cases} \alpha = \left(\frac{1}{\omega^2}\right)\frac{-R_C/L_C}{1 + (R_C/\omega L_C)^2} \\ \beta = \left(\frac{1}{\omega^2}\right)\frac{R_C/L_C}{1 + (R_C/\omega L_C)^2} \\ \gamma = \left(\frac{1}{\omega^2}\right)\frac{\omega^2}{1 + (R_C/\omega L_C)^2} \end{cases}$$

$$\Rightarrow I_e(s) = \frac{\phi_x}{L_c}\left[\frac{-R_C/\omega L_C}{1+(R_C/\omega L_C)^2}\left(\frac{1}{s+R_c/L_c}\right) + \frac{R_C/\omega L_C}{1+(R_C/\omega L_C)^2}\left(\frac{s}{s^2+\omega^2}\right) + \frac{1}{1+(R_C/\omega L_C)^2}\left(\frac{\omega}{s^2+\omega^2}\right)\right]$$

$\Longrightarrow Apply\ Inverse\ Laplace\ Transform$:

$$\Rightarrow i_e(t) = \frac{\phi_x}{L_c}\left[\frac{-R_C/\omega L_C}{1+(R_C/\omega L_C)^2}e^{-\frac{R_c}{L_c}t} + \frac{R_C/\omega L_C}{1+(R_C/\omega L_C)^2}cos(\omega t) + \frac{1}{1+(R_C/\omega L_C)^2}sin(\omega t)\right]$$

$$= \frac{\phi_x}{L_c}\left(\frac{1}{1+(R_C/\omega L_C)^2}\right)\left[sin(\omega t) + \left(\frac{R_c}{L_c\omega}\right)(cos(\omega t) - e^{-\frac{R_c}{L_c}t})\right], \quad (e^{-\frac{R_c}{L_c}t} \longrightarrow 0, neglected)$$

$$= \frac{\phi_x}{L_c}\left(\frac{1}{1+(R_C/\omega L_C)^2}\right)\left[sin(\omega t) + \left(\frac{R_c}{L_c\omega}\right)cos(\omega t)\right]$$

- Final Solution adapted from Post & Ryutov © 2000 IEEE. [31]

Appendix A-3 Derivation of Average Lift Force due to Halbach Array

$$\Rightarrow < F_z > = \frac{1}{T}\int_0^T \vec{F}_z(t)\, dt\,, \qquad (T = \frac{2\pi}{\omega})$$

$$= \frac{1}{T}\int_0^T w_c \vec{I}_y(t)\vec{B}_x(t)\, dt$$

$$= \frac{1}{T}\int_0^T \frac{{w_c}^2 {B_0}^2}{kL_c}\left(\frac{1}{1+(R_C/\omega L_C)^2}\right) e^{-2k\Delta z}[sin^2(\omega t) + \left(\frac{R_c}{L_c\omega}\right) sin(\omega t)\, cos(\omega t)]\, dt$$

$$\Longrightarrow Let\ \alpha = \frac{{w_c}^2 {B_0}^2}{kL_c}\left(\frac{1}{1+(R_C/\omega L_C)^2}\right) e^{-2k\Delta z}$$

$$= \frac{\alpha}{T}\int_0^T [sin^2(\omega t) + \left(\frac{R_c}{L_c\omega}\right) sin(\omega t)\, cos(\omega t)]\, dt$$

$$= \frac{\alpha}{T}[\int_0^T sin^2(\omega t)\, dt + \left(\frac{R_c}{L_c\omega}\right)\int_0^T sin(\omega t)\, cos(\omega t)\, dt]$$

$$= \frac{\alpha}{T}\int_0^T sin^2(\omega t)\, dt + 0,$$

$$(2^{nd} integral\ term \longrightarrow 0, after\ applying\ limits)$$

$$= \frac{\alpha}{T}\int_0^T sin^2(\omega t)\, dt = \frac{\alpha}{2T}\int_0^T [1-\cos(2\omega t)]dt$$

$$= \frac{\alpha}{2T}[\int_0^T dt - \int_0^T \cos(2\omega t)\, dt]$$

$$= \quad \frac{\alpha}{2T}\left[\int_0^T dt - 0\right]$$

$$(2^{nd} integral\ term \longrightarrow 0, after\ applying\ limits)$$

$$= \quad \frac{\alpha}{2T}(T) = \frac{\alpha}{2}$$

$$= \quad \frac{{w_c}^2 {B_0}^2}{2kL_c}\left(\frac{1}{1+(R_C/\omega L_C)^2}\right)e^{-2k\Delta z}$$

- Final Solution adapted from Post & Ryutov © 2000 IEEE. [31]

Appendix A-4 Derivation of Average Drag Force due to Halbach Array

$$\Rightarrow < F_x > = \frac{1}{T}\int_0^T \vec{F}_x(t)\, dt\,, \qquad (T = \frac{2\pi}{\omega})$$

$$= \frac{1}{T}\int_0^T w_c \vec{I}_y(t)\vec{B}_z(t)\, dt$$

$$= \frac{1}{T}\int_0^T \frac{{w_c}^2 {B_0}^2}{kL_c}\left(\frac{1}{1+(R_C/\omega L_C)^2}\right) e^{-2k\Delta z}[sin(\omega t)\, cos(\omega t) + \left(\frac{R_c}{L_c\omega}\right) cos^2(\omega t)]\, dt$$

$$\Longrightarrow Let\ \alpha = \frac{{w_c}^2 {B_0}^2}{kL_c}\left(\frac{1}{1+(R_C/\omega L_C)^2}\right) e^{-2k\Delta z}$$

$$= \frac{\alpha}{T}\int_0^T [sin(\omega t)\, cos(\omega t) + \left(\frac{R_c}{L_c\omega}\right) cos^2(\omega t)]\, dt$$

$$= \frac{\alpha}{T}[\int_0^T sin(\omega t)\, cos(\omega t)\, dt + \left(\frac{R_c}{L_c\omega}\right)\int_0^T cos^2(\omega t)\, dt]$$

$$= \frac{\alpha}{T}[0 + \left(\frac{R_c}{L_c\omega}\right)\int_0^T cos^2(\omega t)\, dt],$$

$$(1^{st} integral\ term \longrightarrow 0, after\ applying\ limits)$$

$$= \frac{\alpha R_c}{TL_c\omega}\int_0^T cos^2(\omega t)\, dt = \frac{\alpha R_c}{TL_c\omega}\int_0^T [1 - sin^2(\omega t)]dt$$

$$= \frac{\alpha R_c}{TL_c\omega}\int_0^T [1 - \frac{1}{2} + \frac{1}{2}\cos(2\omega t)]dt$$

$$= \frac{\alpha R_c}{2TL_c\omega}[\int_0^T dt + \frac{1}{2}\int_0^T \cos(2\omega t)]dt$$

$$= \frac{\alpha R_c}{2TL_c\omega}\left[\int_0^T dt + 0\right],$$

$$(2^{nd} integral\ term \longrightarrow 0, after\ applying\ limits)$$

$$= \frac{\alpha R_c}{2TL_c\omega}(T) = \frac{\alpha}{2}\left(\frac{R_c}{L_c\omega}\right)$$

$$= \frac{{w_c}^2{B_0}^2}{2kL_c}\left(\frac{(R_C/\omega L_C)}{1+(R_C/\omega L_C)^2}\right)e^{-2k\Delta z}$$

- Final Solution adapted from Post & Ryutov © 2000 IEEE. [31]

Appendix A-5 Derivation of Maximum Lift Force (Flat-Track Design)

$$\Rightarrow < F_z > = \frac{{w_c}^2 {B_0}^2}{2kL_c}\left(\frac{1}{1+(R_C/\omega L_C)^2}\right)e^{-2k\Delta z}$$

$$\Longrightarrow Let\ L_c = \frac{\mu_0 P_c}{2k\lambda}\ and\ let\ P_c = w_c$$

$$= \frac{w_c \lambda {B_0}^2}{\mu_0}\left(\frac{1}{1+(R_C/\omega L_C)^2}\right)e^{-2k\Delta z}$$

$$\Longrightarrow Let\ A = w_c\lambda$$

$$= \frac{A{B_0}^2}{\mu_0}\left(\frac{1}{1+(R_C/\omega L_C)^2}\right)e^{-2k\Delta z}$$

$$\Rightarrow < \frac{F_z}{A} > = \frac{{B_0}^2}{\mu_0}\left(\frac{1}{1+(R_C/\omega L_C)^2}\right)e^{-2k\Delta z}$$

$$\Longrightarrow Apply\ L'Hopital's\ Rule\ for\ finding\ \frac{F_{z_{max}}}{A}\ as\ \omega \to \infty:$$

$$\Rightarrow < \frac{F_{z_{max}}}{A} > = \lim_{\omega\to\infty} < \frac{F_z}{A} > = \lim_{\omega\to\infty}\left(\frac{{B_0}^2}{\mu_0}\left(\frac{1}{1+(R_C/\omega L_C)^2}\right)e^{-2k\Delta z}\right)$$

$$= \frac{{B_0}^2}{\mu_0}\left(\frac{1}{1+0}\right)e^{-2k\Delta z}$$

$$= \frac{{B_0}^2}{\mu_0}e^{-2k\Delta z}$$

- Final Solution adapted from Post & Ryutov © 2000 IEEE. [31]

Appendix A-6 Derivation of Halbach Array Optimized Dimensions for Max LWR

- ***Solving for Optimized Depth:***

$$\Rightarrow < \frac{F_{z_{max}}}{F_g} > = \quad \frac{AB_0^2\mu_0^{-1}}{pw\lambda dg} e^{-2k\Delta z}$$

$$\Longrightarrow Let\ B_0 = B_r\left[1 - e^{-kd}\right] \operatorname{sinc}\left(\frac{\pi}{M}\right), k = \frac{2\pi}{\lambda}, and\ A = w\lambda$$

$$= \quad \mu_0^{-1} {B_r}^2 \left(1 - e^{-\frac{2\pi}{\lambda}d}\right)^2 \operatorname{sinc}^2\left(\frac{\pi}{M}\right)(pdg)^{-1} e^{-\frac{4\pi}{\lambda}\Delta z}$$

$$\Longrightarrow Let\ \alpha = \mu_0^{-1} {B_r}^2 \operatorname{sinc}^2\left(\frac{\pi}{M}\right) e^{-\frac{4\pi}{\lambda}\Delta z}(pg)^{-1}$$

$$= \quad \alpha\left(1 - e^{-\frac{2\pi}{\lambda}d}\right)^2 d^{-1}$$

$$\Rightarrow \frac{d(F_{z_{max}}/A)(d)}{d(d)} = \quad 2\alpha\left(-\frac{2\pi}{\lambda}e^{-\frac{2\pi}{\lambda}d}\right)\left(1 - e^{-\frac{2\pi}{\lambda}d}\right)d^{-1} - \alpha\left(1 - e^{-\frac{2\pi}{\lambda}d}\right)^2 d^{-2}$$

$$= \quad 0$$

$\Longrightarrow Cancelling\ light\ terms\ and\ solving\ for\ d_{opt}$:

$$\Rightarrow d_{opt} = \quad \frac{1}{5}\lambda$$

- Final Solution adapted from Post & Ryutov © 2000 IEEE. [31]

- ***Solving for Optimized Lambda:***

$$\Rightarrow < \frac{F_{z_{max}}}{F_g} > = \quad \frac{AB_0^2\mu_0^{-1}}{pw\lambda dg} e^{-2k\Delta z}$$

$$\Longrightarrow Let\ B_0 = B_r\left[1 - e^{-kd}\right] \operatorname{sinc}\left(\frac{\pi}{M}\right), k = \frac{2\pi}{\lambda}, d = d_{opt} = \frac{1}{5}\lambda, and\ A = w\lambda$$

$$= \quad \mu_0^{-1} {B_r}^2 \left(1 - e^{-\frac{2\pi}{5}}\right)^2 \operatorname{sinc}^2\left(\frac{\pi}{M}\right)\left(\frac{1}{5}p\lambda g\right)^{-1} e^{-\frac{4\pi}{\lambda}\Delta z}$$

$$\Longrightarrow Let\ \beta = \mu_0^{-1} {B_r}^2 \left(1 - e^{-\frac{2\pi}{5}}\right)^2 \operatorname{sinc}^2\left(\frac{\pi}{M}\right)\left(\frac{1}{5}pg\right)^{-1}$$

$$= \quad \beta\lambda^{-1} e^{-\frac{4\pi}{\lambda}\Delta z}$$

$$\Rightarrow \frac{d(F_{z_{max}}/A)(\lambda)}{d(\lambda)} = \quad -\beta\lambda^{-2} e^{-\frac{4\pi}{\lambda}\Delta z} + \beta\lambda^{-1}\left(\frac{4\pi}{\lambda^2}\Delta z\right) e^{-\frac{4\pi}{\lambda}\Delta z}$$

$$= \quad 0$$

$\Longrightarrow Cancelling\ light\ terms\ and\ solving\ for\ \lambda_{opt}$:

$$\Rightarrow \lambda_{opt} = \quad 4\pi\Delta z$$

- Final Solution adapted from Post & Ryutov © 2000 IEEE. [31]

Appendix A-7 Derivation of Halbach Array Frequency of Maximum Drag Force

$$\Rightarrow < F_x > = \quad \frac{{w_c}^2 {B_0}^2}{2kL_c}\left(\frac{(R_C/\omega L_C)}{1+(R_C/\omega L_C)^2}\right)e^{-2k\Delta z}$$

$$\Longrightarrow Let\ \alpha = \frac{{w_c}^2 {B_0}^2}{kL_c}e^{-2k\Delta z}$$

$$= \quad \alpha R_C \omega^{-1} {L_C}^{-1}\left(1+\left(R_C\omega^{-1}{L_C}^{-1}\right)^2\right)^{-1}$$

$$\Rightarrow \frac{dF_x(\omega)}{d\omega} = \quad -\alpha R_C\omega^{-2}{L_C}^{-1}\left(1+\left(R_C\omega^{-1}{L_C}^{-1}\right)^2\right)^{-1}$$

$$- \alpha R_C\omega^{-1}{L_C}^{-1}\left(1\right.$$

$$\left.+\left(R_C\omega^{-1}{L_C}^{-1}\right)^2\right)^{-2}\left(-2{R_C}^2\omega^{-3}{L_C}^{-2}\right)$$

$$= \quad 0$$

$\Longrightarrow Cancelling\ light\ terms\ and\ solving\ for\ \omega$:

$$\Rightarrow \omega = \quad \frac{R_c}{L_c}$$

- Final Solution adapted from Post & Ryutov © 2000 IEEE. [31]

APPENDIX B

VARIOUS SOLUTIONS OF THE ELECTROMAGNETIC SUSPENSION SYSTEM

Table B.1. Maximum Force Limits. Adapted from Post & Ryutov © 2000 IEEE. [31]

Maximum F_z $(\omega \longrightarrow \infty)$	$\frac{B_0^2 {w_c}^2}{2kL_c} e^{-2k\Delta z}$
Maximum F_z per area [Ideal Flat Track Design] $(\omega \longrightarrow \infty)$	$\frac{B_0^2}{\mu_0} e^{-2k\Delta z}$
Maximum F_x $(\omega \longrightarrow \infty)$	0

Table B.2. Optimization Dimensions for Maximum LWR. Adapted from Post & Ryutov © 2000 IEEE. [31]

Optimized Depth (d_{opt})	$\frac{1}{5}\lambda$
Optimized Lambda (λ_{opt})	$4\pi\Delta z$
Maximum LWR $(\Delta z = 3\ cm)$	$50{:}1$

Table B.3. Frequency and Velocity Terms for Maximum Drag. Adapted from Post & Ryutov © 2000 IEEE. [31]

Halbach Array Frequency for Maximum Drag	${R_c}/{L_c}$
Halbach Array Velocity for Maximum Drag	$\frac{R_c}{kL_c}$

APPENDIX C

PARAMETERS USED FOR ELECTROMAGNETIC SUSPENSION TESTS

Table C.1. Parameters for the passive maglev simulation test. Adapted from Post & Ryutov (1996) [30], and K&J Magnetics (2018). [20]

Magnet Properties	
Material	Neodymium (NdFeB)
Width (w)	2.54 cm (1 in)
Depth (d)	2.54 cm
Length (l)	2.54 cm
Lambda (λ)	10.2 cm (4 in)
No. Magnets/Halbach Array (M)	4
Halbach Array Magnetic Peak (B_0)	1.01 T
Halbach Array Wave Number (k)	61.8 m^{-1}
Magnet Velocity (v)	0 - 30 mph (0 - 13.4 m/s)
Displacement Gap (Δz)	2.44 cm
Track Properties	
Material	Aluminum
Thickness (Δc)	9.52 mm (0.375in)
Resistance (R)	0.17 $\mu\Omega$
Inductance (L)	10.2 nH

Table C.2. Parameters for the active maglev simulation test. Adapted from Post & Ryutov (1996) [30], and K&J Magnetics (2018). [20]

Magnet/Motor Properties	
Material	Neodymium (NdFeB)
Width (w)	2.54 cm (1 in)
Depth (d)	2.54 cm
Length (l)	2.54 cm
Lambda (λ)	10.2 cm (4 in)
No. Magnets/Halbach Array (M)	4
Total Magnets/Rotary Halbach Array	16 (64 total per device)
Halbach Array Magnetic Peak (B_0)	1.01 T
Halbach Array Wave Number (k)	61.8 m^{-1}
Outer Motor Diameter	21.59 cm (8.5 in)
Inner Motor Diameter	17.78 cm (7 in)
Magnet Angular Velocity (ω)	0 - 4000 rpm (0 - 418.88 rad/s)
Displacement Gap (Δz)	$0 - 30$ mm
Track Properties	
Material	Copper
Thickness (Δc)	9.52 mm (0.375in)
Resistance (R)	0.17 $\mu\Omega$
Inductance (L)	10.2 nH

APPENDIX D

PERCENT ERROR PLOTS FOR ACTIVE MAGLEV PERFORMANCE TESTS

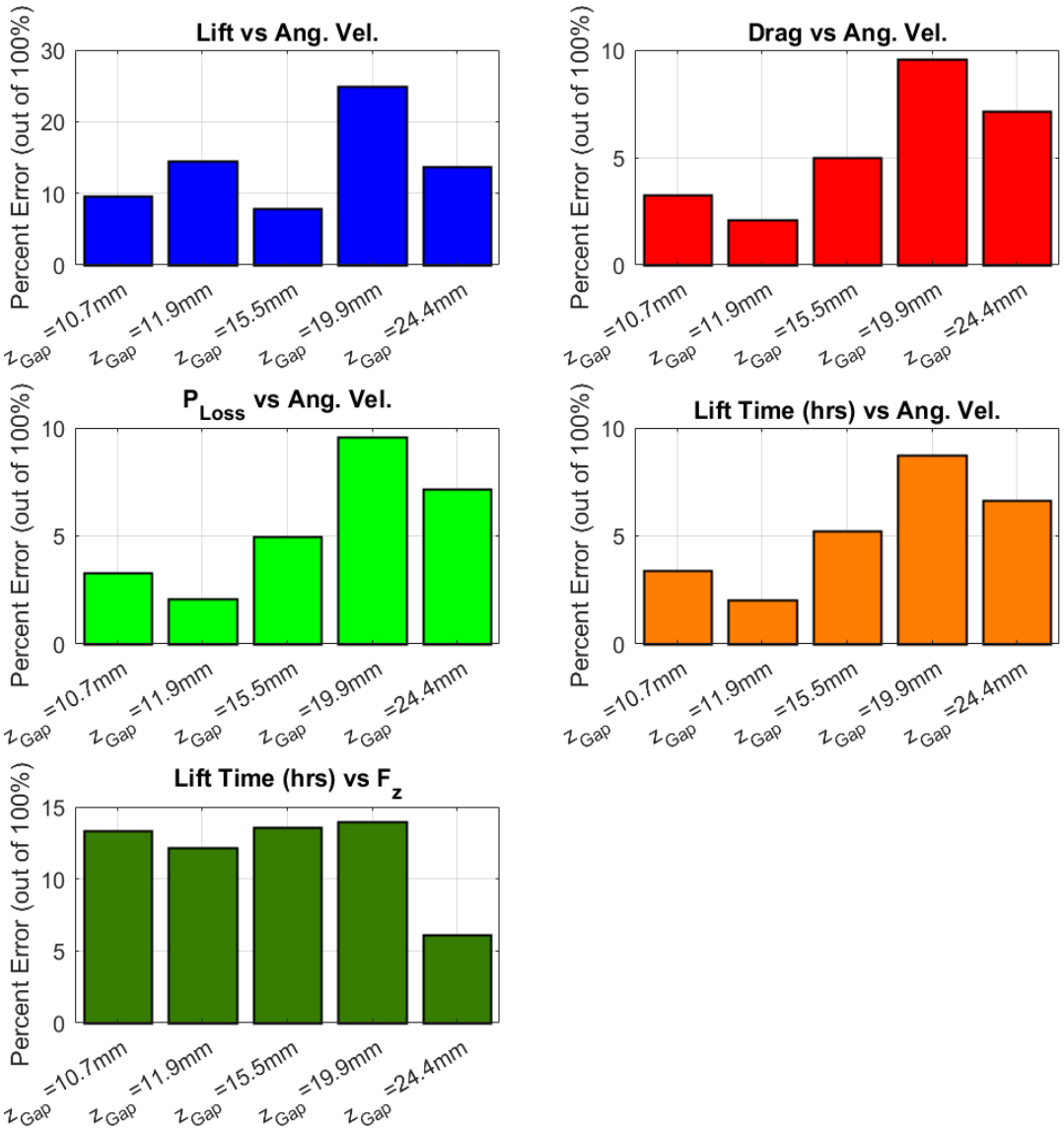

Figure D.1(a)-(e). Percent error of theoretical versus experimental plots at given displacement gaps. Data adapted from *Arx-Pax* (2015) [3] and Post & Ryutov (1996). [30]

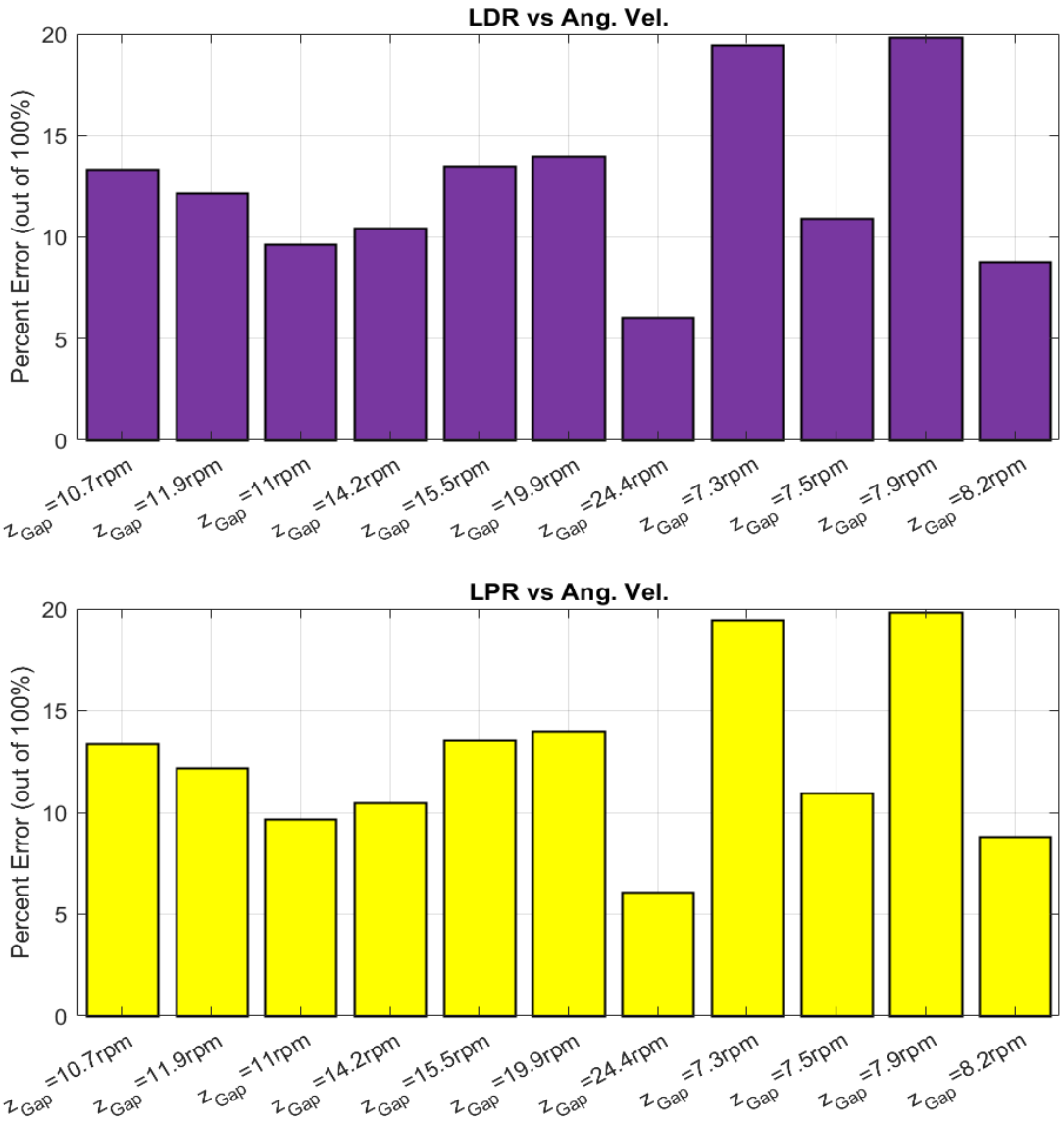

Figure D.2(a)-(b). Percent error of theoretical versus experimental plots of the lift/drag and lift/power ratios at given displacement gaps. Data adapted from *Arx-Pax* (2015) [3] and Post & Ryutov (1996). [30]

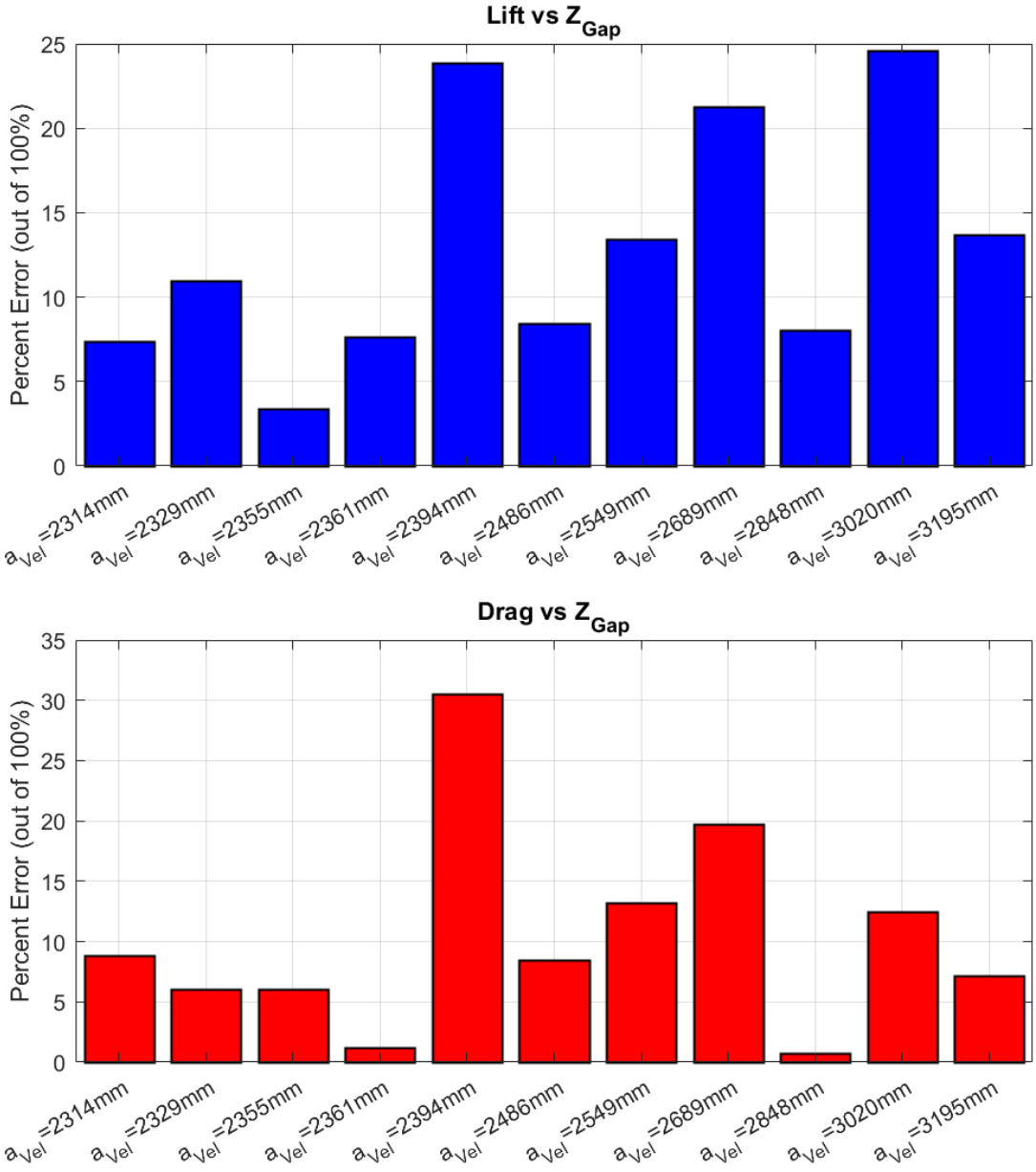

Figure D.3(a)-(b). Percent error of theoretical versus experimental plots of the lift and drag forces at given angular velocities. Data adapted from *Arx-Pax* (2015) [3] and Post & Ryutov (1996). [30]

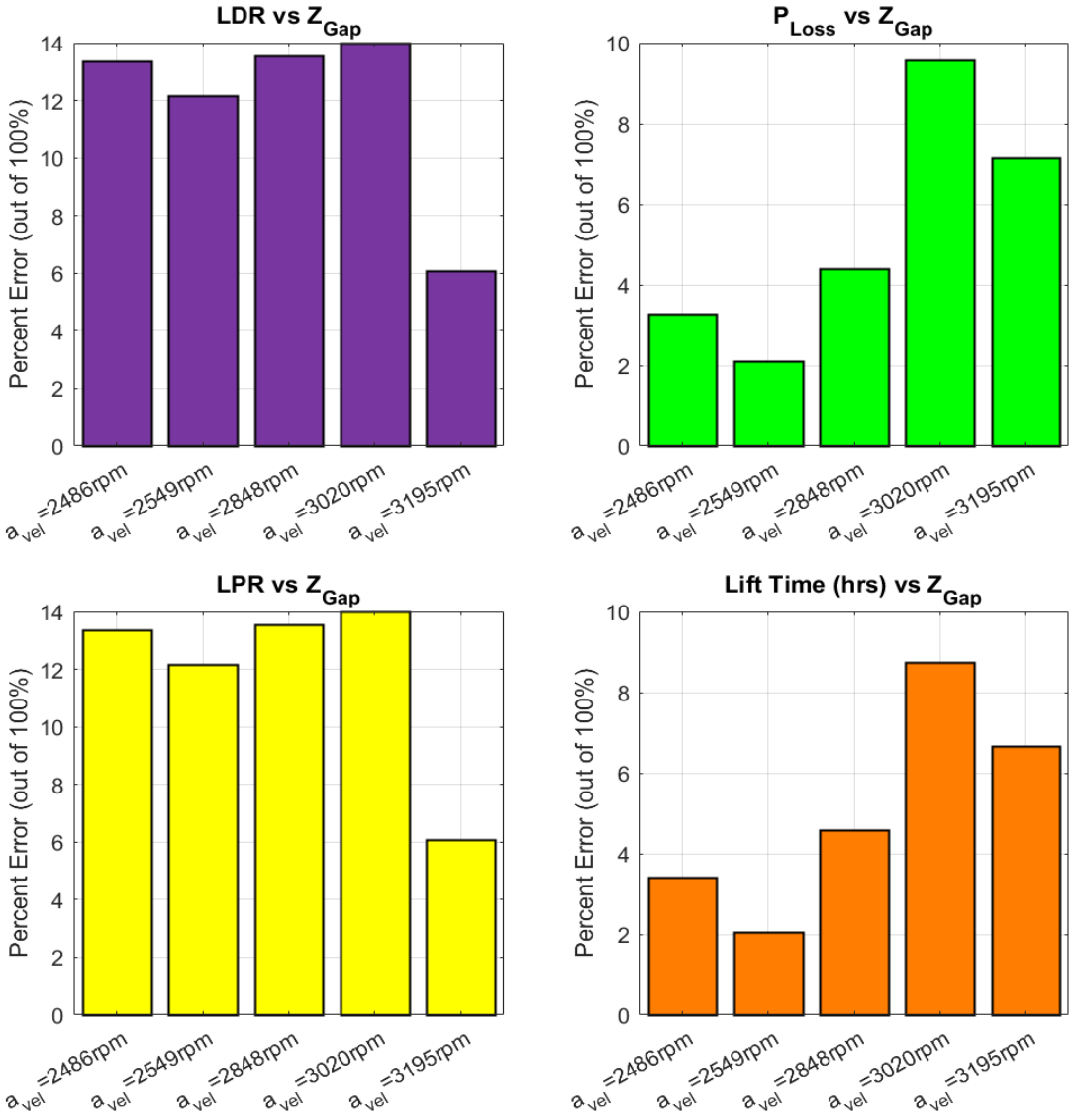

Figure D.4(a)-(d). Percent error of theoretical versus experimental plots at given angular velocities. Data adapted from *Arx-Pax* (2015) [3] and Post & Ryutov (1996). [30]